Computational and Theoretical Insights into Multi-Body Quantum Systems

by

Andrew Stasiuk

A thesis
presented to the University of Waterloo
in fulfillment of the
thesis requirement for the degree of
Masters of Mathematics
in
Applied Math (Quantum Information)

Waterloo, Ontario, Canada, 2021

© Andrew Stasiuk 2021

Examining Committee Membership

The following served on the Examining Committee for this thesis. The decision of the Examining Committee is by majority vote.

Supervisor:	David G. Cory Professor, Dept. of Chemistry, University of Waterloo
Internal Examiner:	Joseph Emerson Associate Professor, Dept. of Mathematics, University of Waterloo
Internal Examiner:	Jon Yard Associate Professor, Institute for Quantum Computing

Author's Declaration

I hereby declare that I am the sole author of this thesis. This is a true copy of the thesis, including any required final revisions, as accepted by my examiners.

I understand that my thesis may be made electronically available to the public.

Abstract

In generality, perfect predictions of the structure and dynamics of multi-body quantum systems are few and far between. As experimental design advances and becomes more refined, experimentally probing the interactions of multiple quantum systems has become commonplace. Predicting this behavior is not a "one size fits all" problem, and has lead to the inception of a multitude of successful theoretical techniques which have made precise and verifiable predictions through, in many cases, clever approximations and assumptions. As the state-of-the-art pushes the quantum frontier to new experimental regimes, many of the old techniques become invalid, and there is often no tractable methodology to fall back on.

This work focuses on expanding the theoretical techniques for making predictions in newly accessible experimental regimes. The transport of quantum information in a room-temperature dipolar spin network is veritably diffusive in nature, but much less is known about the transport properties of such a sample at low temperatures. This work presupposes that diffusion is still a good model for incoherent transport at low temperatures, and proposes a new method to calculate its diffusion coefficient. The diffusion coefficient is reported as a function of the temperature of the ensemble. Further, the interaction of an i.i.d. spin ensemble with a quantized electromagnetic field has long been analyzed via restriction to the Dicke subspace implicit in the Holstein–Primakoff approximation, as well as other within other approximations. This work reanalyzes the conditions under which such a restriction is valid. In regimes where it is shownt that restricting to the Dicke subspace would be invalid, the Hamiltonian structure is thoroughly analyzed. Various predictions can be made by appealing to a reduction in effective dimensionality via a direct sum decomposition.

The main theme of the techniques utilized throughout this work is to appeal to a reduction in difficulty via various theoretical tools in order to prepare for an otherwise intractable computational analysis. Computational insights due to this technique have then gone on to motivate directly provable theoretical results, which might otherwise have remained hidden behind the complexity of the structure and dynamics of a multi-body quantum system.

Acknowledgements

I would like to thank every member in Cory group for the varied discussions on all things quantum - from material science to qubit error correction. The breadth of material we've discussed on a weekly basis has kept my mathematical imagination active, and in part has made this thesis possible.

Table of Contents

List of Figures

Chapter 1

Introduction

Quantum physics is proving to be an extremely useful theoretical framework for describing microscopic systems, leading to advances in fundamental physics and the advent of nanotechnology, with the holy grail being a universal quantum processor [33]. Unlike classical physics, multi-body quantum systems provide the unique challenge of an exponentially growing state space [12]. To contrast, an N body classical physics problem has a state space of dimension $3N$, whereas an N body system of spin-1/2 particles has a state space dimension of 2^N. This massive increase in the number of dimensions over a classical problem is a double edged sword. On one hand, the induced degrees of freedom provide the capacity to store information in a manner that is seemingly entirely de-localized, bringing with it all the banes and boons of entanglement [12][1]. On the other hand, keeping track of all these degrees of freedom either theoretically or computationally can prove insurmountable.

Recently, advances in condensed matter physics and quantum simulators have induced a refreshed interest into multi-body physics[12][17]. Quantum annealers can solve classical optimization problems by encoding onto a multi-body quantum system, where the solution is given by the ground state of the Hamiltonian [39]. Ion and atom traps are able to directly observe the the transport of quantum information in spin chains, giving rise to proposed technologies such as quantum wires [26] [55]. The theoretical tools for solving multi-body systems are varied and often beautifully clever [47].

This work re-examines a familiar structure present in many forms throughout the field of multi-body physics: ensembles of identical spin-1/2 particles. With the spin-1/2 particle serving as the prototypical two level system, and foundation of many proposed and realized quantum technologies [13], it is imperative to better understand how large ensembles of

these particles behave [8]. Two settings are considered here: spins which are coupled to a quantized electromagentic field, and those which are not.

1.1 Quantization of the Electromagnetic Field

In classical spin resonance experiments, all electromagnetic fields are modeled as completely classical objects, that is they do not have their own Hilbert spaces [43]. While a good approximation for many experimental regimes such as room temperature nuclear magnetic resonance (NMR), quantum electrodynamics (QED) indicates that this is not quite true - fields are also quantum objects that can store information in their own Hilbert spaces[52]. The first major success of QED was correctly predicting the so-called Lamb shift of the Hydrogen spectrum in 1947, in which Lamb correctly predicted and measured that the presence of the quantum electromagnetic vacuum splits the energies of otherwise degenerate electronic orbitals[30].

Cavity quantum electrodynamics, or cavity QED, allows for a natural extension of many spin-resonance experiments, which is able to model the various interactions of quantum electromagnetic fields. In particular, the model under consideration here is a one dimensional single mode cavity. The usual approach is to consider a field confined to a length L along the $\boldsymbol{z}$ direction, such that it is electrically polarized in the $\boldsymbol{x}$ direction [37]. The field is completely defined by Maxwell's Equations in free space [19],

$$\begin{aligned} \boldsymbol{\nabla} \cdot \boldsymbol{E} &= 4\pi\rho(\boldsymbol{r},t) & \boldsymbol{\nabla} \times \boldsymbol{E} &= -\frac{1}{c}\frac{\partial \boldsymbol{B}}{\partial t} \\ \boldsymbol{\nabla} \cdot \boldsymbol{B} &= 0 & \boldsymbol{\nabla} \times \boldsymbol{B} &= \frac{1}{c}\left(4\pi \boldsymbol{J}(\boldsymbol{r},t) + \frac{\partial \boldsymbol{E}}{\partial t}\right). \end{aligned} \tag{1.1}$$

Solving these equations, for the spatial profile of the electric field under the assumption that $\boldsymbol{E} = E_x(z,t)\boldsymbol{x}$ and that only the first mode coming from separation of variables is allowed, it is a common exercise to show that

$$E_x(z,t) = E_0 \sin(\pi z/L) q(t), \tag{1.2}$$

for $E_0 = \sqrt{\frac{\hbar\omega}{\epsilon_0 V}}$. Here, $q(t)$ is a yet to be determined function, and V is the effective cavity volume, $V = LA$. The only non-zero component of $\boldsymbol{B}$ can be computed using the Maxwell equations, which yields

$$B_y(z,t) = \frac{\mu_0\epsilon_0 L}{\pi} E_0 \cos(\pi z/L)\frac{\mathrm{d}q(t)}{\mathrm{d}t}. \tag{1.3}$$

Computing the classical energy over this region of volume gives the Hamiltonian for the electromagnetic field,

$$H = \frac{1}{2}\int \mathrm{d}V\left(\epsilon_0 E_x^2 + \frac{1}{\mu_0}B_y^2\right) = \frac{1}{2}\omega^2 q^2 + \frac{1}{2}p^2, \tag{1.4}$$

where $p = \dot{q}$. This Hamiltonian is easily recognized as the harmonic oscillator, and quantizing the Hamiltonian by promoting q and p to operators $\hat{q}$ and $\hat{p}$ such that they canonically commute,

$$[\hat{q}, \hat{p}] = \mathrm{i}\hbar\mathbb{1}, \tag{1.5}$$

yields the equally well known quantum harmonic oscillator [37].

The quantum harmonic oscillator (QHO) is solved by making an operator transformation to the ladder operators [37], defined such that

$$\hat{a} = \frac{1}{\sqrt{2\hbar\omega}}(\omega_c\hat{q} + \mathrm{i}\hat{p}), \tag{1.6}$$

yielding

$$\hat{\mathcal{H}}_c = \hbar\omega_c(\hat{a}^\dagger\hat{a} + 0.5\mathbb{1}). \tag{1.7}$$

The eigenstates of this Hamiltonian are known as Fock states, or number states, indexed by $|n\rangle$ for $n \in \mathbb{N}$. Thus,

$$\hat{\mathcal{H}}_c\,|n\rangle = \hbar\omega_c(n + 0.5)\,|n\rangle\,. \tag{1.8}$$

From the canonical commutation operators, it can be determined that $[\hat{a}, \hat{a}^\dagger] = \mathbb{1}$, which allows one to compute their action on the Fock number basis states,

$$\begin{aligned}\hat{a}\,|n\rangle &= \sqrt{n}\,|n-1\rangle\\ \hat{a}^\dagger\,|n\rangle &= \sqrt{n+1}\,|n+1\rangle\,.\end{aligned}$$

Now, one can introduce a spin-1/2 particle in this cavity at some location $z_0 \in [0, L]$ along with a large classical magnetic field along $\boldsymbol{z}$ for the purpose of giving the spin a well defined Zeeman splitting. The Zeeman splitting is described by the Hamiltonian [43],

$$\hat{\mathcal{H}}_s = \frac{\hbar B_0\gamma}{2}\hat{\sigma}_z = \frac{\hbar\omega_0}{2}\hat{\sigma}_z. \tag{1.9}$$

In the above internal Hamiltonian of the spin γ is the gyromagnetic ratio of the spin particle, and $\hat{\sigma}_z$ is the Pauli z operator, which can be written in its eigenbasis as

$$\hat{\sigma}_z = |e\rangle\langle e| - |g\rangle\langle g|\,. \tag{1.10}$$

In the regimes of interest to this work, the spin is well described as by a point particle [43] with a magnetic dipole moment of

$$\hat{\boldsymbol{\mu}} = \frac{\hbar\gamma}{2}(\hat{\sigma}_x \boldsymbol{x} + \hat{\sigma}_y \boldsymbol{y} + \hat{\sigma}_z \boldsymbol{z}). \tag{1.11}$$

Thus the interaction of the (stationary) spin with the quantum field is described by the minimal coupling Hamiltonian [37], such that

$$\hat{\mathcal{H}}_I = \hat{\boldsymbol{E}}(z_0) \cdot \hat{\boldsymbol{\mu}} = \hbar g(z_0)(\hat{a}^\dagger + \hat{a}) \otimes (\hat{\sigma}_+ + \hat{\sigma}_-), \tag{1.12}$$

where $g(z)$ is a scalar function encoding the overlap of the quantum field with the spin at given location of the spin, assuming that the spin is point-like compared to L. For electron spin resonance systems (ESR), the strength of the spin–cavity interaction is given by the geometric parameter

$$g_0 = g_e \mu_B \sqrt{\frac{\mu_0 \omega_c}{2V_c}}, \tag{1.13}$$

where g_e is the electron Landau g-factor, μ_B is the Bohr magneton, μ_0 is the permeability of free–space, and V_c is the mode volume of the cavity.

Combining all the pieces together, the Hamiltonian for the entire system is given by

$$\hat{\mathcal{H}} = \hat{\mathcal{H}}_c \otimes \mathbb{1} + \mathbb{1} \otimes \hat{\mathcal{H}}_s + \hat{\mathcal{H}}_I. \tag{1.14}$$

Omitting the tensor products and identities where clear, defining $g_0 = g(z_0)$, this allows the Hamiltonian to be written as

$$\frac{1}{\hbar}\hat{\mathcal{H}} = \omega_c \hat{a}^\dagger \hat{a} + 0.5\omega_s \hat{\sigma}_z + g_0(\hat{a}^\dagger \hat{\sigma}_- + \hat{a}\hat{\sigma}_+) + g_0(\hat{a}^\dagger \hat{\sigma}_+ + \hat{a}\hat{\sigma}_-). \tag{1.15}$$

In the above Hamiltonian the lone identity was omitted since it a constant energy shift, leading to an un-physical global phase in the time evolution of an arbitrary state. The coupling Hamiltonian has been split into two groups, as they are behave differently. The $\hat{a}^\dagger\hat{\sigma}_- + \hat{a}\hat{\sigma}_+$ term is a so-called "flip-flop" exchange, which mediates the transfer of excitations between the spin and the field, and is thus occasionally called an "energy conserving term" [37]. This is in part because the term conserves excitations, which are defined as eigenvalues of the operator $\hat{K}$,

$$\hat{K} = \hat{a}^\dagger \hat{a} \otimes \mathbb{1} + \mathbb{1} \otimes \frac{\mathbb{1} + \hat{\sigma}_z}{2}. \tag{1.16}$$

When the spin and cavity are on resonance, $\omega_s = \omega_c = \omega_0$, the excitation operator maps directly to the internal energy portion of the Hamiltonian. Thus, if the spin-cavity coupling

is treated as a perturbative drive, it can be thought of as driving transitions to a state with the same energy eigenvalue. The $\hat{a}^\dagger\hat{\sigma}_+ + \hat{a}\hat{\sigma}_-$ term is often referred to as the "counter-rotating" term, and it does not conserve the number of excitations, rather, it raises and lowers them in steps of size 2.

The derived Hamiltonian can be extended to the many-spin case by repeating the coupling process for every spin of interest. Each spin is located at some $z_i \in [0, L]$, leading to an effective spin-cavity coupling of $g_i = g(z_i)$. Further, inhomogenieties or variations in the field at a given z_i would lead to variation in the Zeeman splitting even if each spin has the same gyromagnetic ratio. Take $\omega_i = \gamma B_0(z_i)$ to be splitting for the ith spin. For convenience assume that the spins are non-interacting. Then, the total Hamiltonian is given by

$$\frac{1}{\hbar}\hat{\mathcal{H}} = \omega_c \hat{a}^\dagger\hat{a} + \frac{1}{2}\sum_{i=1}^{N} \omega_s^{(i)}\hat{\sigma}_z^{(i)} + \sum_{i=1}^{N}\left(g_i(\hat{a}^\dagger\hat{\sigma}_-^{(i)} + \hat{a}\hat{\sigma}_+^{(i)}) + g_i(\hat{a}^\dagger\hat{\sigma}_+^{(i)} + \hat{a}\hat{\sigma}_-^{(i)})\right). \tag{1.17}$$

In order to simplify the Hamiltonian, it's often assumed that the classical field is very nearly uniform, so that $\omega_s^{(i)} \approx \omega_s$ for all i, and that all spins are concentrated about $L/2$ such that $g_i \approx g_0$ for each i. Experimentally a uniform magnetic field is never truly satisfied, but coil design can significantly mitigate sources of inhomogeneity [54]. There is a trade-off of scales in any multi-spin experiment, in that the higher the spin-density, the more closely the uniform coupling approximation will be satisfied, which then competes with the fact that spin-spin coupling cannot be neglected if the spins are close together. For example, dipolar coupling between spins scales as $1/d^3$, where d is the separation between two spins [43].

Under the uniform coupling assumptions, the Hamiltonian can be rewritten using the collective operators $\hat{J}_z = 0.5\sum_i \hat{\sigma}_z^{(i)}$ and $\hat{J}_\pm = \sum_i \hat{\sigma}_\pm^{(i)}$, which span the algebra of $\mathfrak{sl}(2;\mathbb{C})$. The move to collected operators seems to seems to imply that an ensemble of spins, being indistinguishable to the cavity, will emulate behavior tantamount to a single spin with a much higher value for its angular momentum. The consequences of this interpretation will be explored in great depth in Section 3.1. Further, we assume that the spin ensemble and the cavity are on resonance, such that $\omega_s = \omega_c = \omega_0$. The collective Hamiltonian can be then written compactly using this notation as,

$$\frac{1}{\hbar}\hat{\mathcal{H}} = \omega_0\hat{a}^\dagger\hat{a} + \omega_0\hat{J}_z + g_0(\hat{a}^\dagger\hat{J}_- + \hat{a}\hat{J}_+) + g_0(\hat{a}^\dagger\hat{J}_+ + \hat{a}\hat{J}_-). \tag{1.18}$$

The number of collective excitations can be similarly defined by extending $\hat{K}$ with a summation over all spins, analogous to how the collective Hamiltonian was derived. In particular,

omitting the tensor products with identity for brevity,

$$\hat{K} = \hat{a}^\dagger \hat{a} + \hat{J}_z + \frac{N}{2}\mathbb{1}. \tag{1.19}$$

The validity of the uniform coupling approximations varies based on the experimental apparatus, and variations from the mean coupling strengths will serve to cause unitary errors relative to the idealized prediction. Of course, in any realistic scenario, noise and decoherence is nigh unavoidable. Much of this work relies on the validity of these assumptions, which contrasts with the fact there is likely no physical system without imperfections. While this work focuses primarily on the ideal setting, modeling the effective noise caused by these inhomogenieties is an interesting and difficult problem [8], which may be a fruitful avenue for future work.

1.2 The Rotating Wave Approximation

Considering the Hamiltonian for a single spin coupled to the cavity, given by equation (1.15), there are further approximations that can be made to simplify the problem. In particular, consider moving into a rotating frame generated by

$$\frac{1}{\hbar}\hat{\mathcal{H}}_0 = \omega_0 \hat{a}^\dagger \hat{a} + 0.5\omega_0 \hat{\sigma}_z. \tag{1.20}$$

In general, a frame transformation generated by $\hat{U}_R(t)$ does the following [37]:

$$\begin{aligned} |\psi\rangle \longrightarrow |\psi_R\rangle &= \hat{U}_R |\psi\rangle \\ \hat{\mathcal{H}} \longrightarrow \hat{\mathcal{H}}_{rot} &= \hat{U}_R \hat{\mathcal{H}} \hat{U}_R^\dagger + \mathrm{i}\frac{\mathrm{d}\hat{U}_R}{\mathrm{d}t}\hat{U}^\dagger. \end{aligned} \tag{1.21}$$

Thus, in the case where

$$\hat{U}_R = \exp \frac{\mathrm{i}\hat{\mathcal{H}}_0 t}{\hbar}, \tag{1.22}$$

the rotating frame Hamiltonian is transformed to

$$\frac{1}{\hbar}\hat{\mathcal{H}}_{rot}(t) = g_0\big(e^{\mathrm{i}(\omega-\omega_0)t}\hat{a}^\dagger\hat{\sigma}_- + e^{-\mathrm{i}(\omega-\omega_0)t}\hat{a}\hat{\sigma}_+\big) + g_0\big(e^{\mathrm{i}(\omega+\omega_0)t}\hat{a}^\dagger\hat{\sigma}_+ + e^{-\mathrm{i}(\omega+\omega_0)t}\hat{a}\hat{\sigma}_-\big). \tag{1.23}$$

It is useful now to to particularize to a set of parameter ranges on the phenomenological constants present in the Hamiltonian. The experimental apparatus in mind for this work is

an electron spin resonance (ESR) system where a collection of electrons will be interacting with a 1D microwave cavity. With a large static field, ω_0 can be taken to be on the order of 10 GHz, while g_0 is on the order of 10 Hz [2]. The rotating frame Hamiltonian can be written as

$$\frac{1}{\hbar}\hat{\mathcal{H}}_{rot}(t) = g_0(\hat{a}^\dagger\hat{\sigma}_- + \hat{a}\hat{\sigma}_+) + g_0\big(e^{2i\omega_0 t}\hat{a}^\dagger\hat{\sigma}_+ + e^{-2i\omega_0 t}\hat{a}\hat{\sigma}_-\big). \tag{1.24}$$

Above, the excitation number conserving portion of the interaction Hamiltonian is static in the rotating frame, while the excitation raising and lowering term picks up a time dependence that corresponds to it rotating opposite the rotating frame. It is for this reason that these terms are dubbed "counter-rotating".

Since $g_0/\omega_0 \ll 1$, the interaction Hamiltonian can be well treated as a perturbation of $\hat{\mathcal{H}}_0$. With this in mind, excitation non-conserving transitions inherit a highly suppressed transition rate to the point of being effectively un-observable in most experiments [37]. Further, when the spin and cavity are on resonance, $\omega = \omega_0$, this is the only term in the Hamiltonian which doesn't commute with the dominant $\hat{\mathcal{H}}_0$ term, making it secular. All of these arguments coalesce together to form the backbone of the rotating wave approximation (RWA) – the excitation raising and lower terms can be removed from the original Hamiltonian with confidence that any predictions derived would be in good agreement with reality. In summation, the Hamiltonian of theoretical interest is given by,

$$\frac{1}{\hbar}\hat{\mathcal{H}}_{JC} = \omega_0\hat{a}^\dagger\hat{a} + 0.5\omega_0\hat{\sigma}_z + g_0(\hat{a}^\dagger\hat{\sigma}_- + \hat{a}\hat{\sigma}_+), \tag{1.25}$$

which is referred to in literature as the Jaynes-Cummings Hamiltonian [42].

The above argument can be analogously extended to the case where many spins are uniformly (and resonantly) coupled to the single mode cavity, due to the fact that the collective operators satisfy the same commutation relations as the single spin operators,

$$[\hat{J}_z, \hat{J}_\pm] = \pm\hat{J}_\pm. \tag{1.26}$$

Thus, the collective Hamiltonian under the rotating wave approximation is

$$\frac{1}{\hbar}\hat{\mathcal{H}}_{TC} = \omega_0\hat{a}^\dagger\hat{a} + \omega_0\hat{J}_z + g_0(\hat{a}^\dagger\hat{J}_- + \hat{a}\hat{J}_+), \tag{1.27}$$

which is referred to in the literature as the Tavis-Cummings Hamiltonian[48]. The validity of the rotating wave approximation for the ensemble is usually given with the condition that $\omega_0 \gg g_0\sqrt{N}$. This work's discussion on the TC Hamiltonian focuses on systems in the strong coupling regime, where the field interaction with the spins can be resolved experimentally and the RWA holds. This work further avoids discussing dynamics in the ultra-strong coupling regime, in which the RWA is violated in a measurable fashion. A more precise discussion on the condition for the validity of the RWA is given in 3.1.

1.3 Dipolar Spin Hamiltonian

Consider now an ensemble of energetically identical spins, distinguished by their fixed locations in space, experiencing a large, uniform, classical magnetic field. Take each of these spins to be interacting with all-to-all connections through dipole-dipole coupling. Due to the large field, a secular approximation can be made on the homonuclear dipole interaction, including only the A and B terms of the dipolar alphabet [43]. Thus,

$$\hat{\mathcal{H}} = \hat{\mathcal{H}}_s + \hat{\mathcal{H}}_{Dipolar}, \tag{1.28}$$

where

$$\hat{\mathcal{H}}_s = \hbar B_0 \gamma \sum_i \hat{S}_z^{(i)} = \hbar \omega_0 \hat{J}_z, \tag{1.29}$$

and

$$\hat{\mathcal{H}}_{Dipolar} = \frac{\mu_0 \hbar^2 \gamma^2}{8\pi} \sum_{i \neq j} \frac{1 - 3\cos^2\theta_{ij}}{r_{ij}^3} \big(\hat{S}_z^{(i)} \hat{S}_z^{(j)} - \frac{1}{4} (\hat{S}_+^{(i)} \hat{S}_-^{(j)} + \hat{S}_-^{(i)} \hat{S}_+^{(j)}) \big). \tag{1.30}$$

In equation (1.30), it should be understood that r_{ij} is the distance between the spins labeled by indices i and j, and θ_{ij} is the angle that a line connecting these two spins makes with external magnetic field, which in this case is along the z direction, in the lab frame. Further, it should be understood that $\hat{S}_z^{(i)}$ is one-half of the Pauli-z operator for spin i, such that

$$[\hat{S}_\mu^{(i)}, \hat{S}_\nu^{(j)}] = \mathrm{i} \epsilon_{\mu\nu}{}^{\eta} \delta_{ij} \hat{S}_\eta^{(i)}, \tag{1.31}$$

where $\mu, \nu, \eta \in \{x, y, z\}$, and the angular momentum ladder operators are defined as usual so that

$$\hat{S}_\pm^{(i)} = \hat{S}_x^{(i)} \pm \mathrm{i} \hat{S}_y^{(i)}. \tag{1.32}$$

Global magnetization is a conserved quantity, which follows from the commutation relation, $[\hat{J}_z, \hat{\mathcal{H}}] = 0$. Moving into a rotating frame generated by $\hat{J}_z$ will cancel the Zeeman portion of the Hamiltonian, yielding a time independent rotating frame Hamiltonian consisting of only the homonuclear dipolar interaction:

$$\hat{\mathcal{H}}_{rot} = \hbar \sum_{i \neq j} b_{ij} \big(\hat{S}_z^{(i)} \hat{S}_z^{(j)} - \frac{1}{4} (\hat{S}_+^{(i)} \hat{S}_-^{(j)} + \hat{S}_-^{(i)} \hat{S}_+^{(j)}) \big), \tag{1.33}$$

where b_{ij} is defined such that

$$b_{ij} := \frac{\mu_0 \hbar \gamma^2 \big(1 - 3\cos^2\theta_{ij}\big)}{8\pi r_{ij}^3}, \tag{1.34}$$

for convenience. Now, consider the action of this Hamiltonian on states contained within the Zeeman basis. An N-partite state is an element of the Zeeman basis if every subsystem's state is an eigenstate of $\hat{\sigma}_z$. That is, each spin is either aligned or anti-aligned with the magnetic field. The first term of the rotating frame Hamiltonian, given by the A term in the dipolar alphabet [43], is simply a state dependent energy shift. On the other hand, the term originating from the B portion of the dipolar alphabet, mediates a mutual spin flip exchange [43]. For this reason, this term shall be referred to as the flip-flop term or interaction. In other words, the flip-flop interaction appears to facilitate a local distribution of magnetization to move through the spin network, whilst still conserving the total magnetization. Thus one would expect that the action of the flip-flop term, will mediate a local transport of magnetization. Given the global conservation law, it is reasonable to guess that this transport will be diffusive in nature. Assuming this is indeed the case, a diffusion coefficient should be given to quantify the diffusion rate.

Spin diffusion was first measured in 1998 [56], confirming the suspicions of early researchers in that there were additional sources of noise causing rapid spin-lattice relaxation present in solid NMR samples [5][4][50]. The notion of spin diffusion was later firmly connected to theoretically tractable computations of moments of the measured spectral line shape [34]. After overcoming many technological hurdles, the 1998 experiment directly verified the predicted diffusion rates in a Calcium Flouride crystal, which is cubic and has full translational symmetry [56]. Further, it was found that dipolar ordered states had a larger diffusion coefficient (and thus a faster diffusion rate) than Zeeman ordered states, and this discrepancy was attributed to coherent transport effects via interference of initially correlated neighboring spins [7].

Chapter 2

Semi-Classical Spin Diffusion

Historically, spin diffusion has referred to a few concepts, including the spatial diffusion of spin-active particles of a liquid, like Helium-3 [22], and the diffusion of polarization in a crystalline solid[4][56]. This chapter focuses on the latter. In particular, spin-diffusion in crystalline solids has been able to aptly describe the evolution of many body quasi-equilibrium states, which are many-body quantum states which deviate slightly from thermal equilibrium [18]. With this class of states, it is common to make a long wavelength, meaning that the deviations from equilibrium vary slowly and continuously as a function of some spatial dimension. In this regime, theory and experiment coincide on the diffusion rates of Calcium-Fluoride, and the state-of-the-art for calculating the diffusion rate theoretically uses what is known as a modified Kubo formula [7][18]. Derivation of the Kubo formula utilizes the fact that the state of the crystal is near equilibrium to take thermodynamic derivatives in order to simplify particular quantities. In particular, linear response of magnetization with respect to a large external field is assumed [27][25].

It is then clear that the Kubo formula approach would be incorrect for states which are far from thermodynamic equilibrium, as this would violate the underlying assumptions needed to derive the formula. Due to the difficulty of polarizing large ensembles of spins, in part because of the very long nuclear T_1 times at the bath temperatures required, very little effort has gone into developing methods for calculating diffusion rates in regimes far from thermal equilibrium. With rapidly improving technology, highly polarized spin ensembles are becoming more feasible experimentally [24] [40], and thus should no longer be ignored theoretically.

This chapter focuses on describing the characteristic properties of spin-diffusion in a highly polarized spin ensemble. This approach is further motivated to focus on a single

atomic species crystal, particularly a single crystal sample of Silicon-29. There has been some promising work recently in terms of polarizing Phosphorus within a Silicon crystal, and due to Silicon's long T_1 times, this makes it an excellent experimental candidate to focus on theoretically [21].

2.1 Casting the Problem as a Random Walk

Before transforming the Hamiltonian any further, it is instructive to consider the expected initial state of the spin ensemble. The working assumption for this approach requires that the crystal is initially highly polarized and all spins contain no initial quantum correlations, so that

$$\hat{\rho}_0 = \left(\frac{1}{2}\big(\mathbb{1} + (1-\epsilon)\hat{\sigma}_z\big)\right)^{\otimes N}, \tag{2.1}$$

where $1-\epsilon$ is the initial polarization, and ϵ is taken to be small, but non-zero, $0 < \epsilon \ll 1$. Equivalently, the state of the spins can be recast directly in the Zeeman basis, $\{|0\rangle, |1\rangle\}$, so that

$$\hat{\rho}_0 = \left(\left(1-\frac{\epsilon}{2}\right)|0\rangle\langle 0| + \frac{\epsilon}{2}|1\rangle\langle 1|\right)^{\otimes N}. \tag{2.2}$$

By treating this density matrix as a statistical ensemble of pure states, one can see that each spin has a probability $p_0 = 1-\frac{\epsilon}{2}$ to be aligned with the external field, and a probability $p_1 = \frac{\epsilon}{2}$ to be anti-aligned with the external field (under a projective measurement). This directly implies that the number of spins anti-aligned (or equivalently, aligned) with the external field is an instance of a binomial distribution, defined by N and probability p_1. A full quantum treatment would involve averaging over all 2^N possible crystal states. This can be avoided by noting that for highly polarized ensembles, the induced binomial distribution on the number of anti-aligned spins will not be strongly supported after about three standard deviations from the mean, so that the range on the number of anti-aligned spins which contribute significantly is considerably bounded:

$$\max\left\{0, \frac{N\epsilon}{2} - 3\sqrt{N\frac{\epsilon}{2}(1-\frac{\epsilon}{2})}\right\} \leq n_{sig} \leq \frac{N\epsilon}{2} + 3\sqrt{N\frac{\epsilon}{2}(1-\frac{\epsilon}{2})}. \tag{2.3}$$

This still leaves the issue that for a given number of anti-aligned spins, n, in a lattice there are

$$m = \binom{N}{n} \tag{2.4}$$

possible spatial distributions of anti-aligned spins, which can easily become a significant quantity for large ensembles. Due to the fact that we expect that the behaviour of a particular anti-aligned spin will depend mainly upon its local neighbourhood of spins, its vicinity to crystal edges, and state of the crystal as a whole, one can make the *a priori* assumption that many of these crystal instances will display similar transport properties. Thus a Monte Carlo type approach to numerical simulations can be used, such that each trial starts by sampling a Bernoulli distribution for each spin to determine its initial state. Ignoring spatial distribution of spins, this is equivalent to sampling a binomial distribution to determine the number of anti-aligned spins. The advantage to the repeated Bernoulli sampling approach is that it takes care of randomized spatial distributions for free.

To reiterate, it is expected that the flip-flop term in the Hamiltonian will mediate a diffusion process for local magnetization. In particular, for a given polarization one can produce a set of meaningful pure states corresponding to the true state of the crystal, which after averaging will give the bulk behaviour for the true mixed state of the crystal. It still remains to be shown how to calculate the effective diffusion coefficient, as a function of the polarization of the initial state.

In order to compute the rate at which magnetization diffuses through the crystal, one needs to determine the time evolution of the crystal, at least approximately. For a time independent Hamiltonian, the propagation operator can be written symbolically as the exponential of the Hamiltonian,

$$\hat{U}(t) = \exp\left(\frac{\mathrm{i}t}{\hbar}\hat{\mathcal{H}}_{rot}\right). \tag{2.5}$$

This propagation operator is not functionally useful for large system sizes, as it does not have a clean closed from solution. In order to sidestep the exponential difficulty of this problem, it is common to appeal to perturbation theory. In particular, the Dyson expansion is a reasonable choice, since the Hamiltonian is already of the form $\hat{\mathcal{H}} = \hat{\mathcal{H}}_0 + \lambda\hat{V}$. To prepare for this expansion, one can move into the interaction picture generated by

$$\hat{\mathcal{H}}_0 = \hbar\sum_{i\neq j} b_{ij}\hat{S}_z^{(i)}\hat{S}_z^{(j)}, \tag{2.6}$$

so that

$$\hat{U}_D(t) = e^{\mathrm{i}t\hat{\mathcal{H}}_0}. \tag{2.7}$$

Then,

$$|\psi_D\rangle = \hat{U}_D\,|\psi\rangle\,, \tag{2.8}$$

and it is important to note that all the crystal states of interest are eigenstates of $\hat{\mathcal{H}}_0$, and so this transformation adds an un-physical global phase which can be safely ignored. Taking $\lambda = 0.25$, and

$$\hat{V} = \sum_{i \neq j} b_{ij} \big(\hat{S}_+^{(i)} \hat{S}_-^{(j)} + \hat{S}_-^{(i)} \hat{S}_+^{(j)} \big), \tag{2.9}$$

the Schrodinger equation in the interaction picture transforms to

$$\frac{\mathrm{d}}{\mathrm{d}t} |\psi_D\rangle = \frac{1}{4} \mathrm{i} \hat{V}_D(t) |\psi_D\rangle . \tag{2.10}$$

In the above equation,

$$\hat{V}_D(t) = \hat{U}_D(t) \hat{V} \hat{U}_D^\dagger(t), \tag{2.11}$$

which simplifies to the following by use of an identity[7]:

$$\hat{V}_D(t) = \sum_{i \neq j} b_{ij} \left(\hat{S}_+^{(i)} \hat{S}_-^{(j)} \hat{L}_{ij}(t) + \hat{S}_-^{(i)} \hat{S}_+^{(j)} \hat{L}_{ji}(t) \right), \tag{2.12}$$

where

$$\hat{L}_{ij}(t) = \prod_{l \neq i,j} \exp \left(2\mathrm{i}t(b_{li} - b_{lj}) \hat{S}_z^{(l)} \right) = \exp \left(\sum_{l \neq i,j} 2\mathrm{i}t(b_{li} - b_{lj}) \hat{S}_z^{(l)} \right). \tag{2.13}$$

Notice,

$$\hat{L}_{ji}^\dagger(t) = \hat{L}_{ij}(t), \tag{2.14}$$

which guarantees that the interaction picture Hamiltonian is still self-adjoint, and thus evolution is still unitary. Further, note that the action of this operator on a crystal state which is solely the product of Zeeman states can be calculated exactly without the need for any approximations:

$$\hat{L}_{ij} |\psi_{crystal}\rangle = \exp \left(\mathrm{i}t \Big(\sum_{\substack{l \neq i,j \\ aligned}} (b_{li} - b_{lj}) - \sum_{\substack{l \neq i,j \\ anti-aligned}} (b_{li} - b_{lj}) \Big) \right) |\psi_{crystal}\rangle . \tag{2.15}$$

For convenience, define

$$\Omega_{ij}(\psi) = \sum_{\substack{l \neq i,j \\ aligned}} (b_{li} - b_{lj}) - \sum_{\substack{l \neq i,j \\ anti-aligned}} (b_{li} - b_{lj}). \tag{2.16}$$

Ω will often be referred to as the "mean-field" frequency of the crystal state, as it is dependent on the relative orientations of spins throughout the crystal. The solution of

the Schrodinger equation in the interaction picture is formally a time-ordered exponential, which shall be expanded as a Dyson series [37]:

$$\hat{U} = \mathcal{T} \exp\left(\int_0^t \mathrm{d}s \, \hat{V}_D(s) \right) = \mathbb{1} + \hat{U}^{(1)} + \hat{U}^{(2)} + \cdots . \tag{2.17}$$

Here, the Dyson terms are given as usual:

$$\hat{U}^{(1)} = \frac{1}{4}\mathrm{i} \int_0^t \mathrm{d}t_1 \, \hat{V}_D(t_1) \tag{2.18}$$

$$\hat{U}^{(2)} = -\frac{1}{16} \int_0^t \mathrm{d}t_1 \int_0^{t_1} \mathrm{d}t_2 \, \hat{V}_D(t_1)\hat{V}_D(t_2) \tag{2.19}$$

$$\vdots$$

$$\hat{U}^{(n)} = \left(\frac{1}{4}\mathrm{i}\right)^n \int_0^t \mathrm{d}t_1 \int_0^{t_1} \mathrm{d}t_2 \cdots \int_0^{t_{n-1}} \mathrm{d}t_n \, \hat{V}_D(t_1)\hat{V}_D(t_2)\cdots\hat{V}_D(t_n). \tag{2.20}$$

The Dyson series provides path towards computing transition probabilities for the quantum state of the crystal. At zeroth order, there are no non-trivial transition probabilities, and thus no transport occurs. At first order, any anti-aligned spin can swap places with any aligned spin, so long as their dipolar coupling constant is non-zero. That is, oppositely aligned spins i and j can swap orientations so long as $b_{ij} \neq 0$. Now, due to the abundance of aligned spins relative the the number of anti-aligned spins in a given crystal state of interest, one can view the crystal as a sea of aligned spins with a few ant-aligned spin defects which are allowed to move around this sea in a random manner. In fact, the discrete spin sites coupled with transition probabilities in a particular time step can be mapped to a similar classical problem of a random walk. That is to say, this perturbation scheme can be interpreted so that magnetization "defects" take a random walk through the crystal lattice. While this random walk is a classical notion, the walk weights themselves are computed from quantum theory.

Now, a random walk will converge to a Wiener process, by way of the central limit theorem [45]. This means that in the continuous limit of the random walk, the distribution induced by the psuedo-random motion of spin defects converges to a Gaussian. Likewise, the Green's function for the diffusion equation is a Gaussian [14]. Thus, one can take the correspondence of these two functions to posit an effective diffusion rate for the spin defects. More precisely, in 3 spatial dimensions the diffusion rate is written as

$$D = \frac{\langle r^2 \rangle|_{t=\delta t}}{6\delta t}. \tag{2.21}$$

Here, 6 is a dimensional factor, δt is the length of a time-step, and $\langle r^2 \rangle$ is the mean squared distance of the random movement of a defect with an initially known location after a time δt.

With an expression for calculating the effective diffusion coefficient in terms of transition probabilities, and a method for calculating these probabilities, it remains only to calculate the diffusion coefficient. To do so, consider a particular initial state of the crystal, called $|in\rangle$. Then, for a particular spin defect at index n, sum over all of its possible transitions, each of which produces a final state of the crystal, referred to without loss of generality as $|out\rangle$. Then, the probability that a particular transition occurs within a time period δt is given by

$$P_{hop} = \left| \left\langle out \right| \hat{U}(\delta t) \left| in \right\rangle \right|^2, \tag{2.22}$$

so that

$$\left\langle r^2 \right\rangle = \sum_{hops} P_{hop} (r_{hop})^2. \tag{2.23}$$

While $\hat{V}_D(t)$ is a sum over $N(N-1)$ terms, any given transition will not require all terms of the sum:

$$\left\langle 1_m 0_n \cdots \right| \hat{S}_+^{(i)} \hat{S}_-^{(j)} \left| 0_m 1_n \cdots \right\rangle = \delta_{im} \delta_{jn}. \tag{2.24}$$

Thus for a first order transition of a defect at index n hoping to an allowed index m, only two terms of the sum need to be considered. For this transition, written as $(n \longrightarrow m)$ for brevity, the matrix element can be computed as follows:

$$\begin{aligned}
U_{n\to m}^{(1)} &= \left\langle out \right| \hat{U}^{(1)} \left| in \right\rangle \\
&= \frac{\mathrm{i}}{4} \int_0^t \mathrm{d}t_1 \; b_{mn} \left(e^{\mathrm{i}t_1 \Omega_{mn}(in)} + e^{\mathrm{i}t_1 \Omega_{mn}(in)} \right) \\
&= \frac{\mathrm{i}b_{nm}}{2} \int_0^t \mathrm{d}t_1 \exp\left(\Omega_{nm}(in) t_1 \right) \\
&= \frac{\mathrm{i}b_{nm}}{2\mathrm{i}\Omega_{nm}(in)} \left(\exp\left(\mathrm{i}\Omega_{nm}(in) t \right) - 1 \right) \\
&= \frac{\mathrm{i}b_{nm}}{\Omega_{nm}(in)} \frac{\exp \frac{\mathrm{i}\Omega_{nm}(in)t}{2} - \exp \frac{-\mathrm{i}\Omega_{nm}(in)t}{2}}{2\mathrm{i}} \exp \frac{\mathrm{i}\Omega_{nm}(in)t}{2} \\
&= \frac{\mathrm{i}b_{nm}}{\Omega_{nm}(in)} \sin \frac{\Omega_{nm}(in)t}{2} \exp \frac{\mathrm{i}\Omega_{nm}(in)t}{2}.
\end{aligned} \tag{2.25}$$

Then, at first order, for the spin defect at index n, for some well chosen δt, with surrounding crystal state represented as $|in\rangle$, it will see an effective diffusion coefficient of

$$D_n^{(1)} \approx \sum_m{}' \frac{b_{nm}^2 r_{nm}^2}{6\delta t \Omega_{nm}^2} \sin^2 \frac{\Omega_{nm}\delta t}{2}, \tag{2.26}$$

where the sum over m is only over indices with initial spin state aligned with the external field, as indicated by the apostrophe notation.

Continuing on to second order transitions, there is now a summation over 4 indices, culminating in $N^2(N-1)^2$ terms, and each term of the sum contains a product of 2 flip-flop operators. This mediates two new types of transitions, $(n \longrightarrow r \longrightarrow m)$ and $(n \longrightarrow m, p \longrightarrow q)$, or in words, a double hop transition and two independent single hop transitions. To calculate the matrix elements for the double hop, notice that the sum will be over terms of the following form:

$$\begin{aligned}\left\langle 1_m 0_r 0_n \cdots \right| \hat{S}_+^{(i)} \hat{S}_-^{(j)} \hat{L}_{ij}(t_1) \hat{S}_+^{(k)} \hat{S}_-^{(l)} \hat{L}_{kl}(t_2) \left| 0_m 0_r 1_n \cdots \right\rangle \\ = \delta_{nl}\delta_{kr} e^{\mathrm{i}\Omega_{kl}(in)t_2} \delta_{jr}\delta_{im} e^{\mathrm{i}\Omega_{ij}(in;n\to r)t_1}.\end{aligned} \tag{2.27}$$

In the above equation, $\Omega_{ij}(in; n \to r)$ indicates that this must be calculated as a function of the updated crystal state, after the first hop. After some arithmetic,

$$U_{n\to m}^{(2)} = \sum_{r\neq n,m}{}' \frac{\mathrm{i}b_{mr}b_{rn}}{2\Omega_{rn}} \left(\frac{\sin\frac{(\Omega_{mr}+\Omega_{rn})t}{2}}{\Omega_{mr}+\Omega_{rn}} \exp\frac{\mathrm{i}t(\Omega_{mr}+\Omega_{rn})}{2} - \frac{\sin\frac{\Omega_{mr}t}{2}}{\Omega_{mr}} \exp\frac{\mathrm{i}t\Omega_{mr}}{2} \right), \tag{2.28}$$

where the explicit dependence of Ω on the crystal state is omitted for notational brevity. For the case of the double hop transition, there needs to be least two spin defects in the lattice, which shall be labelled by indices n and p without any loss of generality. Then, transitions are of the form,

$$\begin{aligned}\left\langle 0_n 1_m 0_p 1_q \cdots \right| \hat{S}_+^{(i)} \hat{S}_-^{(j)} \hat{L}_{ij}(t_1) \hat{S}_+^{(k)} \hat{S}_-^{(l)} \hat{L}_{kl}(t_2) \left| 1_n 0_m 1_p 0_q \cdots \right\rangle \\ = \delta_{km}\delta_{ln} e^{\mathrm{i}\Omega_{kl}(in)t_2} \delta_{iq}\delta_{jp} e^{\mathrm{i}\Omega_{ij}(in;n\to m)t_1} \\ + \delta_{kq}\delta_{lp} e^{\mathrm{i}\Omega_{kl}(in)t_2} \delta_{im}\delta_{jn} e^{\mathrm{i}\Omega_{ij}(in;p\to q)t_1}.\end{aligned} \tag{2.29}$$

The intuition for these terms is that the time ordered integrals should not distinguish which single hop "happened first". Further, notice that all summations here are cancelled by the

Kronecker deltas. Then, calculating the matrix element for these types of transitions,

$$U^{(2)}_{n\to m,p\to q} = \left\langle out\right| \hat{U}^{(2)} \left|in\right\rangle$$

$$\left\langle out\right| \hat{U}^{(2)} \left|in\right\rangle = \frac{-b_{nm}b_{pq}}{4} \int_0^t \mathrm{d}t_1 \int_0^{t_1} \mathrm{d}t_2 \Big(\exp\left(\mathrm{i}\Omega_{mn}(in)t_2\right) \exp\left(\mathrm{i}\Omega_{qp}(in; n\to m)t_1\right) + \exp\left(\mathrm{i}\Omega_{qp}(in)t_2\right) \exp\left(\mathrm{i}\Omega_{mn}(in; p\to q)t_1\right) \Big). \quad (2.30)$$

The integrals can be computed, but the exact form of the solution is omitted as there is little intuition to be gained. These new terms provide a method to calculate a second order estimate for the effective diffusion rate of the spin defect at index n,

$$D_n^{(2)} \approx \frac{1}{6\delta t} {\sum_m}' \left(\left|U^{(1)}_{n\to m} + U^{(2)}_{n\to m}\right|^2 + {\sum_{p,q}}' \left|U^{(2)}_{n\to m,p\to q}\right|^2 \right) r_{nm}^2. \quad (2.31)$$

Calculating higher order terms follows similarly, and enumerating all allowed transitions at a particular order is tedious but intuitive and can be done diagrammatically in a manner which is superficially similar to the diagrammatic approach of a Feynman diagram.

2.2 Computation of Diffusion Coefficients

For the purpose of computation and picking experimental parameters, the computations shall be focused on computing the spin diffusion rates of single crystal of Silicon-29, which has a tetrahedral (diamond) crystal structure. Generation of the crystal is done by inputting the positions of a single unit cell, and then tiling the unit cell repeatedly so that the crystal is represented as a lattice of unit cells. Due to computational constraints, this work focuses on a crystal with $N = 400$ discrete spins, corresponding to a unit cell tiling of $5 \times 5 \times 2$ in x, y, z respectively. For simulations on crystals with N spins at Dyson order n, the required sums have a computation cost $O(\epsilon N \times N^n)$ floating point operations. Plainly, there is a slight advantage at higher values for the polarization.

Once the crystal is generated, the geometric coupling factors r_{ij} and θ_{ij} are computed, which then fully determine the dipolar coupling constants b_{ij}. The time step $\delta t = 10^{-3}$ seconds, as the largest b_{ij} is on the order of 1kHz. Given a set of polarization values and number of trials per instance of polarization, the algorithm randomly initializes each atomic site with an aligned or anti-aligned spin. As previously discussed, this initialization is a

series of Bernoulli trials weighted by the induced probabilities from the initial polarization. These crystal initializations are then used to calculate the required initial values of Ω_{nm}. Computing the value of equation (2.31) for each spin defect within the crystal results in the effective diffusion coefficient for the spin defects in a given trial. Once a diffusion coefficient is computed for each spin, the values are averaged to an effective diffusion rate for the crystal state. The resulting output is then a series of diffusion coefficients indexed by their initial crystal state. These values are then plotted as a function of polarization.

Once the data collection completes (which takes about 64 hours on 16 cores at 3 GHz in Mathematica for 400 spins over 8 values for the polarization with 500 trials per polarization), the resultant collection of diffusion coefficients as a function of polarization are fitted to a regression model, with the goal being a pattern-less residual plot. On the following pages the results of the computations and their regressions are given.

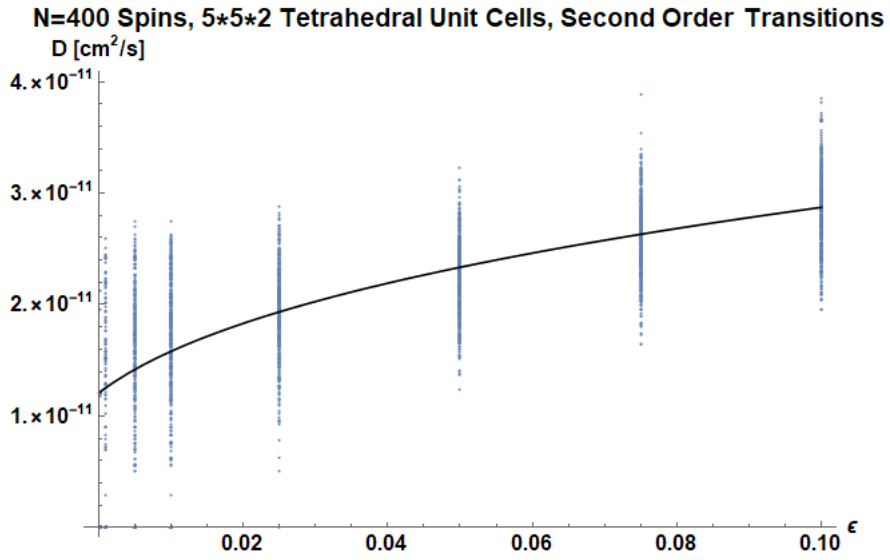

Figure 2.1: Diffusion as a function of polarization for a 400 spin tetrahedral crystal of Silicon–29. The function fitted via regression is given by the function $D(\epsilon) = \sqrt[3]{1.76376 * 10^{-33} + \epsilon \times 2.19458 * 10^{-31}}$ in units of square centimeters per second. the points at various values of polarization indicate computational values sampled during the Monte Carlo simulation.

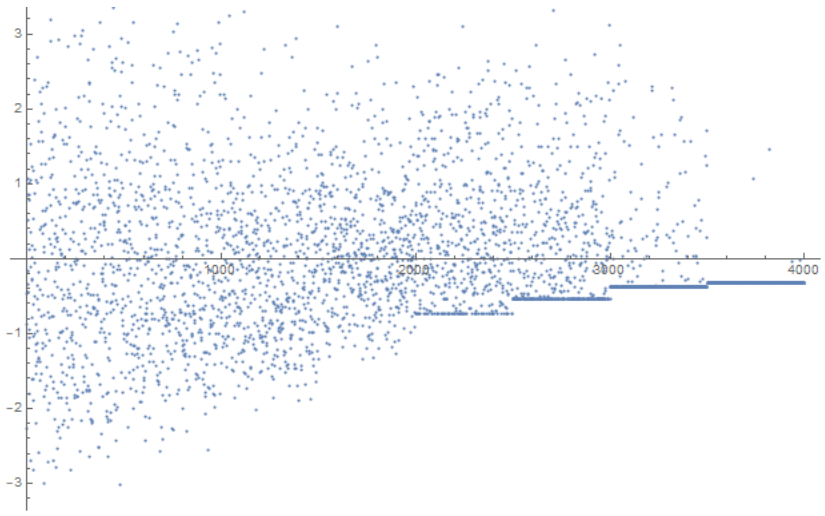

Figure 2.2: Residuals for fit of diffusion as a function of polarization for a 400 spin tetrahedral crystal of Silicon–29, as pictured in figure 2.1.

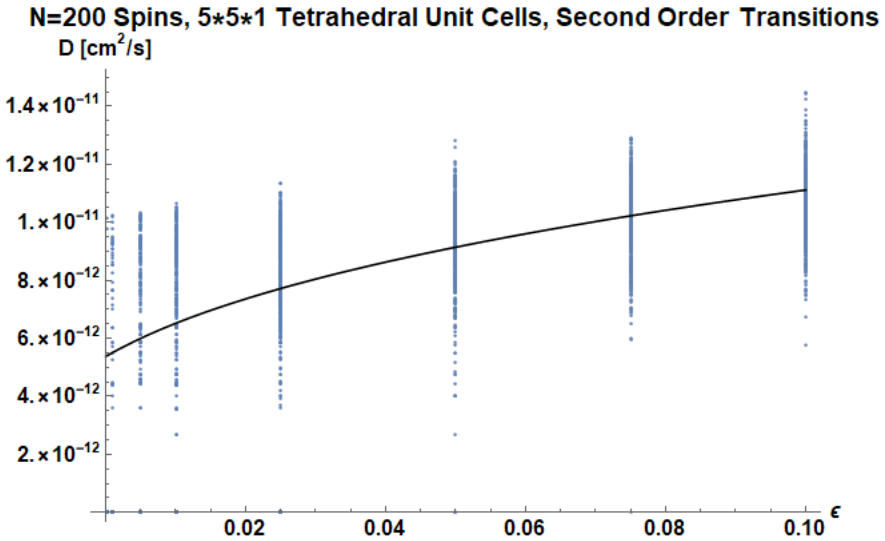

Figure 2.3: Diffusion as a function of polarization for a 200 spin tetrahedral crystal of Silicon–29. The function fitted via regression is given by the function $D(\epsilon) = \sqrt[3]{1.55248 * 10^{-34} + \epsilon \times 1.21782 * 10^{-32}}$ in units of square centimeters per second. the points at various values of polarization indicate computational values sampled during the Monte Carlo simulation.

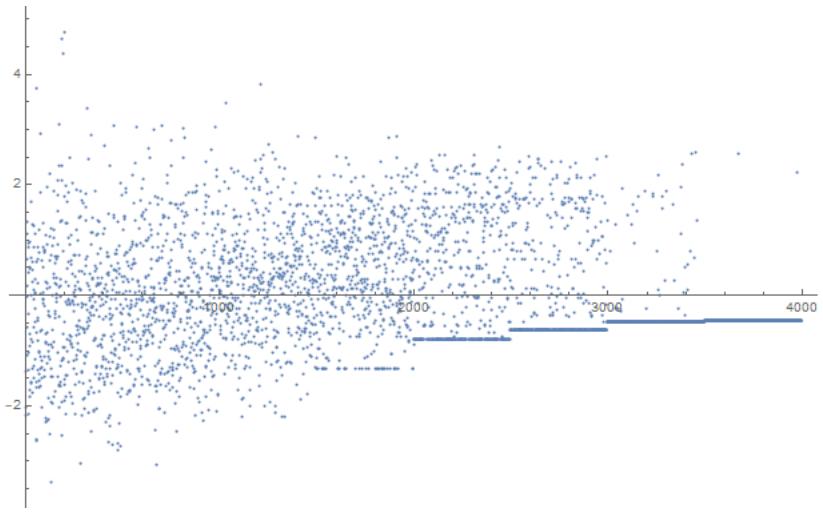

Figure 2.4: Residuals Residuals for fit of diffusion as a function of polarization for a 400 spin tetrahedral crystal of Silicon–29, as pictured in figure 2.3. The clear flat lines in the residual plot are caused by trials in the Monte Carlo simulation which were initialized with no spin excitations, and thus the crystal state had an effective diffusion rate of 0. As polarization increases, this crystal state becomes increasingly common.

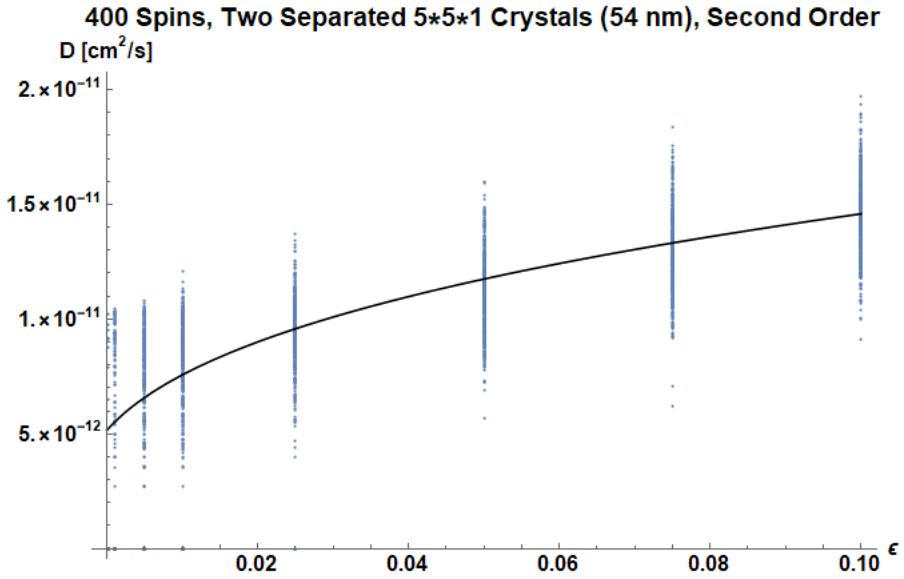

Figure 2.5: Diffusion as a function of polarization for two 200 spin tetrahedral crystals of Silicon–29 separated by 54 nm. The function fitted via regression is given by the function $D(\epsilon) = \sqrt[3]{1.3696 * 10^{-34} + \epsilon \times 2.9675 * 10^{-32}}$ in units of square centimeters per second. the points at various values of polarization indicate computational values sampled during the Monte Carlo simulation.

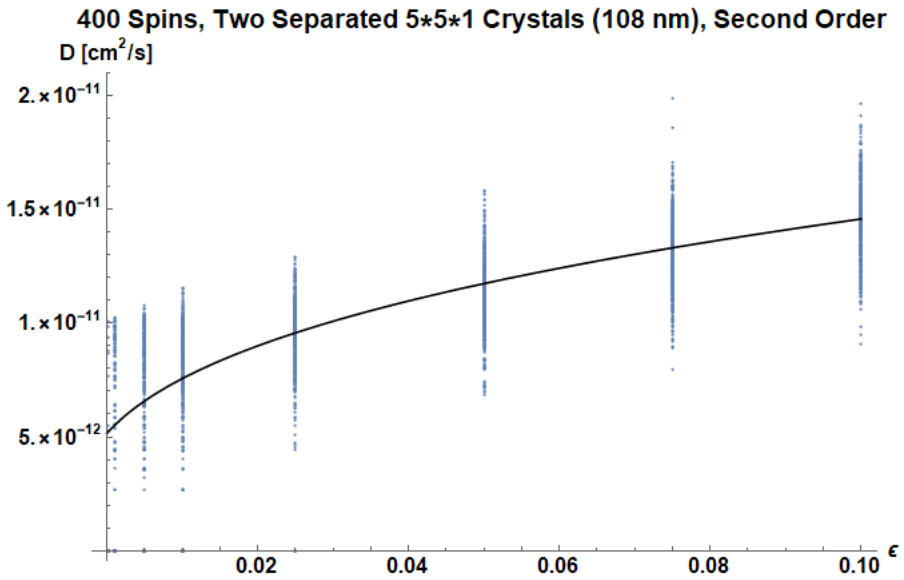

Figure 2.6: Diffusion as a function of polarization for two 200 spin tetrahedral crystals of Silicon–29 seperated by 108 nm. The function fitted via regression is given by the function $D(\epsilon) = \sqrt[3]{1.3633 * 10^{-34} + \epsilon \times 2.9828 * 10^{-32}}$ in units of square centimeters per second. the points at various values of polarization indicate computational values sampled during the Monte Carlo simulation.

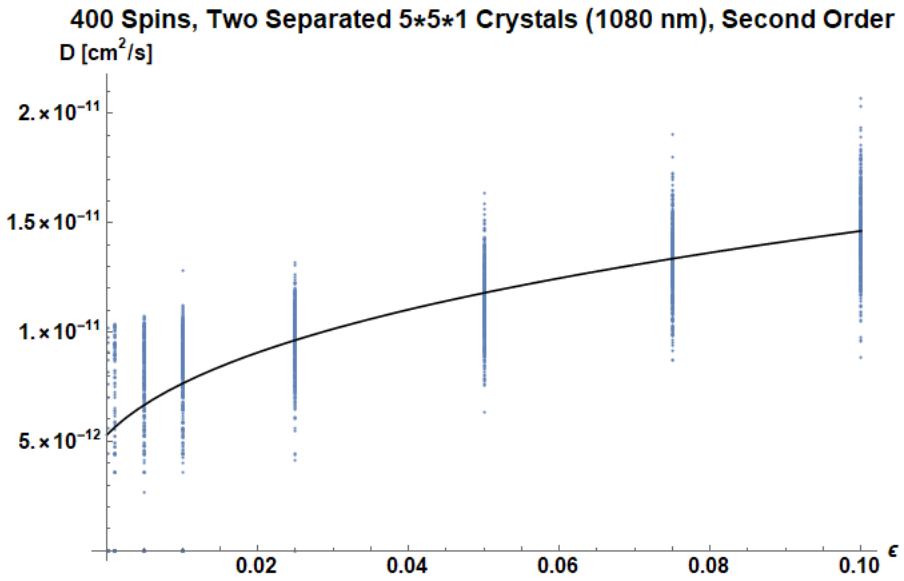

Figure 2.7: Diffusion as a function of polarization for two 200 spin tetrahedral crystals of Silicon–29 separated by 1080 nm. The function fitted via regression is given by the function $D(\epsilon) = \sqrt[3]{1.4851 * 10^{-34} + \epsilon \times 2.98462 * 10^{-32}}$ in units of square centimeters per second. the points at various values of polarization indicate computational values sampled during the Monte Carlo simulation.

Chapter 3

Cavity QED

The predictive power of QED was first demonstrated via the prediction and observation the Lamb shift in 1947, effectively describing the fine structure of the hydrogen atom by including its interaction with the electromagnetic vacuum into the model[30]. With modern experimental design and fabrication techniques, the state of the electromagnetic field has become much more controllable [16]. High quality resonators provide the ability to restrict Maxwell's equations to permit the existence of only single field mode, greatly simplifying the physics and allowing for a direct probe into the quantized structure of the EM field [37]. The dynamics of light confined to a resonator, and the study thereof, is referred to as cavity quantum electrodynamics (cQED), or just cavity QED.

Cavity QED further allows for a precise investigation of light-matter interaction, and the Jaynes-Cummings model first appeared as an attempt to explain spontaneous emission and absorption of photons by atoms [42]. This model's predictions has been highly successful, and the Hamiltonian has been extended to describe the general interaction of two-level systems minimally coupled to bosonic fields, generally referred to as qubits (the two level systems) and photons (the state of the cavity) [42]. In part because the Jaynes-Cummings (JC) model admits analytic solutions, novel light-matter effects such as quantum Rabi oscillations, revivals, and photon anti-bunching have been experimentally verified to high precision [42]. Specific experimental platforms for investigating the structure and physics of the JC Hamiltnonian include Rydberg atoms in optical cavities [31], and superconducting qubits coupled to a superconducting resonator [35].

The JC model only described the interaction of a single qubit with the photon field, the natural extension of this model to an ensembles of qubits is encapsulated by the Tavis-Cummings (TC) model. This model was used by Tavis and Cummings in 1968 to describe

the collective interaction of matter with radiation, describing a highly enhanced photon emission rate in the spin ensemble, which would become known as the phenomenon of super-radiance [48]. Unlike the JC Hamiltonian, the TC Hamiltonian does not directly admit analytic solutions, and as such many techniques for approximating and transforming the Hamiltonian have been used to varying degress of success. In the original paper, Tavis and Cummings recast the energy eigenvector problem as a differential equation which could then be solved numerically or in their case, approximately [48]. More recent works tout exact solutions to the Tavis-Cummings model though they are only "exact" after one takes a series of restrictions and approximations on the structure of the model itself [6]. In terms of a complete description of the eigenvalue and eigenvector structure, none has been presented of ensembles of more than 3 spins [15].

This chapter presents a solution to the problem of determining the structure of TC Hamiltonian. With this solution in hand, various predictions on the phenomena surrounding the Tavis-Cummings model can be recomputed in and arguably more precise manner than ever before. This chapter is broken down into four sections, starting with the energy level structure of the Hamiltonian, then an analysis of thermal states of the model, experimentally motivated dynamics of an initially thermal state, and finally, the cavity's impact and mediation of coherences between spins in a thermal state.

3.1 Structure of the Tavis-Cummings Hamiltonian

The trick to the recipe for diagonalizing the TC model is partly inspired by the solution to the JC Hamiltonian. When faced with diagonalizing an infinite dimensional Hilbert space coupled to a two-level system, writing out a large matrix is hopeless. The saving grace is that the JC model conserves excitations, and so the eigenspace of $\hat{\mathcal{H}}_{JC}$ from equation (1.25) decouples into an infinite ladder of non-interacting two level systems, spanned by $\{|g\rangle|n\rangle, |e\rangle|n-1\rangle\}$ for $n \geq 1$, and a decoupled ground state of $|g\rangle|0\rangle$. To see how to diagonalize the decoupled two level systems, we simply need to set up a matrix representation within these smaller spaces. Computing the action of $\hat{\mathcal{H}}_{JC}$,

$$\begin{aligned}\frac{1}{\hbar}\hat{\mathcal{H}}_{JC}|g\rangle|n\rangle &= (n\omega_0 - 0.5\omega_0 + 0.5\omega_0)|g\rangle|n\rangle + g_0\sqrt{n}|e\rangle|n-1\rangle \\ \frac{1}{\hbar}\hat{\mathcal{H}}_{JC}|e\rangle|n-1\rangle &= ((n-1)\omega_0 + 0.5\omega_0 + 0.5\omega_0)|e\rangle|n-1\rangle + g_0\sqrt{n}|g\rangle|n\rangle\,. \end{aligned} \tag{3.1}$$

Above, the $0.5\omega_0\mathbb{1}$ term was reintroduced to the Hamiltonian so that the dominant energy term would be given by the number of excitations times ω_0. Thus, the action of the

Hamiltonian can be decomposed into a collection non-interacting two level systems:

$$\begin{aligned}\frac{1}{\hbar}\hat{\mathcal{H}}_{JC}\left|g\right\rangle\left|n\right\rangle &= n\omega_0\left|g\right\rangle\left|n\right\rangle + g_0\sqrt{n}\left|e\right\rangle\left|n-1\right\rangle \\ \frac{1}{\hbar}\hat{\mathcal{H}}_{JC}\left|e\right\rangle\left|n-1\right\rangle &= g_0\sqrt{n}\left|g\right\rangle\left|n\right\rangle + n\omega_0\left|e\right\rangle\left|n-1\right\rangle .\end{aligned}$$

The natural matrix representation for this system is given by

$$\begin{bmatrix} n\omega_0 & g_0\sqrt{n} \\ g_0\sqrt{n} & n\omega_0 \end{bmatrix} = \frac{1}{2}\begin{bmatrix} 1 & 1 \\ 1 & -1 \end{bmatrix}\begin{bmatrix} n\omega_0 + g_0\sqrt{n} & 0 \\ 0 & n\omega_0 - g_0\sqrt{n} \end{bmatrix}\begin{bmatrix} 1 & 1 \\ 1 & -1 \end{bmatrix}. \tag{3.2}$$

By orthogonally diagonalizing an arbitrary block of the Hamiltonian, the entire Hamiltonian is now solved, with eigenstates and eigenvalues of

$$\begin{aligned}\left|n,\pm\right\rangle &= \frac{1}{\sqrt{2}}(\left|g\right\rangle\left|n\right\rangle \pm \left|e\right\rangle\left|n-1\right\rangle) \\ \hat{\mathcal{H}}_{JC}\left|n,\pm\right\rangle &= \hbar(n\omega_0 \pm g_0\sqrt{n})\left|n,\pm\right\rangle .\end{aligned} \tag{3.3}$$

As mentioned previously, there is one additional eigenstate, $\left|g\right\rangle\left|0\right\rangle$, with eigenvalue 0. It is clear that this list is exhaustive, as the given eigenstates span the entire composite Hilbert space. These spin-cavity eigenstates are often called "dressed states", or equivalently that the spin-cavity energy levels "hybridize" [37]. This hybridization can be seen directly in figure 3.1.

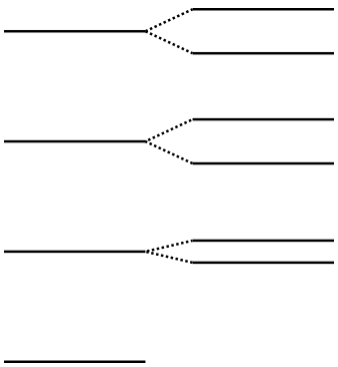

Figure 3.1: Graphical depiction of the hybridization of energy levels in the Jaynes-Cummings ladder. A bar represents a state (or states), with energy loosely corresponding to their vertical height in the diagram, relative to the ground state, given as the lowest lying black bar.

Unfortunately, the trick of diagonalizing the TC model simply by breaking down the Hamiltonian into constant excitation subspaces will not be as fruitful. Given N spin-1/2 particles in a TC model, the number of states present at the k-th excitation level grows like a sum of binomial coefficients up until the $N+1$ st level, where there will be all 2^N possible spin states present for each excitation level after this point. To clarify, the dimension of the k-th excitation level (for $k < N+1$), called D_k, is given by

$$D_k = \sum_{k'=0}^{k} \binom{N}{k'}. \tag{3.4}$$

For $k \geq N+1$, it is then clear that $D_k = 2^N$. For many experimentally reasonable values of N, diagonalizing a set of matrices with this sort of scaling behaviour is hopeless past the first few excitation levels.

The solution to this problem is to appeal to a symmetry that exists solely on the spins. Since the spins are energetically identical, total angular momentum $\hat{J}^2 = \hat{J}_x^2 + \hat{J}_y^2 + \hat{J}_z^2$ commutes with the TC Hamiltonian. This means that total angular momentum of the spins is a conserved quantity and serves as an additional good quantum number for eigenstates of the Hamiltonian. $\hat{J}^2$ has eigenvalues of $j \in \{N/2, N/2-1, \cdots, \{N/2\}\}$, where $\{N/2\}$ denotes the fractional part of $N/2$,

$$\{N/2\} := N/2 - \lfloor N/2 \rfloor. \tag{3.5}$$

A quick counting argument will reveal that the the listed angular momentum subspaces do not account for all 2^N possible basis states. In truth, there are many distinct copies of each angular momentum subspace, and when accounting for the degeneracies the full dimensionality of 2^N is reached. The number of energetically degenerate copies of each angular momentum subspace are a result of repeatedly block diagonalizing by irreducible representations. In physics, computing the irreducible representations of the tensor product of two angular momentum representations is extremely common, and appealing the to Clebsch-Gordan tables allows for easy computations [32]. For example,

$$\begin{aligned} \frac{1}{2} \otimes \frac{1}{2} &\cong 1 \oplus 0 \\ \frac{1}{2} \otimes \frac{1}{2} \otimes \frac{1}{2} &\cong (1 \oplus 0) \otimes \frac{1}{2} \cong \frac{3}{2} \oplus \frac{1}{2} \oplus \frac{1}{2}. \end{aligned}$$

Above, it should be understood that this shorthand notation represents that the tensor product of two spin-1/2 Hilbert spaces is isomorphic to the direct sum of a spin-1 and

a spin-0 Hilbert space, and similarly for the second equation. Repeating this process N times for each spin is unwieldy and inefficient with regard to keeping track of the number of copies of a given angular momentum space. The graphical solution to this problem is a hybrid of quantum chemistry and group theory due to Yamanouchi and Kotani[38], who created a branching diagram for computing the number of copies of a given angular momentum subspace.

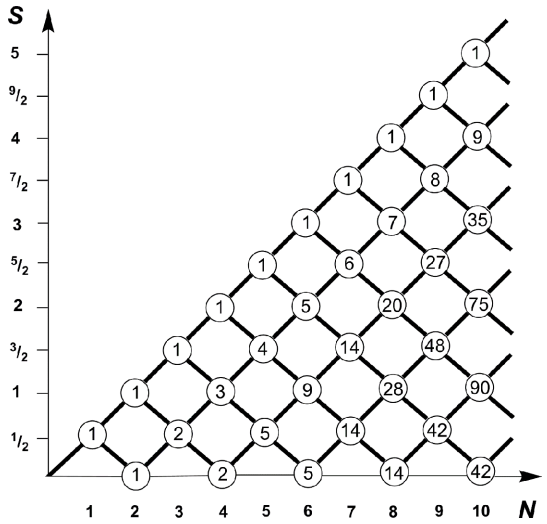

Figure 3.2: Yamanouchi-Kotani branching diagram for computing the number of copies of a given angular momentum subspace for an ensemble of N spin-1/2 particles. Figure taken from [10].

To produce figure 3.2, label the horizontal axis with integer values, denoting the number of spins, and label the vertical axis with integer and half integer values, denoting angular momentum subspaces. The base case is simply that a single spin is spin-1/2, and there are no degeneracies, so a 1 is places at this point on the graph. then draw lines connecting the adjacent angular momentum spaces one value of N to the right, adding together the degeneracies of the originating angular momentum subspaces to compute the number of degenerate subspaces at that particular intersection.

From figure 3.2, one can appeal to intuition and write down a combinatorial formula for the number of copies of the j angular momentum subspace given an identical ensemble of N spin-1/2 particles. To compute the number at a vertical position j, and horizontal position N, one counts the number of total paths that terminate at or above (N, j), and

subtract off all paths that terminate at or above $(N, j+1)$:

$$d_j = \binom{N}{N/2-j} - \binom{N}{N/2-(j+1)} = \frac{N!(2j+1)}{(N/2-j)!(N/2+j+1)!}. \tag{3.6}$$

It is valid to wonder what, if anything, distinguishes the otherwise energetically degenerate copies of each angular momentum subspace. The solution is to apply Schur-Weyl duality [53], which loosely states that each irreducible representation appearing in the direct sum decomposition of $\frac{1}{2}^{\otimes N}$ is paired with a representation of S_N, the permutation group of degree N. Further, each of these pairs is labeled by a standard Young tableau, of at most two rows with N boxes. A standard Young tableau on N symbols is a graphical depiction of a partition of N, formed by stacking rows, totalling N boxes across all rows. In particular from the top of the diagram to bottom, the number of boxes in each row should be decreasing. These boxes are then labeled by integer values from 1 to N, such that the labels are strictly increasing from left to right, as well as top to bottom. An example of a standard Young tableau is given below.

1	3	4
2	5	

The shape of the Young tableau determines the dimension of the angular momentum irreducible representation, and then the entries of the tableaux label the different copies. To compute the angular momentum subspace of a given standard Young tableau, the formula is to take one half the difference of the number of boxes in the top row and the number of boxes in the bottom row. Since these are standard Young tableaux, the top row must have an equal or greater amount of boxes, and thus the angular momentum is always non-negative. A particular integer labelling of these boxes determines the spin exchange symmetries of any given degenerate subspace, and the number of valid label assignments is then equal to the number of degenerate copies of that particular angular momentum subspace. In the previously given example of a standard Young tableau,

1	3	4
2	5	

corresponds to a particular instance of the $j = 1/2$ subspace for $N = 5$ spin-1/2 particles. There are four other valid label assignments, adding up to 5 degenerate copies of the $j = 1/2$ subspace for $N = 5$.

Without digressing too far into the representation theory of finite groups, the most pertinent implication of Schur-Weyl duality to this work is that each subspace is uniquely

labeled by which permutations under spin labeling leaves that subspace invariant. Thus, irreducible representations of the general linear group (an angular momentum subspace) pair with irreducible representations of the symmetric group (a permutation symmetry of the labeling of the spin particles).

The simplest example of the pairing of the symmetric group with the general linear group manifests within the $j = N/2$ subspace, often referred to as the fully symmetric subspace, since each state contained in this subspace is invariant under any relabeling of the N spin-1/2 particles. In the case of two spin-1/2 particles, the symmetric group has two irreducible representations: fully symmetric and fully anti-symmetric. Because of the small size of the example, all of the basis states can be listed in full generality. Using the notation of $|j, m\rangle$ to denote the total angular momentum j and z-component m state, and omitting tensor products for simplicity, the basis states are listed below:

$$\begin{aligned}
|1, -1\rangle &= |g\rangle\,|g\rangle \\
|1, 0\rangle &= \frac{1}{\sqrt{2}}(|g\rangle\,|e\rangle + |e\rangle\,|g\rangle) \\
|1, 1\rangle &= |e\rangle\,|e\rangle \\
|0, 0\rangle &= \frac{1}{\sqrt{2}}(|g\rangle\,|e\rangle - |e\rangle\,|g\rangle).
\end{aligned}$$

Above, the angular momentum $j = 1$ space, when written as a tensor product of the consistent spin-1/2 basis states, is indeed invariant under exchange of spins. On the other hand, the $j = 0$ state gains a minus sign under spin exchange and thus is anti-symmetric under this permutation. In summation, the $j = 1$ angular momentum subspace is invariant under every spin relabeling (exchange and identity), while the $j = 0$ angular momentum subspace is only invariant under the identity relabeling, where no labels change.

The last example given will be $N = 3$, as it is the smallest case with multiple copies of a given angular momentum subspace. The fully symmetric subspace is given below:

$$\begin{aligned}
|\frac{3}{2}, -\frac{3}{2}\rangle &= |ggg\rangle \\
|\frac{3}{2}, -\frac{1}{2}\rangle &= \frac{1}{\sqrt{3}}(|gge\rangle + |geg\rangle + |egg\rangle) \\
|\frac{3}{2}, \frac{1}{2}\rangle &= \frac{1}{\sqrt{3}}(|gee\rangle + |eeg\rangle + |ege\rangle) \\
|\frac{3}{2}, \frac{3}{2}\rangle &= |eee\rangle\,.
\end{aligned}$$

Notice that each state is completely unchanged under reordering of Hilbert spaces. There are two spin-1/2 subspaces that can be simultaneously formed. The standard way to compute the representations of these states are to use the Clebsch-Gordan tables, given in figure 3.3.

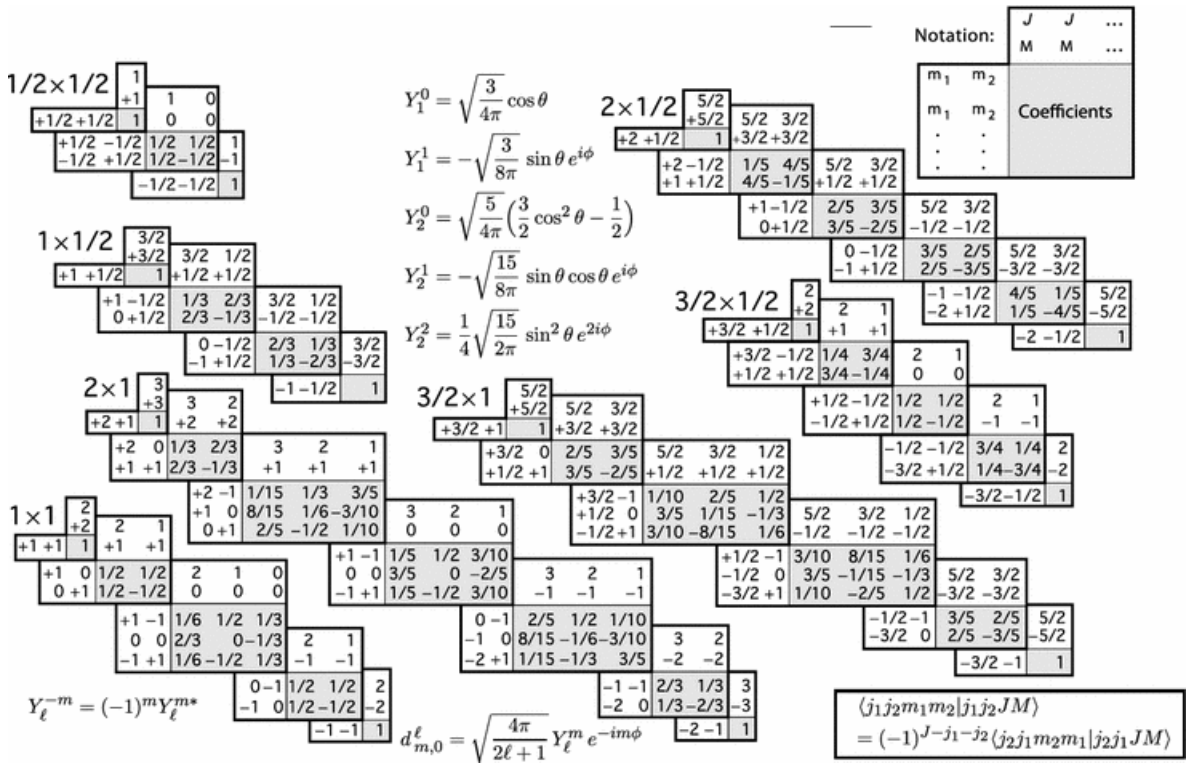

Figure 3.3: Classical collection of Clebsch-Gordan tables, taken from [32].

The following spin-1/2 subspace was formed by combining a composite spin-1 with a spin-1/2:

$$|\frac{1}{2},-\frac{1}{2}\rangle_1 = \frac{1}{\sqrt{6}}(|egg\rangle + |geg\rangle - 2\,|gge\rangle)$$
$$|\frac{1}{2},\frac{1}{2}\rangle_1 = \frac{1}{\sqrt{6}}(2\,|eeg\rangle - |gee\rangle - |ege\rangle).$$

The Young tableaux corresponding to the above angular momentum subspace is given by

$$\begin{array}{|c|c|}\hline 1 & 2 \\ \hline 3 \\ \cline{1-1}\end{array}.$$

The energetically indistinguishable copy of the above spin-1/2 subspace, formed by combining a composite spin-0 with a spin-1/2, is given below:

$$|\frac{1}{2},-\frac{1}{2}\rangle_2 = \frac{1}{\sqrt{2}}(|egg\rangle - |geg\rangle)$$
$$|\frac{1}{2},\frac{1}{2}\rangle_2 = \frac{1}{\sqrt{2}}(|ege\rangle - |gee\rangle),$$

which has a corresponding Young tableaux of

$$\begin{array}{|c|c|}\hline 1 & 3 \\ \hline 2 \\ \cline{1-1}\end{array}.$$

For completeness, the Young tableaux corresponding to the spin-3/2 subspace is given by

$$\begin{array}{|c|c|c|}\hline 1 & 2 & 3 \\ \hline\end{array}.$$

The above examples provide valuable insight into the details hiding behind the decomposition into irreducible representations of angular momentum. These subspaces are effectively indistinguishable experimentally if one restricts the observables to collective operators, as their actions are identical across these subspaces, and will thus be often referred to as degenerate subspaces. Further, each angular momentum subspace, regardless of their dimension, are completely non-interacting under the Tavis-Cummings Hamiltonian. In fact, any Hamiltonian which can be written entirely in terms of the collective angular momentum operators will allow no transitions between angular momentum subspaces.

Given that distinguishing the actual micro-state configurations of a particular angular momentum subspace is nigh indeterminable, it is important to note that the details of a particular configuration in no way impact one's ability to compute the action of the Hamiltonian. The utility of the above discussion has been that one can determine which angular momentum subspaces will occur, how many copies of each occur, and their respective energies. For instance, given N spin-1/2 particles, the angular momentum subspace(s) indexed by j has $2j+1$ states, each separated in energy by $\hbar\omega_0$, with the ground state having an energy of $-j\hbar\omega_0$, which is energetically separated from the lowest possible energy spin state by $(N/2-j)\hbar\omega_0$. Each state in subspace then is written as $|j,m\rangle$, with $m \in \{-j,-j+1,\cdots,j\}$, and the action of the $\mathfrak{sl}(2;\mathbb{C})$ operators appearing in the TC Hamiltonian can be computed via the commutation relations, or looked up [32]:

$$\hat{J}_z\,|j,m\rangle = m\,|j,m\rangle \tag{3.7}$$
$$\hat{J}_\pm\,|j,m\rangle = \sqrt{j(j+1)-m(m\pm1)}\,|j,m\pm1\rangle\,. \tag{3.8}$$

By ignoring the labels on states coming from different subspaces of the same angular momentum, and instead including the degeneracies as statistical weights where ever necessary, the problem size is reduced immensely. Without this reduction of size, there are 2^N spin eigenstates to consider, whereas the reduction allows one to only consider $O(N^2)$ eigenstates, as computed below.

$$\sum_{j=\{N/2\}}^{N/2} (2j+1) = O(N^2).$$

Given that one can describe the entire spin ensemble without loss of information as a collection of non-interaction angular momentum subspaces, it remains only to consider an arbitrary angular momentum subspace j stemming from N spins, coupled indistinguishably to a single mode EM field. To better visualize the coming procedure, consider the energy level diagram in figure 3.4. The horizontal direction is labeled by Fock states, and the vertical direction corresponds to the number of excitations present.

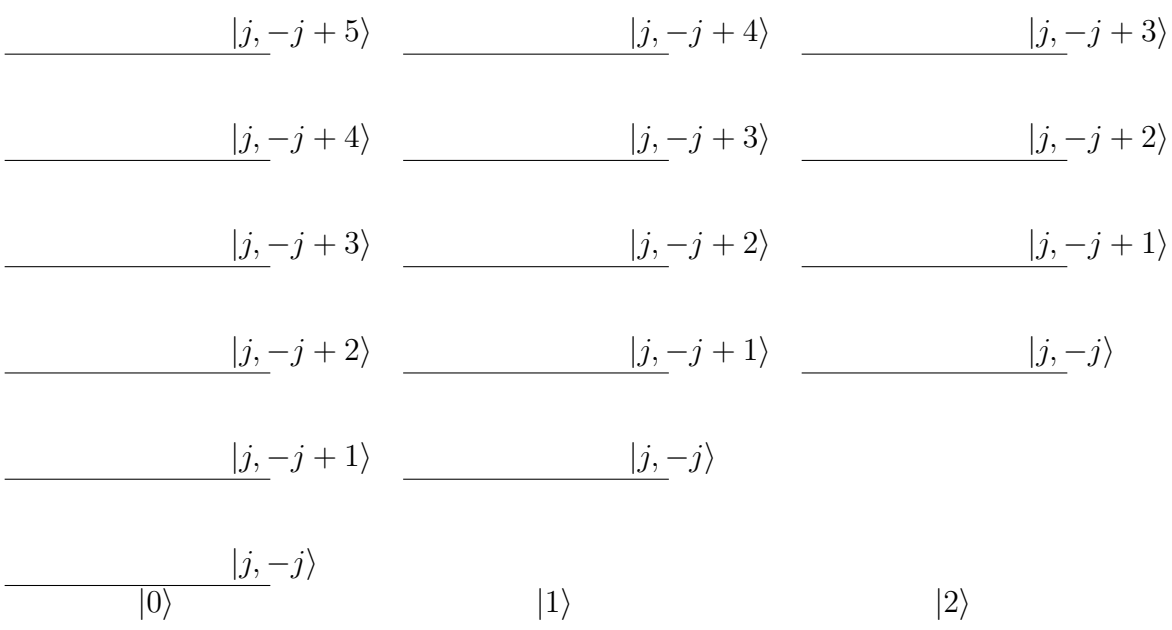

Figure 3.4: Partial sketch of the energy level diagram for an angular momentum subspace and a single mode EM field, without considering $\hat{\mathcal{H}}_{int}$. The ladders terminate vertically at $2j+1$ rungs, and continue horizontally infinitely.

Since the interaction Hamiltonian,

$$\hat{\mathcal{H}}_{int} = \hbar g_0(\hat{a}^\dagger \hat{J}_- + \hat{a}\hat{J}_+), \tag{3.9}$$

preserves angular momentum and the number of excitations, it can be immediately understood that $\hat{\mathcal{H}}_{int}$ can only couple levels in the energy level diagram of figure 3.4 which are on the same horizontal plane. That is, each of these excitation levels can be treated as independent blocks when re-diagonalizing under the interaction Hamiltonian. This induces a set of bases under which one can simply compute matrix representations for each excitation block. It is important to recall that the lowest lying energy state in this ladder is not a 0 excitation state, rather it is a

$$k_0(j) := N/2 - j \tag{3.10}$$

excitation state. The general trend of these bases as a function of k excitations above the ground, $k_0(j)$, is given below:

$$\begin{aligned}
\mathcal{B}_{j,0} &= \{|j,-j\rangle |0\rangle\} \\
\mathcal{B}_{j,1} &= \{|j,-j\rangle |1\rangle, |j,-j+1\rangle |0\rangle\} \\
\mathcal{B}_{j,2} &= \{|j,-j\rangle |2\rangle, |j,-j+1\rangle |1\rangle, |j,-j+2\rangle |0\rangle\} \\
&\vdots \\
\mathcal{B}_{j,2j} &= \{|j,-j\rangle |2j+1\rangle, |j,-j+1\rangle |2j\rangle, \cdots, |j,j\rangle |0\rangle\} \\
&\vdots \\
\mathcal{B}_{j,k} &= \{|j,-j\rangle |k\rangle, |j,-j+1\rangle |k-1\rangle, \cdots, |j,j\rangle |k-2j\rangle\}.
\end{aligned} \tag{3.11}$$

It is then clear that the effective excitation basis increases in dimension by one for each level of excitation above the angular momentum ground state, until the dimension saturates at $2j+1$ for excitations above $2j$. For bookkeeping, define the dimension of the vector space spanned by these bases as

$$D_{j,k} = |\mathcal{B}_{j,k}| = \min\{k+1, 2j+1\}. \tag{3.12}$$

Fixing this ordering of the basis is natural with regard to appealing to intuition, and as it turns out, is also natural when it comes to setting up a coupling matrix. Each state in this infinite collection of bases is diagonal under $\hat{\mathcal{H}}_0$, and thus the action of $\hat{\mathcal{H}}_0$ is entirely determined by the number of excitations present. Since each basis is a set of constant excitations, this serves only as a constant multiple times the identity, and can be safely

ignored for diagonalization purposes. In general, given a diagonalizable matrix A such that $A = B + c\mathbb{1}$, for some diagonalizable matrix B and scalar c, then if B is diagonalized by P then so is A. As a quick proof,

$$D = P^{-1}BP = P^{-1}(A - c\mathbb{1})P = P^{-1}AP - c\mathbb{1} \implies P^{-1}AP = D + c\mathbb{1}. \tag{3.13}$$

Given this fact, it suffices to only consider a matrix representation of $\hat{\mathcal{H}}_{int}$ with respect to each of these bases. Turning back to the energy level diagram of figure 3.4, it is clear that only horizontally adjacent states have a non-zero matrix element, since the photon and spin ladder operators only change the excitation level of each Hilbert space by one. The implication of this, paired with the fixed order of the bases in equation (3.11), is that the coupling matrix is symmetric and tridiagonal with a 0 diagonal. That is,

$$L(j,k) = \begin{bmatrix} 0 & l_0(j,k) & & & \\ l_0(j,k) & 0 & l_1(j,k) & & \\ & l_1(j,k) & 0 & \ddots & \\ & & \ddots & \ddots & l_{n-1}(j,k) \\ & & & l_{n-1}(j,k) & 0 \end{bmatrix}, \tag{3.14}$$

where $n = D_{j,k} - 1$, and for $i \in \{0, 1, \cdots, n-1\}$,

$$\begin{aligned} l_i(j,k) &= \langle j, -j+i| \langle k-i| \hat{\mathcal{H}}_{int} |j, -j+i-1\rangle |k-i+1\rangle \\ &= \hbar g_0 \sqrt{j(j+1) - (-j+i-1)(-j+i)}\sqrt{k-i+1} \\ &= \hbar g_0 \sqrt{\big(2ij - i(i-1)\big)\big(k-i+1\big)}. \end{aligned} \tag{3.15}$$

Thus, a general solution to the Tavis-Cummings Hamiltonian is mathematically equivalent to a solution to diagonalizing $L(j,k)$ for arbitrary allowed values of j and k. $L(j,k)$ is known as a Jacobi operator in linear algebra literature, connected closely to the study of orthogonal polynomials, and finding their eigenvalues is in general not possible to do in a closed form [49]. In fact, a theorem due to Jacobi states that any real symmetric matrix can be transformed into a matrix of tridiagonal form, which, if a general solution for the eigenvalues existed, would seemingly contradict the result of Galois on the general insolubility of polynomials of degree 5 or greater [36]. Interestingly enough there exists a recurrence relation for the characteristic polynomial of Jacobi operators, which can be directly applied to the coupling matrix $L(j,k)$. Let $\det(L(j,k) - \lambda\mathbb{1}) = f_{n+1}$, then

$$f_{n+1} = -\lambda f_n - l_n(j,k)^2 f_{n-1}, \quad f_1 = 1, \quad f_0 = 0. \tag{3.16}$$

The above formula is directly derived from applying the Laplace expansion definition of a matrix determinant to $L(j,k)$. It is through the recurrence relation for the determinant (and thus the characteristic polynomial) that the correspondence between Jacobi operators and orthogonal polynomials is made clear [49].

The state of the art of determining the eigenvalues of Jacobi matrices is quite outside the scope of this work, and a quick attempt at applying theoretical tools from that field did not immediately yield promising results. It would seem that an analytic solution to the Tavis-Cummings problem is still out of reach. That being said, there is a lot of new structure that can be exploited here for the efficient extraction of relevant information. Dual to the theoretical tools, there exist powerful computational tools for finding the eigenvalues of Jacobi operators, namely there exists a single thread eigenvalue algorithm with runtime $O(n \log n)$ on an n dimensional operator[9]. This would require particularizing for all values of j and k of interest, though the efficiency gain is still drastic over a naive approach ignoring the non-interacting block structure of the Hamiltonian.

Before any numerical analysis, there are still some valuable insights which can be extracted from these coupling matrices. From theoretical work in numerical analysis, this form of matrix is also well known and referred to as a hollow tridiagonal matrix. A particularly useful property is that the eigenvalues of the coupling matrix come in opposite signed pairs – that is, if λ is an eigenvalue of $L(j,k)$, then so is $-\lambda$ [51]. In particular if $D_{j,k}$ is odd, then $L(j,k)$ has a 0 eigenvalue. This can be confirmed by using the recursive determinant formula with $\lambda = 0$,

$$\begin{aligned}\det(L(j,k)) &= f_{n+1} \\ &= -l_n(j,k)^2 f_{n-1} \\ &= l_n(j,k)^2 l_{n-2}(j,k)^2 f_{n-3} \\ &= \cdots .\end{aligned}$$

In the above equation, if $D_{j,k}$ is odd, then n is even and thus the recursion terminates with $f_0 = 0$ multiplying the recursive product chain, leading to a 0 determinant, which necessitates the existence of at least one 0 eigenvalue, as expected.

The fact that the spectrum,

$$\Lambda(j,k) = \{\lambda \,|\, L(j,k)\boldsymbol{v} = \lambda \boldsymbol{v}, \boldsymbol{v} \neq 0\}, \tag{3.17}$$

of the coupling matrix is symmetric about zero also means that the respective arithmetic mean is 0. This can equivalently seen by relating the sum of eigenvalues to the trace:

$$\langle \Lambda(j,k) \rangle = \frac{1}{n+1} \sum_{i=0}^{n} \lambda_i = \frac{\operatorname{tr} L(j,k)}{n+1} = 0. \tag{3.18}$$

In lieu of a complete description of the spectrum, a statistical description may suffice. The statistical distribution of a single coupling matrix on its own is not particularly insightful, as it is just a symmetric sum of delta peaks. The statistics of all the energy levels within an excitation level across all angular momentum subspaces has the opportunity to be much more insightful. Since the mean of the splittings within each angular momentum subspace is 0, the mean of the entire distribution will be 0. The variance of a given angular momentum subspace can be shown to be proportional to $\operatorname{tr} L(j,k)^2$

$$\begin{aligned}\operatorname{Var}(\Lambda(j,k)) &= \left\langle \Lambda(j,k)^2 \right\rangle - \left\langle \Lambda(j,k) \right\rangle^2 \\ &= \left\langle \Lambda(j,k)^2 \right\rangle \\ &= \frac{1}{n+1} \sum_{i=0}^{n} \lambda_i^2 \\ &= \frac{1}{n+1} \operatorname{tr} L(j,k)^2. \end{aligned} \tag{3.19}$$

The square of the coupling matrix can be computed exactly, as it is still a sparse matrix, this time a pentadiagonal matrix. The exact form is given below, suppressing the dependence on j and k for brevity.

$$L(j,k)^2 = \begin{bmatrix} l_1^2 & 0 & l_1 l_2 & & & \\ 0 & l_1^2 + l_2^2 & 0 & l_2 l_3 & & \\ l_1 l_2 & 0 & \ddots & \ddots & \ddots & \\ & l_2 l_3 & \ddots & \ddots & \ddots & l_{n-1} l_n \\ & & \ddots & \ddots & l_{n-1}^2 + l_n^2 & 0 \\ & & & l_{n-1} l_n & 0 & l_n^2 \end{bmatrix} \tag{3.20}$$

Then, the trace of the square of the coupling matrix is simply the twice the sum of the squares of all the $l_i(j,k)$ coefficients.

$$\operatorname{tr} L(j,k)^2 = 2 \sum_{i=1}^{n} l_i(j,k)^2 = 2\hbar^2 g_0^2 \sum_{i=1}^{n} \big(2ij - i(i-1)\big)\big(k - i + 1\big). \tag{3.21}$$

Conveniently, the above sum can be computed exactly using the following formulae:

$$\sum_{i=1}^{n} i = \frac{n(n+1)}{2}$$
$$\sum_{i=1}^{n} i^2 = \frac{n(n+1)(2n+1)}{6}$$
$$\sum_{i=1}^{n} i^3 = \frac{n^2(n+1)^2}{4}.$$

Rearranging the coupling coefficients for convenience,

$$\begin{aligned}\frac{1}{\hbar^2 g_0^2} l_i(j,k)^2 &= \big(2ij - i(i-1)\big)\big(k - i + 1\big) \\ &= i(i-(2j+1))(i-(k+1)) \\ &= i^3 - i^2(2j+1+k+1) + i(2j+1)(k+1).\end{aligned}$$

Thus,

$$\begin{aligned}\operatorname{tr} L(j,k)^2 = 2\hbar^2 g_0^2 \Bigg(&\frac{n^2(n+1)^2}{4} - ((2j+1)+(k+1))\frac{n(n+1)(2n+1)}{6} \\ &+ (2j+1)(k+1)\frac{n(n+1)}{2}\Bigg).\end{aligned} \tag{3.22}$$

Recall that n is a function of j and k through the fact that $n = D_{j,k} - 1$. Simplifying further and reintroducing the j and k dependence,

$$\begin{aligned}\operatorname{tr} L(j,k)^2 = \frac{\hbar^2 g_0^2 D_{j,k}(D_{j,k}-1)}{3}\Bigg(&\frac{3}{2} D_{j,k}(D_{j,k}-1) - ((2j+1)+(k+1))(2D_{j,k}-1) \\ &+ 3(2j+1)(k+1)\Bigg).\end{aligned} \tag{3.23}$$

Then, the variance can be written explicitly:

$$\begin{aligned}\operatorname{Var}\Lambda(j,k) = \frac{\hbar^2 g_0^2 (D_{j,k}-1)}{3}\Bigg(&\frac{3}{2} D_{j,k}(D_{j,k}-1) - ((2j+1)+(k+1))(2D_{j,k}-1) \\ &+ 3(2j+1)(k+1)\Bigg).\end{aligned} \tag{3.24}$$

When dealing with multiple angular momentum subspaces, it is vital to note that the k in equation (3.24) indexes the number of excitations above the angular momentum ground state, which itself has $k_0(j) = N/2 - j$ intrinsic spin excitations. This further implies that for a given excitation value, only the angular momentum subspaces with $k_0(j) \geq 0$ have energy levels at this this excitation level. Given the basic characteristics of the energy level splittings previously discusses in this section, it is straightforward to provide a partial sketch of the energy level diagram for the full Tavis-Cummings Hamiltonian.

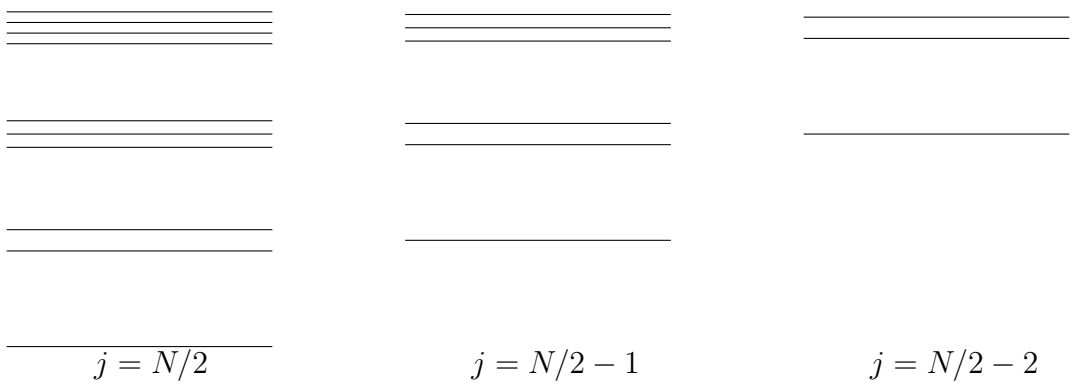

Figure 3.5: Sketch of the energy level diagram for the first three angular momentum subspaces and their respective first four excitation subspaces in the Tavis-Cummings Hamiltonian. Excitations increase moving vertically upwards, and angular momentum decreases moving horizontally to the right, as labeled in the sketch.

The energy level splittings of figure 3.5 are exaggerated, since the splittings are of order g_0, whereas the subspaces are split by ω_0, and it has been enforced that $g_0 \ll \omega_0$. Regardless, the exaggeration allows for a cleaner visualization of the split levels in each subspace at a given excitation. The number of split levels in subspace j at $k_0(j) + k$ excitations is given by $D_{j,k}$.

One can actually solve the for the energy splittings exactly for the first few excitation levels of an arbitrary angular momentum subspace j. Recall that $L(j,k)$ has off diagonal components $l_i(j,k)$, given by

$$l_i(j,k) = \hbar g_0 \sqrt{i\big((2j+1) - i\big)\big((k+1) - i\big)}. \tag{3.25}$$

For simplicity, take $\hbar g_0 = 1$, as they simply determine the units of the energy shifts. For $k = 0$ excitations above the ground, there is no splitting and the coupling matrix is a 1x1 0 matrix, so $\Lambda(j,0) = \{0\}$. Each next subspace will have an additional dimension on the

matrix until the dimension reaches $2j+1$, such that $k=1$ excitation above the ground, the coupling matrix can be written as

$$L(j,1) = \begin{bmatrix} 0 & \sqrt{2j} \\ \sqrt{2j} & 0 \end{bmatrix}. \tag{3.26}$$

Finding the eigenvalues of the above matrix and introducing the scaling factors, one finds,

$$\Lambda(j,1) = \{-\hbar g_0\sqrt{2j}, \hbar g_0\sqrt{2j}\}. \tag{3.27}$$

Continuing to $k=2$,

$$L(j,2) = \begin{bmatrix} 0 & \sqrt{2j}\sqrt{2} & 0 \\ \sqrt{2j}\sqrt{2} & 0 & \sqrt{4j-2} \\ 0 & \sqrt{4j-2} & 0 \end{bmatrix}, \tag{3.28}$$

yielding

$$\Lambda(j,2) = \{-\hbar g_0\sqrt{8j-2}, 0, \hbar g_0\sqrt{8j-2}\}. \tag{3.29}$$

In principle this process can be repeated until at least $k=8$ excitations above the ground, where there will be 4 distinct oppositely signed pairs of eigenvalues and one zero eigenvalue, which can be reduced to a fourth order polynomial. For $k=9$ and beyond, one can simplify to a fifth order polynomial, which has no general algebraic solution. If further reductions of order exist, they would indicate the possibility of an exactly solvable model. As a final computation, consider $k=3$ excitations above the ground

$$L(j,3) = \begin{bmatrix} 0 & \sqrt{2j}\sqrt{3} & 0 & 0 \\ \sqrt{2j}\sqrt{3} & 0 & \sqrt{4j-2}\sqrt{2} & 0 \\ 0 & \sqrt{4j-2}\sqrt{2} & 0 & \sqrt{6j-6} \\ 0 & 0 & \sqrt{6j-6} & 0 \end{bmatrix}, \tag{3.30}$$

yielding

$$\Lambda(j,3) = \Big\{ -\hbar g_0\sqrt{5(2j-1)+\sqrt{64j^2-64j+25}}, -\hbar g_0\sqrt{5(2j-1)-\sqrt{64j^2-64j+25}}, \\ \hbar g_0\sqrt{5(2j-1)-\sqrt{64j^2-64j+25}}, \hbar g_0\sqrt{5(2j-1)+\sqrt{64j^2-64j+25}}\Big\}. \tag{3.31}$$

While the next few excitation levels have closed form solutions for the energy level splittings, they become increasingly unwieldy, while the process to compute them remains

identical. For this reason, they are omitted. As it stands, the computed splittings determine the entire energy level structure for the first four excitation levels across all angular momentum subspaces. The more useful interpretation with regards to determining low temperature behavior of the Gibbs thermal sate is that the Hilbert space is fully solved for all eigenstates within four excitation levels above the true ground state. Graphically, these states are represented by figure 3.7, which includes the degeneracies of the respective angular momentum subspaces.

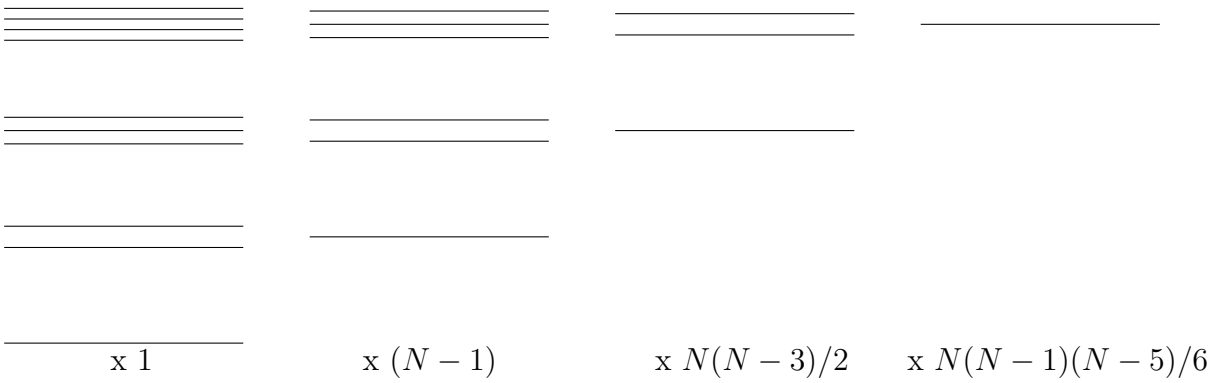

Figure 3.6: Sketch of the energy level diagram for the first four angular momentum subspaces and the first four excitation subspaces in the Tavis-Cummings Hamiltonian. Excitations increase moving vertically upwards, and angular momentum decreases moving horizontally to the right. This sketch includes the degeneracy of the angular momentum subspaces as label, illustrating there is only a single copy of the $j = N/2$ subspace, $N-1$ copies of the $j = N/2-1$ subspace, and so on.

Figure 3.7: Graphical representation of the energy levels determined with previously computed closed form splittings, labelled horizontally by the number of degeneracies of each angular momentum subspace.

Recall equation (3.6), which determined that there are

$$d_j = \frac{N!(2j+1)}{(N/2-j)!(N/2+j+1)!} \tag{3.32}$$

copies of angular momentum subspace j. Interpreting this value with statistics in mind, if one were to randomly sample an eigenstate and determine its corresponding angular momentum subspace $\hat{\mathcal{H}}_{TC}$, then the probability that its subspace has total angular momentum j is $(2j+1)d_j/2^N$. Further, if one were to randomly sample the eigenstates of the full TC Hamiltonian, at excitation level k, then the probability that this eigenstate is contained

within an angular momentum j space is $D_{j,k-k_0(j)}d_j/D_k$. Recall that D_k measures the number of states present across all angular momentum subspaces with excitation number k. Denoting the collection of all the energy levels of the Tavis-Cummings Hamiltonian as a function of k excitations as $\mathcal{E}(k)$, defined by

$$\mathcal{E}(k) = \bigcup_j \Lambda(j,k), \tag{3.33}$$

the above insights make clear the following:

$$\langle \mathcal{E}(k) \rangle = 0 \tag{3.34}$$

$$\begin{aligned} \mathrm{Var}(\mathcal{E}(k)) &= \sum_{j=\min\{N/2-k,\{N/2\}\}}^{N/2} \frac{D_{j,k-k_0(j)}d_j}{D_k} \mathrm{Var}\,\Lambda(j,k-k_0(j)) \\ &= \sum_{j=\min\{N/2-k,\{N/2\}\}}^{N/2} \frac{d_j}{D_k} \,\mathrm{tr}\, L(j,k-k_0(j))^2. \end{aligned} \tag{3.35}$$

The d_j have a combinatorial dependence on j, and it is unlikely that there is an informative closed form expression for this sum. That being said, computing this sum requires only $O(N)$ floating point operations, assuming that the factorial can be computed in $O(1)$ flops. This can be achieved by appealing to Gosper's approximation, which becomes increasingly accurate with increasing N. Numerical plots of the variance of the energy level distribution as a function of excitations can thus be readily produces for ensembles of even $N = 1000$ spins:

As one can see in figure 3.8, there are two regimes of interest elucidated with the knowledge of the variance. The first, slow growth regime is induced by the fact that as one introduces more excitations into the system, so too does one include more angular momentum subspaces. Importantly, the ground state is introduced first, which always has a magnitude 0 energy level splitting. Then, the dominant structure is the degeneracy of that next angular momentum subspace. Given a sketch of d_j it is clear that the number of degenerate copies of an angular momentum subspace are rapidly increasing as one moves from $j = N/2$ towards j_{max} which is in close proximity to the lowest angular momentum subspaces. Thus, as k increases, there is an increasingly large 0 valued contribution to the average, which persists until $k \approx j_{max}$. Hence the suppression of the magnitude of the variance of $\mathcal{E}(k)$ in this regime.

Near $N/2$ there is an inflection point where the standard deviation changes behavior to be much more regular as a function of k. The standard deviation is very closely modelled

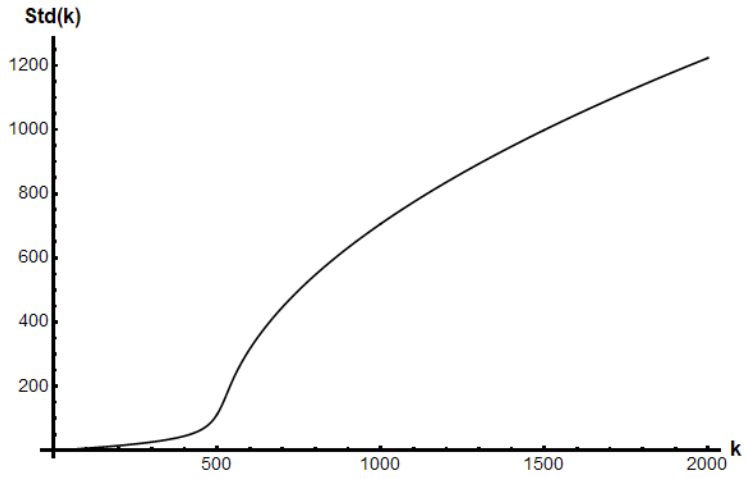

Figure 3.8: A plot of $\sqrt{\text{Var}(\mathcal{E}(k))}$, the standard deviation of the Lamb shifts as a function of excitations, for an $N = 1000$ spin TC model. Notice the change in concavity in the standard deviation at approximately $k = N/2 = 500$.

with a $\sqrt{k}$, meaning the variance is linear in k. Intuitively, around $k = N/2$, all angular momentum subspaces have a constant dimension of $2j + 1$ as k further increases, such that any impact from the spins is effectively identical with increasing k. The photonic contribution does still increase, with the action of the ladder operators bringing in a $\sqrt{k}$ dependence into the coupling matrix. Thus, the variance, being a trace of the square of this matrix, picks up a linear dependence on k. Then, one would expect that the standard deviation has a $\sqrt{k}$ dependence after $k = N/2$, which is indeed illustrated in figure 3.8.

The variance is linear in k beyond this point, as indicated by figure 3.9, and performing regression of the variance as a function of N and k reveals that the dominant growth behavior of this line is slightly less than $g_0^2 Nk$. The regression of the slope of the variance can be seen graphically in figure 3.10. In fact, one can derive the following relationship: the variance of the collective Lamb shift splittings, as function of k excitations, grows as the product of N and k for $k > N + 1$, so that

$$\text{Var}(\mathcal{E}(k)) = O(Nk). \tag{3.36}$$

The derivation of this statement hinges on understanding how degeneracies of lower angular momentum subspaces dominate the statistics. In fact, the derivation works by considering only the strong support of d_j as a function of the angular momentum space j, which encompasses only the lowest $O(\sqrt{N})$ subspaces.

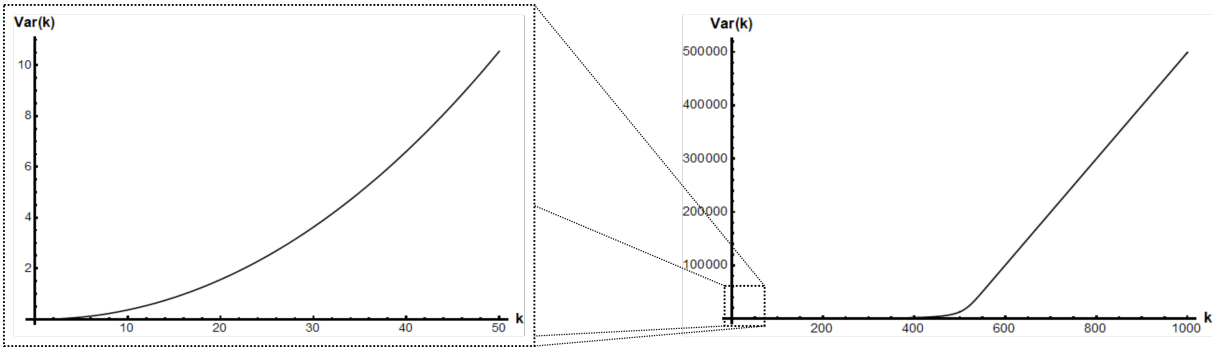

Figure 3.9: Variance of the unit–less ($\hbar = g_0 = 1$) Lamb shift splittings for $N = 1000$ spin–1/2 particles. Notice that the variance becomes linear in k soon after $k = N/2 = 500$. Notice the non-linearity and reduction of scale of the variance in the lower excitation subspaces as compared to the $k > N/2$ subspaces.

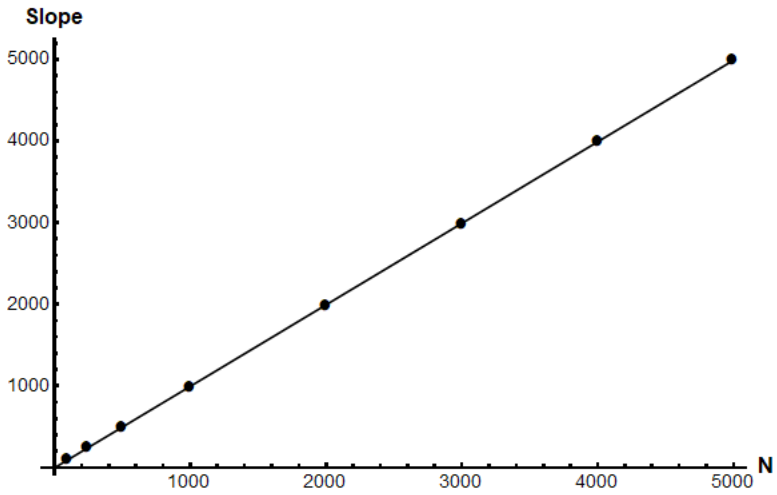

Figure 3.10: Slope of the variance of the collective Lamb shift splittings in the linear regime, for various N. Points mark computed values of the slope for each N. The regression model is $\text{Slope}(N) = 0.9989N - 0.27$, with an R^2 value of nearly 1.

Turning now to a brief investigation of the behavior of d_j as a function of j, the location of j_{max}, can be done numerically. As it stands, d_j is not a continuous function of j, but by elevating factorials to Gamma functions or utilizing the Gosper's approximation, one can sidestep this issue. Computing j_{max} and performing regression for a range of values of N produces the curve seen in figure 3.11.

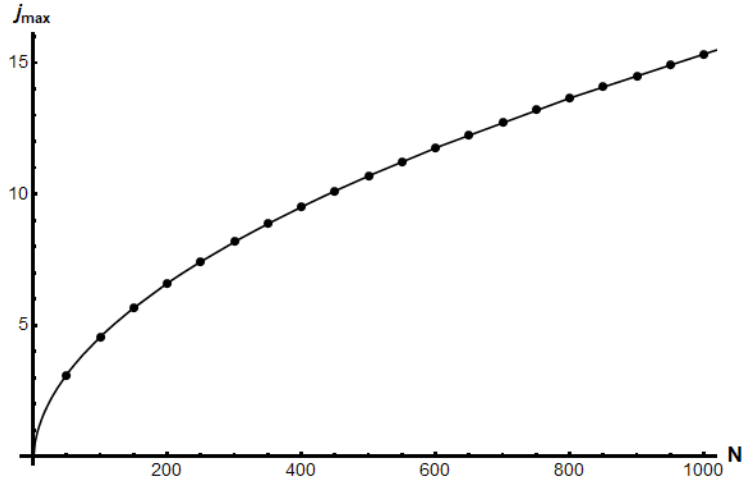

Figure 3.11: A plot of a fit for j_{max} as a function of the number of spins, N. The points indicate numerically computed values of j_{max} for select values of N such that $0 < N \leq 1000$, and the solid line is given by the regression model, $-0.268755 + 0.459957 * N^{0.51029}$.

As illustrate in figure 3.11, j_{max} follows an almost square root of N dependence, at least up to $N = 10,000$. The fit was found by first finding the power law using a log-log regression. Then, that power was utilized to transform the data such that linear regression was done to enhance the fit. This resulted in

$$j_{max}(N) \approx 0.06724 + 0.450427 * N^{0.51029}. \tag{3.37}$$

It should be noted that there is seemingly no single power law dependence that accurately describes j_{max} for all ranges of N. After a variety of transformations were attempted on the data, this one was determined to be the best fit, even though there are structured residuals, visualized in figure 3.12.

From joint research on this subject, an approximate mathematical relationship for j_{max} can be computing by appealing to digamma functions [46]. The resulting formula is extremely precise, with increasing accuracy at higher values of N:

$$j_{max}(N) = \frac{\sqrt{N}}{2} - \frac{1}{2} + \frac{1}{6\sqrt{N}} + O\big(\frac{1}{N}\big). \tag{3.38}$$

From the same work, the region of strong support is approximately determined. For visualization's sake, figure 3.13 showcases the shape of the the degeneracy distribution as a function of j, and illustrates that almost all population is contained within a small fraction of the lowest angular momentum subspaces, all localized near j_{max}.

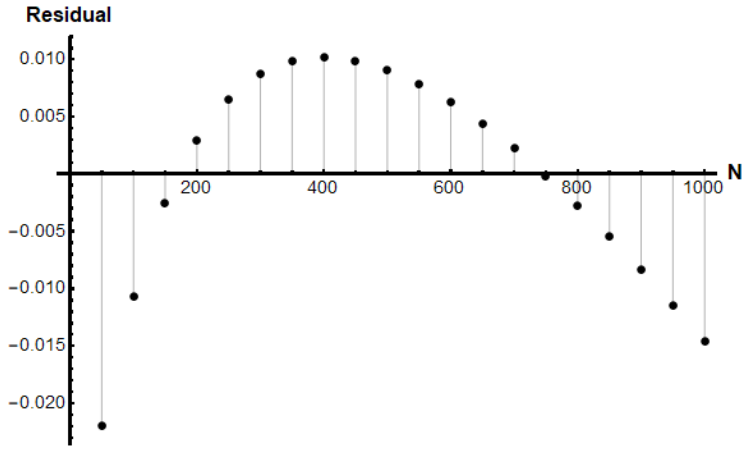

Figure 3.12: A plot of residuals of the fit for j_{max}.

Mathematically, external work has shown that the strong support of d_j is all j such that $0 \leq j \leq O(\sqrt{N})$ [46]. Then, to prove the statement about the variance, it is easiest to work with $k > N$, since this fixes $D_k = 2^N$. Then,

$$\mathrm{Var}(\mathcal{E}(k)) = \frac{1}{2^N} \sum_j d_j \,\mathrm{tr}(L(j,k)^2). \tag{3.39}$$

Recall that the trace of the square is given by,

$$\begin{aligned} \mathrm{tr}(L(j,k)^2) = &\frac{1}{2} |\mathcal{B}_{j,k}|^4 - \frac{1}{3} |\mathcal{B}_{j,k}|^3 (2k + 4j + 13) \\ &+ |\mathcal{B}_{j,k}|^2 (2jk + 4k + 8j + 23/2) \\ &- |\mathcal{B}_{j,k}| \frac{1}{3}(18jk + 44j + 22k + 53) \\ &+ 4(jk + 2j + k + 2). \end{aligned} \tag{3.40}$$

Using the fact now that $|\mathcal{B}_{j,k}| = 2j + 1$,

$$\begin{aligned} \mathrm{tr}(L(j,k)^2) = &k\big(\frac{8}{3}j^3 + 4j^2 - \frac{8}{3}j\big) \\ &- N\big(\frac{4}{3}j^3 + 2j^2 - \frac{4}{3}j\big) \\ &+ \big(\frac{4}{3}j^2 - 2j^2 - \frac{34}{3}j - 2\big). \end{aligned} \tag{3.41}$$

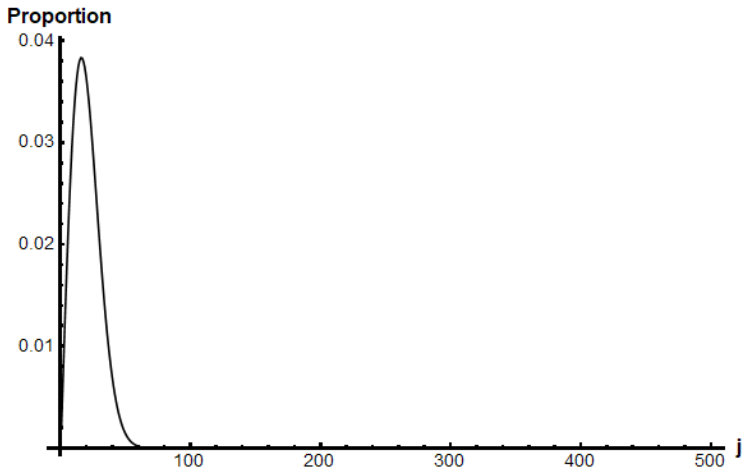

Figure 3.13: Degeneracy as a function of angular momentum, scaled by the total number of states. Here, $N = 1000$, the horizontal axis labels j, and the vertical axis represents the *degeneracy weighting function*, $d_j/2^N$.

We focusing on only the terms of order k, the dominant part of the expression is given by

$$\frac{4}{3}k(2j^3 + 3j^2 - 2j). \tag{3.42}$$

It remains to determine the order k contribution to the entire variance,

$$\mathrm{Var}(\mathcal{E}(k)) = \frac{4}{3}k \sum_j \frac{d_j}{2^N}(2j^3 + 3j^2 - 2j) + \cdots, \tag{3.43}$$

where the terms of order k^0 will be dropped moving forward.

In order to make the sum over j tractable, one can bound d_j to show that for all allowed values of j,

$$\frac{d_j}{2^N} = O(\frac{1}{N}). \tag{3.44}$$

Since $d_j < d_{j^*}$ for each j, this bound needs only to be shown for $j = j_{max}$. Then, taking only the leading term of $j_{max} = \sqrt{N}/2$,

$$d_{j_{max}} = \frac{\sqrt{N}/2 + 1}{N/2 + \sqrt{N}/2 + 1}\binom{N}{N/2 + \sqrt{N}/2 + 1}. \tag{3.45}$$

Focusing on the first factor,

$$\frac{2}{\frac{N+1}{\sqrt{N}+1} + 1} = O(1/\sqrt{N}). \tag{3.46}$$

Since $k = N/2 + \sqrt{N}/2 + 1$, $|N/2 - k| = o(n^{2/3})$, which allows for the utilization of the following asymptotic equivalence relation[44]:

$$\binom{N}{k} \sim \frac{2^N}{\sqrt{N\pi/2}} e^{-(N-2k)^2/(2N)}. \tag{3.47}$$

Then, using the fact that $N - 2k = \sqrt{N} - 2$,

$$e^{-(N-2k)^2/(2N)} = e^{-(\sqrt{N}-2)^2/(2N)} = e^{-1/2+2/\sqrt{N}-2/N} = \frac{1}{\sqrt{e}}\big(1 + O(1/\sqrt{N})\big). \tag{3.48}$$

Putting this together with the asymptotic equivalence relation,

$$\binom{N}{N/2 + \sqrt{N}/2 + 1} \sim \frac{2^N}{\sqrt{N\pi e/2}}\big(1 + O(1/\sqrt{N})\big) = O(2^N/\sqrt{N}). \tag{3.49}$$

This finally implies

$$d_{j_{max}} = O(2^N/N), \tag{3.50}$$

and thus it hold that for all allowed j,

$$d_j 2^{-N} = O(1/N). \tag{3.51}$$

Utilizing all of these facts about d_j, and that the strong support of the weighting function is from 0 to $O(\sqrt{N})$, the sum can be computed explicitly under these approximations as

$$\begin{aligned}
\sum_j \frac{4k d_j}{2^N} \frac{2j^3 + 3j^2 - 2j}{3} &= \frac{4k}{3} \sum_j O\big(\frac{1}{N}\big)(2j^3 + 3j^2 - 2j) \\
&\approx O\big(\frac{k}{N}\big) \sum_{j=0}^{O(\sqrt{N})} (2j^3 + 3j^2 - 2j) \\
&= O\big(\frac{k}{N}\big) O(N^2) \\
&= O(Nk).
\end{aligned} \tag{3.52}$$

Then, the root mean square energy level splitting of the Tavis-Cummings model grows as $g_0 O(\sqrt{Nk})$, which parallels the energy level splittings of the Jaynes-Cummings model, which grows as exactly $g_0\sqrt{k}$. The non-linear energy level splittings of the JC model

have been used to verify that superconducting qubits are interacting with a resonator in a quantum manner [10]. The same non-linearity is then present in the TC model at high ($k > N$) excitation values, now with an additional collective enhancement factor of $\sqrt{N}$. It is then reasonable to believe that this same experimental design can be used to verify that a collection of qubits is interacting with quantized EM field under a *collective quantum interaction*.

3.2 Thermal Behavior of the TC Hamiltonian

To connect the results presented so far and make predictions about physical reality, one needs to consider thermal states and experimentally accessible measurements. The descriptive statistics on $\mathcal{E}(k)$ provide information on the support of the accessible energy levels and their magnification due to degeneracies. All things being equal, if the support of $\mathcal{E}(k)$ is small compared to the dominant energy scale of the problem, then the thermal skew due to the Gibbs factor $e^{-\beta E}$ is effectively constant across the entire excitation space for most values of $\beta = \frac{1}{k_B T}$. This is indeed valid under the previously made assumption that $g_0 \ll \omega_0$. Thus the support of $\mathcal{E}(k)$ is determined by diagonalizations of $L(j,k)$, and the shape of the distribution over this support is more strongly dependent on degeneracy counting than temperature effects.

The visualization of $\mathcal{E}(k)$ can be made through a plot of the density of states. The density of states is defined as a function energy, with value given by the number of states present at a given energy. The state weighting function is computed as a sum of degeneracies of eigenstates within accessible angular momentum subspaces at a given energy:

$$w_k(\lambda) = \sum_j \begin{cases} d_j & \lambda \in \Lambda(j,k) \\ 0 & \text{else} \end{cases}. \tag{3.53}$$

Then, the density of states is a sum over delta-function weighted by w_k, such that

$$n(E) = \sum_{k=0}^{\infty} \sum_{\lambda \in \mathcal{E}(k)} w_k(\lambda) \delta(E - \hbar(k\omega_0 + \lambda g_0)). \tag{3.54}$$

With a log variable transformation on $n(E)$ for the sake of visualization, the density of states can be directly plotted to illustrate the energy level structure of the TC system across excitation spaces, and demonstrate the breakdown of the rotating wave approximation in certain parameter regimes. The density of states for the case where the rotating wave approximation is valid is given in figure 3.14, and in figure 3.15 for the case where the RWA breaks down.

The density of states provides direct access to the partition function, as the partition function can be acquired by taking the Laplace transform of the density of states:

$$Z(\beta) = \int_0^{\infty} \mathrm{d}E e^{-\beta E} n(E). \tag{3.55}$$

This definition is equivalent to the Hamiltonian focused definition to be given in equation (3.57), but arguably provides a better intuition for how the shape of the degeneracy

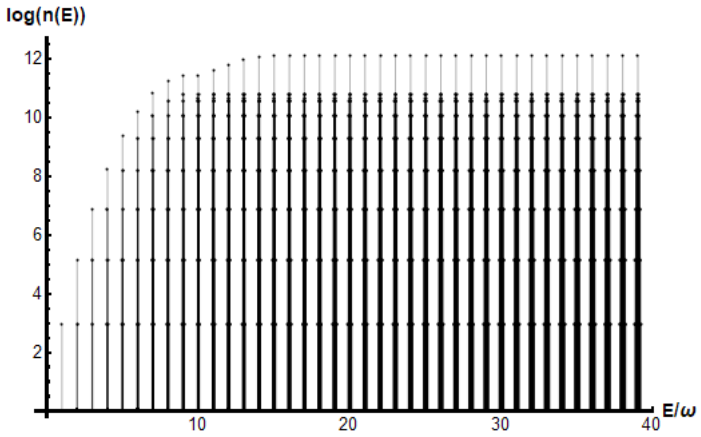

Figure 3.14: Scaled density of states for $N = 20$ spins, with $\omega/g = 500$. The rotating wave approximation is valid for the entire range of k values shown in this plot. The increasing thickness of the lines at each excitation subspace illustrates both the growth of the variance of the Lamb shift as a function of excitations and that *eventually*, at high enough energies, the RWA will become invalid.

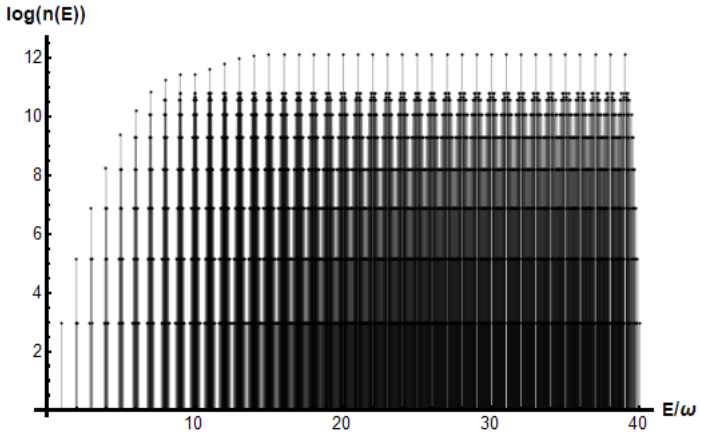

Figure 3.15: Scaled density of states for $N = 20$ spins, with $\omega/g = 100$. The RWA begins to break down at around $k = 15$ excitations, and overlapping subspaces indicated that the notion of "excitation number" is not a good quantum number, violating the underlying assumptions. Thus, the TC model should not be used for high energy experiments or systems with ultra–strong coupling.

weighting function dominates the structure thermal states at all but the lowest excitation

levels.

The computation of a full thermal distribution is straightforward at this point. Plot $\mathcal{E}(k)$ about k on the x-axis, scaling the axis by g_0/ω_0, up to some k_{max}. This produces an un-normalized plot of an infinite temperature distribution. To include finite temperature, simply multiply by the curve $e^{-\beta E}$, where E is the energy scaled appropriately, and finally normalize the entire curve to area 1 (equivalently, divide by the partition function).

To illustrate this behavior, consider an ensemble of $N = 100$ spins. Thanks to the subspace decomposition, computing all eigenvalues for every subspace up to $k = 200$ excitations can be done in a matter of minutes on a laptop. From there, it is only a few more seconds of computation time to combine all of that data into a thermal distribution for a given temperature. As a first attempt at visualization, consider a reasonable experimental situation where the spin-cavity system sits in a dilution refrigerator at $T = 0.1$ Kelvin. Take $\omega_0 = 10$ GHz, and $g_0 = 10$ Hz.

It seems almost surprising that even at such a low temperature, with relatively small ensemble of spins, that the average energy is so far from the ground state energy. Thanks to the efficiency of all the necessary computations, one can easily plot the average thermal energy as a function of temperature to see how far one has to cool in order to get a distribution near the ground state.

Figure 3.17 illustrates that there is a region where the expected energy of the thermal ensemble varies much more rapidly than on the rest of the domain. Based on everything learned thus far, this behavior can be attributed to degeneracies of angular momentum subspaces. The partition function, and the Gibbs thermal state for this Hamiltonian, given by

$$\hat{\rho}_T = \frac{e^{-\beta \hat{\mathcal{H}}_{TC}}}{\operatorname{tr} e^{-\beta \hat{\mathcal{H}}_{TC}}}, \tag{3.56}$$

can be easily calculated numerically, as indicated by the calculation of the previous plots. This is mainly due to the fact that the only important quantities that need to be extracted from the coupling matrices are the eigenvalues. If the eigenvectors corresponding to the computed energy level splittings were required, it would be much more computationally difficult.

The partition function for a Hamiltonian with energetically degenerate, but all discrete, quantum states is given as a function of inverse temperature, $\beta = \frac{1}{k_B T}$, such that

$$Z(\beta) = \operatorname{tr} e^{-\beta \hat{\mathcal{H}}} = \sum_E D(E) e^{-\beta E}. \tag{3.57}$$

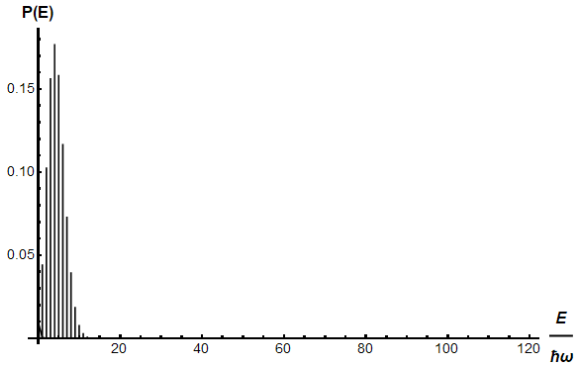

(a) $T = 0.025$ K

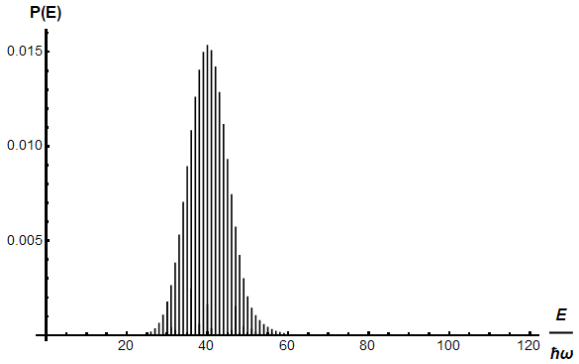

(b) $T = 0.200$ K

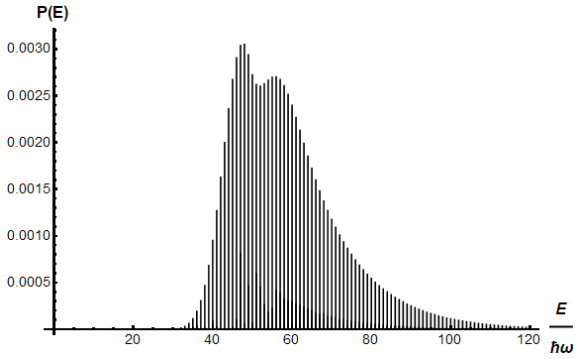

(c) $T = 1.00$ K

Figure 3.16: Thermal population distribution for the TC Hamiltonian at $\omega_0 = 10$ GHz, $g = 10$ Hz, and $N = 100$ spins, for selected temperatures of $T = 0.025, 0.200, 1.000$ Kelvin. Notice that at each temperature, the ground state population is not appreciably populated for temperatures on the order of hundreds of mK or greater.

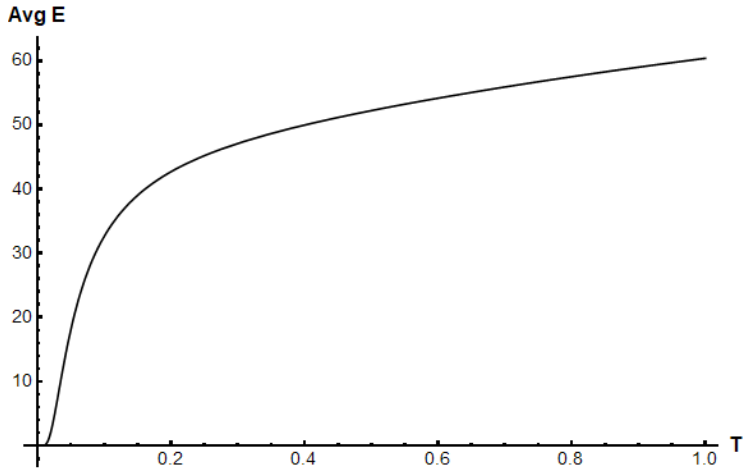

Figure 3.17: Plot of the average thermal energy for an $N = 100$ spin TC model as a function of T in Kelvin.

In equation (3.57), one sums over all energy eigenvalues of $\hat{\mathcal{H}}$, denoted by E, with degeneracy given as $D(E)$. This can be broken down into a triple sum, over the two good quantum numbers (k and j) and then finally the energy level splittings within a (j,k) subspace. Then,

$$Z(\beta) = \sum_{k=0}^{\infty} \sum_{j=N/2}^{\max\{N/2-k,\{N/2\}\}} d_j \Bigg(\sum_{\lambda \in \Lambda(j,k-k_0(j))} \exp\big(-\hbar\beta(k\omega_0 + \lambda g_0)\big) \Bigg). \tag{3.58}$$

The form of the partition function in equation (3.58) fully illustrates how the block decomposition can aid both in computations and for intuition. As a note, the sum over j in equation (3.58) is meant to be taken as counting down – this could easily be transformed into a proper summation, but at the cost of clarity within the argument of the exponential.

In order for any summation representing the partition function to be well defined, it must converge. By inspection, notice that while the contributions from the degeneracies of angular momentum spaces is quite large, the contribution is bounded and achieves a maximum contribution when $k = \lfloor \frac{N}{2} \rfloor$. Similar behaviour occurs due to the sum over λ. The infinite sum over k is then eventually dominated by a decaying exponential, which converges so long as the temperature is positive. The Tavis-Cummings Hamiltonian is infinite dimensional and thus does not permit negative temperatures. For the sake of argument, a negative temperature could be introduced on the spin system before it is coupled to the cavity, and then rapidly introduced, which would be modeled by upgrading

g_0 to a switching function at some critical time t_0. Even in this case, the resulting state would not be a thermal state of the new Hamiltonian, and after some thermalization time, the resulting temperature would still be positive with a finite partition function.

Even though convergence is guaranteed for the partition function as a whole, there is still a clear competition for dominance at the lower excitation levels between d_j and $\exp(-k\beta\hbar\omega_0)$. Consider for a moment the portion of the partition function formed by only summing over the ground states, as those terms provide the necessary intuition without much distraction:

$$e^0 + (N-1)e^{-\beta\hbar\omega_0} + \frac{N(N-3)}{2}e^{-2\beta\hbar\omega_0} + \frac{N(N-1)(N-5)}{6}e^{-3\beta\hbar\omega_0} + \cdots . \tag{3.59}$$

It is not uncommon in an electron spin resonance (ESR) experiment to consider and ensemble of between 10^9 and 10^{15} spins coupled collectively and resonantly to a single mode EM field in a cold dilution refrigerator [41]. Consider $N = 10^{12}$ with the usual $\omega_0 = 10$GHz. It appears that while one is considering angular momentum subspaces far above j_{max}, then decreasing j leads to increasing powers in N in the expression for the degeneracy. Since numerics leads one to expect $j_{max} \approx O(\sqrt{N})$, the region of strong support for the angular momentum degeneracy distribution occurs about $10^{12} - 10^6 \approx 10^{12}$ angular momentum subspaces away from the true ground state. Thus one would expect this behaviour to remain true for a long while. Within these low excitation angular momentum ground states, the dominant term, as a function of k, is then

$$\big(N\exp(-\beta\hbar\omega_0)\big)^k. \tag{3.60}$$

For large spin ensembles, the low excitation sector of the partition function can be viewed approximately as a sum over truncated geometric series. The geometric series with the largest rate factors are then the ground states of each angular momentum subspace with an approximate rate factor of $r = N\exp(-\beta\hbar\omega_0)$, and one would expect then that their behavior dominates over the other truncated series. It is well known that for geometric series, convergence is guaranteed if $|r| < 1$. So then, how does this behavior translate into the partition function? The only tunable parameter in the model is currently taken to be the temperature, and so temperature is the determining factor for the "convergence behavior" of the truncated geometric series. Translating $r < 1$ into experimental parameters, one finds

$$N\exp\big(-\frac{\hbar\omega_0}{k_BT}\big) < 1 \implies T < \frac{\hbar\omega_0}{k_B\log N}. \tag{3.61}$$

The critical temperature for the example parameters given comes out to $T_c = 0.00276437$ degrees Kelvin. Then, one can compute the behavior of the full partition function for the

first 4 excitation levels across all angular momentum subspaces. That is, a sum over all energy levels drawn in figure 3.7. To help visualize how the partition function behaves as a function of temperature, consider a plot of partial sums of the partition function, given in figure 3.18. The kth partial sum of the partition function is written $Z_k(\beta)$, and defined in equation (3.62).

$$Z_k(\beta) = \sum_{k'=0}^{k} \sum_{j=N/2}^{\max\{N/2-k',\{N/2\}\}} d_j \left(\sum_{\lambda \in \Lambda(j,k'-k_0(j))} \exp\big(-\beta\hbar(k'\omega_0 + \lambda g_0)\big) \right). \tag{3.62}$$

Since the ground state is set adjusted to an eigenenergy of $E = 0$, the population of the ground state is simply given as $1/Z(\beta)$. This puts the ground state population in the cold regime at $T = 0.002 < T_c$ at 0.999974. At the critical temperature, the ground state population is approximately 0.35, and in the hot regime, $T = 0.0035 > T_c$, the ground state population is at least less than 10^{-6}. There is clearly an extreme sensitivity to temperature in the lowest regime, with a fast transition from the ground state being very well populated below T_c, and being hardly populated above T_c. Surprisingly, the simplistic geometric series argument produced a very accurate rule for computing where this cut lies, given the back of the envelope nature of its computation. Mathematically, the drastic change in low excitation behavior is precisely determined by the competing scaling of degeneracy terms and Gibbs thermal factors in the partition function. For this reason, thermal states with temperature below T_c shall be called *temperature dominated*, while thermal state with temperature above T_c shall be called *degeneracy dominated*.

So where does the population go in the degeneracy dominated regime? By appealing to smaller ensembles of spins, this question becomes much easier to answer. The average energy as a function of temperature, plotted in figure 3.17 gives the approximate location of population by first indicating which excitation level is dominant. Since the ground states of each angular momentum space are populate faster due to equivalent orders of contribution from the Gibbs factors and degeneracy factors, one would expect that most of the thermal population occurs in the ground states near the location of the average energy, with some population in nearby excited states as well. In particular, the $N = 100$ plot of figure 3.17 shows a very rapid rise in average energy to just above $E = 40\hbar\omega$. Given that $j_{max}(100) = 5$, it is unsurprising that after average energy reaches approximately $45\hbar\omega$ the slope as a function of temperature becomes drastically reduced. It would be at this point that any scaling effects due to newly introduced degenerate angular momentum subspaces begin to saturated, and thermal scaling begins to take back control. That being said, the presence of the degeneracies has irreversibly pushed up the average thermal energy at a given temperature.

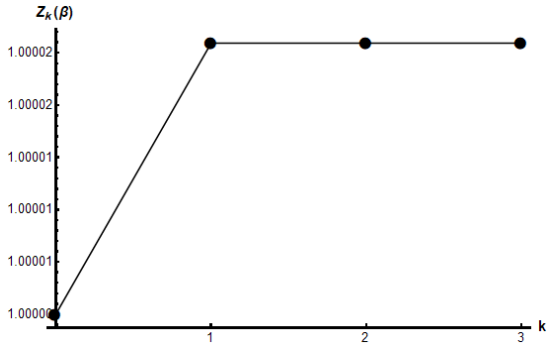

(a) $T = 0.002$ K

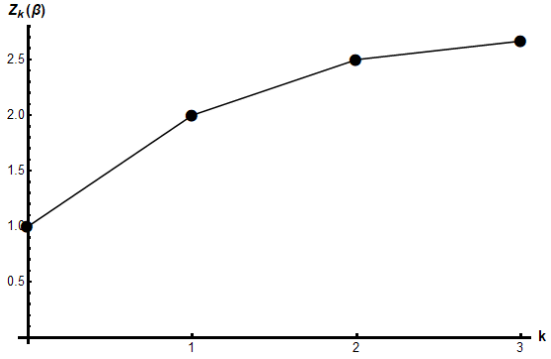

(b) $T = 0.002764$ K

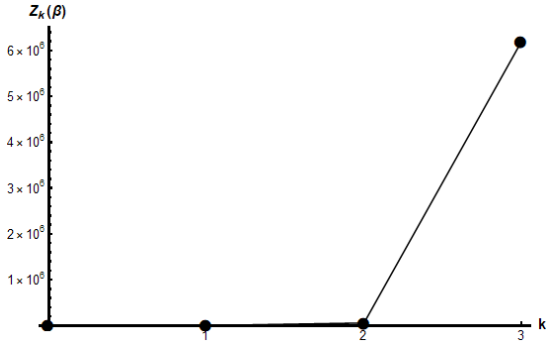

(c) $T = 0.0035$ K

Figure 3.18: Plots of $Z_k(\beta)$ with temperature below, at, and above, the critical temperature for an TC model particularized to $N = 10^{12}$ spins. Notice the vastly different scales and concavities for each temperature. In particular, the $T = .0035$ sample does not appreciably populate the ground state.

To illustrate the transition between the temperature and degeneracy dominated regime, consider zooming in on the average energy as a function of temperature for $N = 100$ spins, focusing on temperatures nearby to the critical temperature for this ensemble, $T_c = 0.01658$ K. This behavior is illustrated in figure 3.19

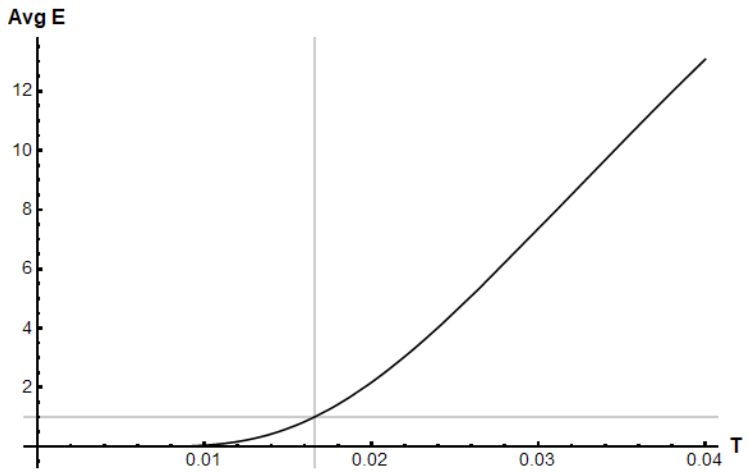

Figure 3.19: Plot of the average thermal energy for an $N = 100$ spin TC model as a function of T (in Kelvin) in the ultra–cold temperature regime. Marked on this plot are the constant lines $T_c = 0.01658$ and $\langle E \rangle = \hbar\omega_0$, which nearly intersect on the curve describing the average thermal energy for this ensemble.

As seen in figure 3.19, the critical temperature almost exactly corresponds to $\langle E \rangle = \hbar\omega_0$ for $N = 100$. In actuality, $\langle E \rangle_{T=0.01658} \approx 1.003\hbar\omega_0$, the coincidence is indeed striking, albeit a likely artifact of the particular parameter set. One would indeed expect that within the temperature dominated regime, average energy be near or less than $\hbar\omega_0$, since the population is almost entirely contained within the true ground state, which has an energy eigenvalue of 0. The drastic increase in average energy as temperature rises into the degeneracy dominated regime corresponds directly to the drastic decrease in population of the lowest lying excitation spaces.

To investigate the sharpness of the transition as a function of N, consider a plot of the expected energy as function of temperature, with the identical values for ω_0 and g_0, while also varying N. First, consider the average thermal energy in the degeneracy dominated regime.

Now, consider a plot of the same behaviour, while restricting to even lower temperatures, in order to focus on the temperature dominated regime.

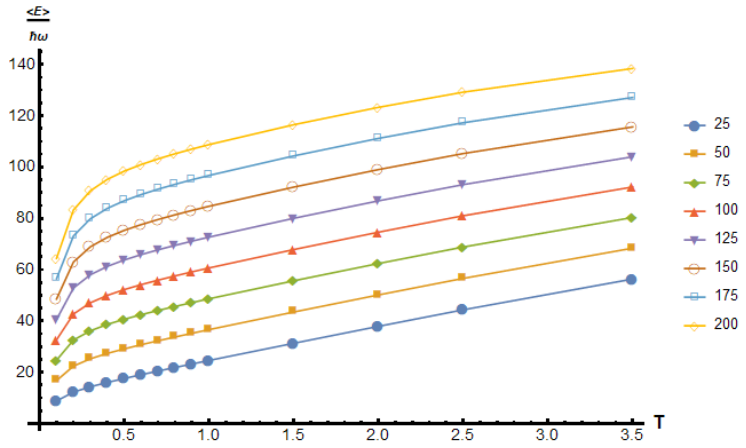

Figure 3.20: Plot of the average thermal energy for varying N, as labelled by the legend, as a function of T. In the degeneracy dominated regime, the expected energy is concave down in T, and monotonically increasing in N.

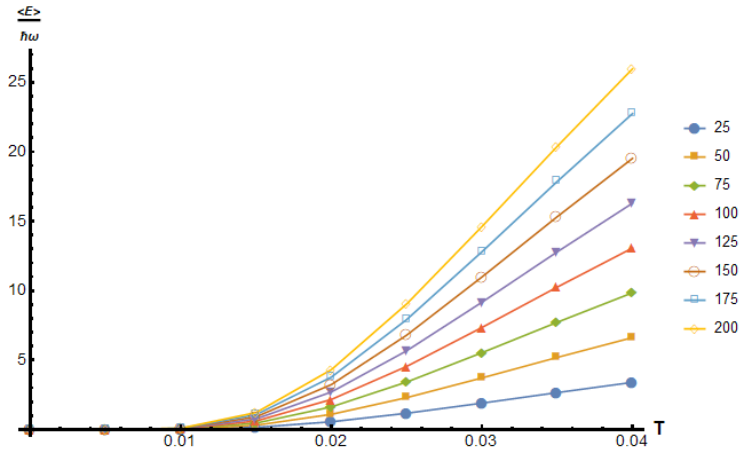

Figure 3.21: Plot of the average thermal energy for various sized spin ensembles, given by N, as a function of the temperature T. In the temperature dominated regime, the expected energy is concave up in T, and monotonically increasing in N.

A full description of the behavior of this function is not possible to do exactly in a closed form. This is due to the fact that the expected energy can be written as a derivative of the natural logarithm of the partition function, which itself admits no closed form solution

for the Tavis-Cummings Model.

$$\begin{aligned}\frac{\partial Z(\beta)}{\partial \beta} &= \sum_E -E e^{-\beta E} \\ &= -Z(\beta)\left(\frac{1}{Z(\beta)}\sum_E E e^{-\beta E}\right) \\ &= -Z(\beta)\,\langle E\rangle \qquad (3.63)\\ \implies \langle E\rangle &= -\frac{1}{Z(\beta)}\frac{\partial Z(\beta)}{\partial \beta} \\ \implies \langle E\rangle &= -\frac{\partial \log Z(\beta)}{\partial \beta} \qquad (3.64)\end{aligned}$$

Thus, while an exact closed form equation describing this behavior is seemingly out of reach, useful trends and information can still be extracted.

Firstly, at a given temperature, the difference in expected energy as a function of N appears quite regular, and is in fact linear. To see this, consider a plot of the average energy as a function of N, given a fixed temperature T.

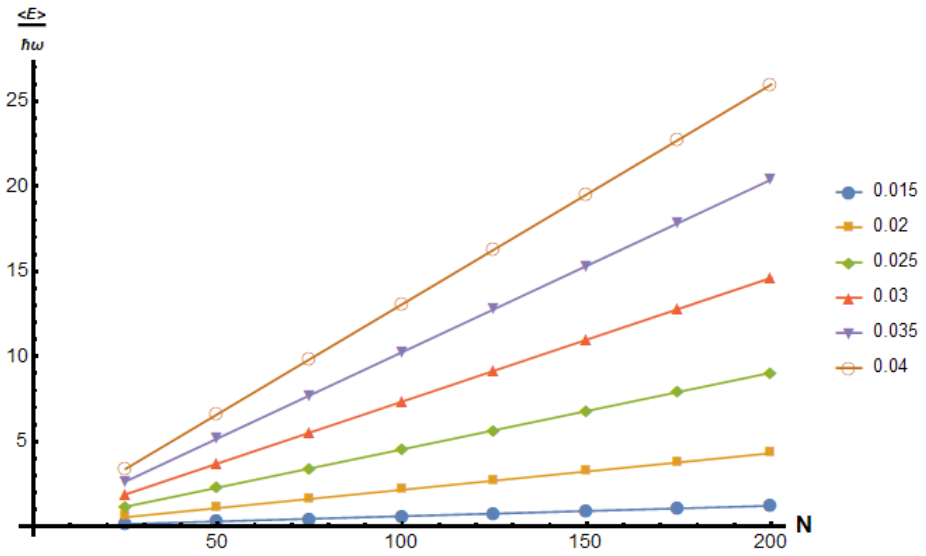

Figure 3.22: Plot of the average thermal energy of the TC model for select temperatures as a function of the number of the spins, N. Notice that at each temperature, $\langle E\rangle$ is a linear function of N.

Regression confirms what the eye suspects in figure 3.22, each constant temperature slice is a linear function in N. This indicates that the average energy as a function of N and T in this regime can be written as a linear function in N, with slope and intercept depending solely on T, at least for the values considered numerically.

$$\langle E \rangle (N, T) = m(T)N + b(T) \tag{3.65}$$

Now, fitting $m(T)$ and $b(T)$ proves to be much more challenging, as these functions inherit the complicated behavior of the partition function. After a bit of investigation, and many failed fits, it became clear that $m(T)$ was a much more complicated function than $b(T)$. In fact, it was discovered by repeated variable transformation that $b(T)$ could be fit to a two parameter model:

$$b(T) = xT \exp\big(-\frac{y}{T}\big), \quad x, y \in \mathbb{R}_+. \tag{3.66}$$

A large confounding issue with the regression for $m(T)$ was that the function seemed to involve a $0 \times \infty$ type limit as $T \longrightarrow 0$. The limits always converged to 0 for any attempted model, but proved to be difficult for the numerical regression algorithms to handle. A variety of variable transformations were done in an attempt to improve stability, and eventually a 3 parameter model was reached that yielded good fitting behaviour:

$$\log m(T) = x + y \log T + \frac{z}{T^{1.1}}, \quad x, y, z \in \mathbb{R} \tag{3.67}$$

Putting everything together, the resulting fit to the data produced the following final approximate function for $\langle E \rangle$.

$$\langle E \rangle (N, T) \approx \exp\left(\frac{.0435}{T^{1.1}} - 0.688\right) T^{-0.02276} + T \exp\left(2.57011 - \frac{0.03675}{T}\right) \tag{3.68}$$

The main issue with the fit is that small residuals in the function $m(T)$ are magnified by when they are multiplied by large N. This causes the deviation seen in the plots of figures 3.23 and 3.24, which show the predicted values of $\langle E \rangle$ from the regressed model along with the actual computed values.

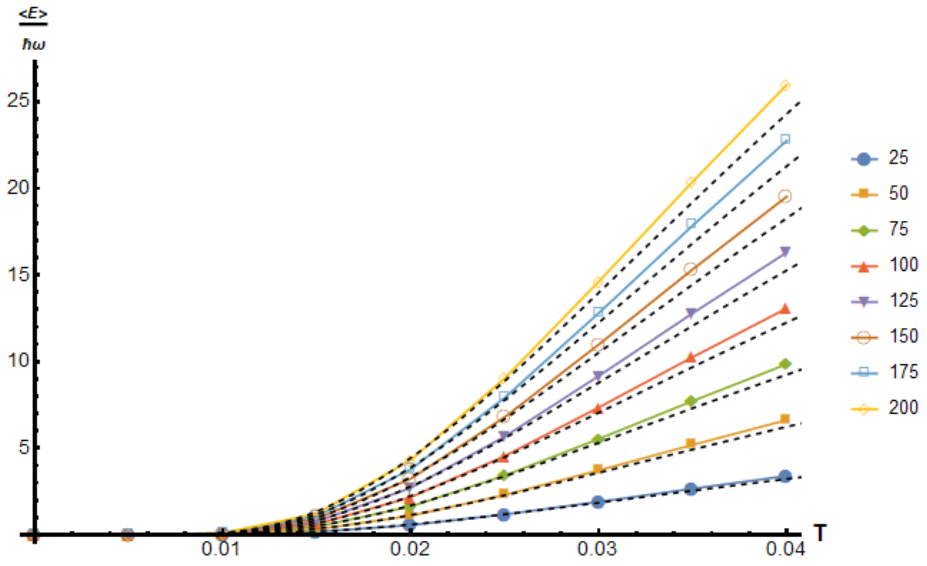

Figure 3.23: Shown are plots of average energy of the TC model as a function of temperature for various values of N, in the temperature dominated regime. Computed values at a given value of N are labeled by the legend, and their corresponding predicted values from the regression model are indicated by the dashed lines.

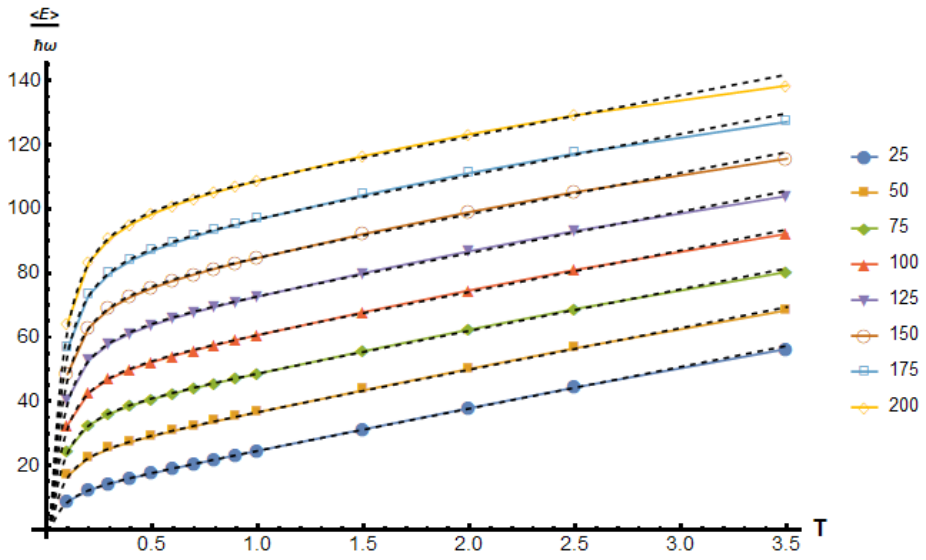

Figure 3.24: Shown are plots of average energy of the TC model as a function of temperature for various values of N, in the degeneracy dominated regime. Computed values at a given value of N are labeled by the legend, and their corresponding predicted values from the regression model are indicated by the dashed lines.

3.3 Dynamics of Initially Thermal States

The sensitivity of the thermal state to temperature, and the surprisingly low critical temperature for ensuring a state has a significant population in the low excitation eigenstates, has profound impacts on experimental design and interpretation. The common practice in literature is often to assume that population is only contained in the $j = N/2$ subspace, and that the dominant experimental signature seen in these experiments is determined by transitions between the $k = 0$ and $k = 1$ excitation subspaces within this angular momentum space [41, 3, 23, 28]. For an ensemble of N spins, the $k = 1$ energies of these eigenstates are split by $\pm\hbar g_0\sqrt{N}$, which can easily rise into the MHz regime. This has led to the confusing notion of single spin g, given by $g = g_0$, usually on the order of tens of Hertz, and collective spin g, given as $g = g_0\sqrt{N}$, which occasionally even replaces g_0 in the statement of the Tavis-Cummings Hamiltonian [41, 3, 23, 28]. As already shown in this work, the energy eigenstructure, and its relation to thermal states, has a much more rich and complex structure than these assumptions seem to imply.

At present, experimentally accessible information for a quantum system described by a Tavis-Cummings Hamiltonian are given as expectation values of observables. In particular, one can measure on the spins through a magnetic interaction, or on the cavity through homodyne detection of a field quadrature [20]. Measurement on the spins would physically require a set of conducting coils be introduced around the spins, which can pick up a free induction decay (FID) signal, effectively measuring $\left\langle \hat{J}_x \right\rangle$. The presence of these coils is dual purposed, as one can also send current through them, inducing a magnetic field, which provides some measure of collective control on the spins. The cavity observable is taken to be the x field quadrature, represented by $\frac{1}{2}\left\langle \hat{a} + \hat{a}^\dagger \right\rangle$. By appealing to the circuit description of QED, this is realized through current or voltage measurements across the quantum resonator. As with the spins, the observable operator can be similarly utilized as a control on the EM field by sending current or voltage into the resonator.

The detection of the precession of spins has been long studied through the field of NMR, and the pulse sequences of NMR for enhanced sensitivity translate directly to the measurement of a Tavis-Cummings type system. The theoretical description of an experiment is then seemingly straightforward: define an initial state, a pulse sequence, and then an observable. The pulse sequence corresponds to a series of unitary actions on the initial state, and then computation of the observable is simply the expected value of that updated state evolving in time. Further, time evolution of an energy eigenstate is simple:

$$\hat{\mathcal{H}} \left|\psi(0)\right\rangle = E \left|\psi(0)\right\rangle \implies \left|\psi(t)\right\rangle = e^{\frac{\mathrm{i}Et}{\hbar}} \left|\psi(0)\right\rangle . \tag{3.69}$$

By linearity, this extends to any superposition of energy eigenstates. As of yet, the actual components of the eigenstates in the spin-cavity basis, $\mathcal{B}_{j,k}$, have not been needed for any computations. Unfortunately, in order to compute the action of $\hat{J}_x$ or $\hat{a}^\dagger$, one needs either the representation of these operators in the energy eigenbasis, or the components of the energy eigenbasis in the spin-cavity basis. In either case, a full orthogonal diagonalization of $L(j,k)$ is now required, and there is a major loss of computational efficiency since the $O(n \log n)$ eigenvalue algorithm is no longer sufficient.

It is clear that there are two paths to experimental prediction that do not overload computational scaling: small spin ensembles and restrictions to low excitation subspaces. The restriction to low excitation subspaces embodies the current practice for descriptions of large spin Tavis-Cummings models. As discussed, this requires one to be in the temperature dominated regime of the thermal distribution. The representations of the actions of $\hat{J}_x$ and the photon ladder operators can be computed with relative ease when restricting to the lowest excitation subspaces. For small numbers of spins, even a full Hamiltonian description of is feasible, and can provide insight into high spin low excitation simulations, without having to be computationally clever.

Consider a Tavis-Cummings Hamiltonian with $N = 3$ spin-1/2 particles. There are two angular momentum subspaces, $j = 3/2$ with degeneracy 1 and $j = 1/2$ with degeneracy 2. The energy splitting eigenvalues can be easily computed. Starting with the $j = 1/2$ subspace, which has a ground state with $k = 1$ excitation. For $k \geq 2$,

$$\Lambda(1/2, k) = \{-\hbar g_0 \sqrt{k-1}, \hbar g_0 \sqrt{k-1}\}. \tag{3.70}$$

The respective eigenvectors to the above eigenvalues are given by

$$\frac{1}{\sqrt{2}}\big(|1/2, -1/2\rangle |k-1\rangle - |1/2, 1/2\rangle |k-2\rangle \big)$$
$$\frac{1}{\sqrt{2}}\big(|1/2, -1/2\rangle |k-1\rangle + |1/2, 1/2\rangle |k-2\rangle \big).$$

The $j = 3/2$ ground state is the true ground state of the Hamiltonian, with $k = 0$ excitations. At $k = 1$, the energy splitting eigenvalues are given by

$$\Lambda(3/2, 1) = \{-\sqrt{3}\hbar g_0, \sqrt{3}\hbar g_0\}, \tag{3.71}$$

with corresponding eigenvectors of

$$\frac{1}{\sqrt{2}}\big(|3/2, -3/2\rangle |1\rangle - |3/2, -1/2\rangle |0\rangle \big)$$
$$\frac{1}{\sqrt{2}}\big(|3/2, -3/2\rangle |1\rangle + |3/2, -1/2\rangle |0\rangle \big).$$

Moving on to $k = 2$,

$$\Lambda(3/2, 2) = \{-\sqrt{10}\hbar g_0, 0, \sqrt{10}\hbar g_0\}, \tag{3.72}$$

with corresponding eigenvectors,

$$\begin{aligned}
&\frac{1}{\sqrt{10}}\big(\sqrt{3}\,|3/2,-3/2\rangle\,|2\rangle - \sqrt{5}\,|3/2,-1/2\rangle\,|1\rangle + \sqrt{2}\,|3/2,1/2\rangle\,|0\rangle\,\big)\\
&\quad\frac{1}{\sqrt{5}}\big(\sqrt{2}\,|3/2,-3/2\rangle\,|2\rangle \qquad\qquad - \sqrt{3}\,|3/2,1/2\rangle\,|0\rangle\,\big)\\
&\frac{1}{\sqrt{10}}\big(\sqrt{3}\,|3/2,-3/2\rangle\,|2\rangle + \sqrt{5}\,|3/2,-1/2\rangle\,|1\rangle + \sqrt{2}\,|3/2,1/2\rangle\,|0\rangle\,\big).
\end{aligned}$$

For $k \geq 3$, the energy eigenvalues can indeed be written in closed form,

$$\begin{aligned}
\Lambda(3/2, k) = \Big\{ &-\hbar g_0\sqrt{5k - 5 + \sqrt{16k^2 - 32k + 16}}, -\hbar g_0\sqrt{5k - 5 - \sqrt{16k^2 - 32k + 16}},\\
&\hbar g_0\sqrt{5k - 5 - \sqrt{16k^2 - 32k + 16}}, \hbar g_0\sqrt{5k - 5 + \sqrt{16k^2 - 32k + 16}}\Big\}.
\end{aligned} \tag{3.73}$$

The energy eigenvectors as a general function of k become very unwieldy, their closed form solution is omitted here, but can be found in [46]. With the structure of the Hamiltonian determined, interpreting the outcome of experimentally motivated simulations is possible. The $N = 3$ hybridized energy level ladder, additionally marked with $\hat{J}_+$ meditated transitions, is given in figure 3.25.

Consider a simple experimental procedure of "pulse and measure". The unitary sequence is then simply a θ rotation about the x axis, and then an acquisition of the free induction decay, allowing the system to evolve under the Hamiltonian. This sequence can be mathematically described by a single unitary operator, such that

$$\hat{U}(t) = \exp\left(\frac{-\mathrm{i}\hat{\mathcal{H}}t}{\hbar}\right)\exp\Big(-\mathrm{i}\theta\hat{J}_x\Big). \tag{3.74}$$

The FID signal can be then computed as

$$\Big\langle \hat{J}_x(t)\Big\rangle = \mathrm{tr}\left(\hat{U}(t)\hat{\rho}_{in}\hat{U}(t)^\dagger\hat{J}_x\right), \tag{3.75}$$

for some initial state $\hat{\rho}_{in}$. Computing the action of the transverse pulse can, in principle be done by appealing to the modified Euler formula for $\mathfrak{su}(2)$ to $SU(2)$ correspondence:

$$\exp\big(-\mathrm{i}\frac{\theta}{2}\boldsymbol{n}\cdot\hat{\boldsymbol{\sigma}}\big) = \mathbb{1}\cos\frac{\theta}{2} - \mathrm{i}\boldsymbol{n}\cdot\hat{\boldsymbol{\sigma}}\sin\frac{\theta}{2}. \tag{3.76}$$

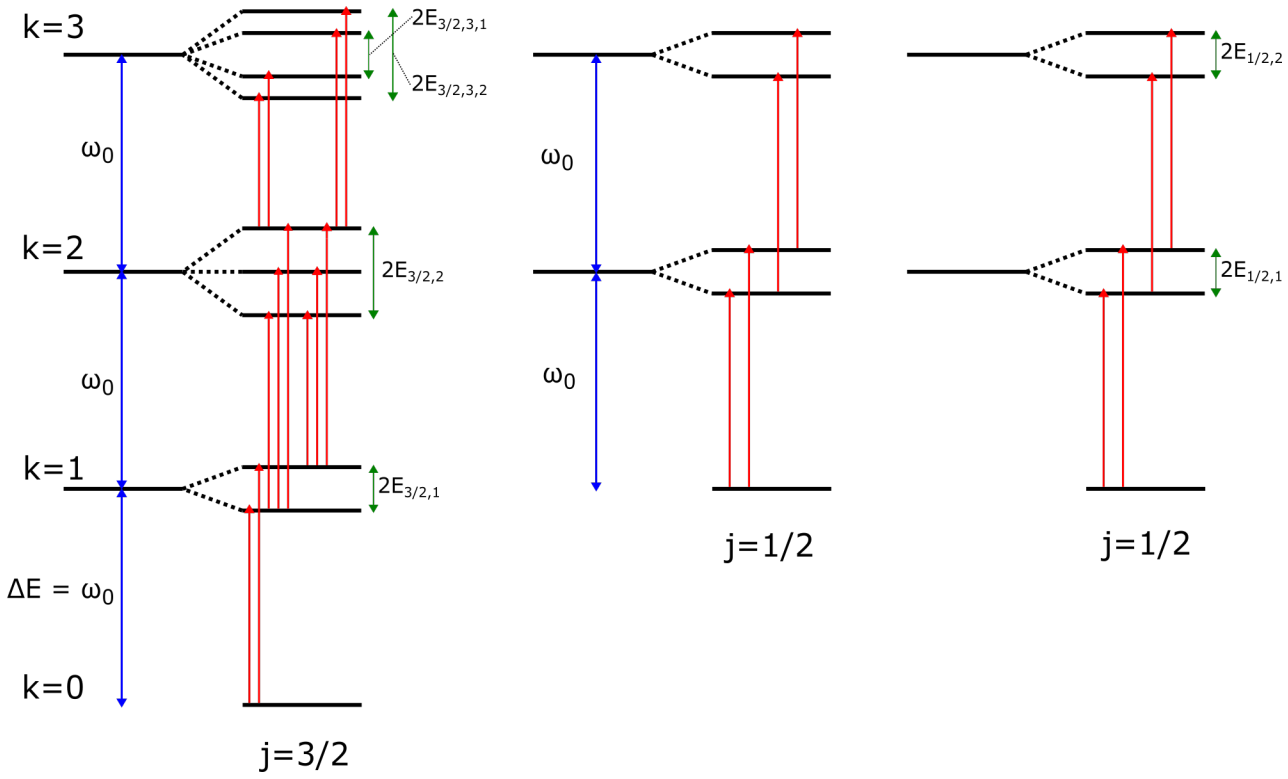

Figure 3.25: Illustration of the resulting hybridization of energy levels in the Tavis–Cummings model for $N = 3$, explicitly on resonance such that $\omega_0 = \omega_s = \omega_c$. Vertical single arrow lines (red) indicate transitions mediated by $\hat{J}_+$, meaning that the eigenstates represented by the horizontal bars have a non-zero $\hat{J}_+$ matrix element. Transitions are all–to–all between neighboring excitation subspaces of the same angular momentum, with some transitions between the $k = 2$ and $k = 3$ subspaces omitted for clarity. Note that there are no allowed transitions via collective spin or photon operators between distinct angular momentum subspaces, regardless of the value of j. Separation between excitation spaces is a constant ω_0, denoted by bidirectional arrows (blue) between the pre–hybridized angular momentum states. Lamb shift splittings are denoted be bidirectional arrows (green) to the right of the hybridized states. In the $j = 1/2$ subspaces, these splittings are given by $E_{1/2,k} = g_0\sqrt{k}$. In the $j = 3/2$ subspace, the Lamb shifts are given by: $E_{3/2,1} = g_0\sqrt{3} \approx 1.73g_0$, $E_{3/2,2} = g_0\sqrt{10} \approx 3.16g_0$, $E_{3/2,3,1} = g_0\sqrt{10 - \sqrt{73}} \approx 1.21g_0$, and $E_{3/2,3,2} = g_0\sqrt{10 + \sqrt{73}} \approx 4.31g_0$.

Above, $\boldsymbol{n}$ is a three dimensional real unit vector, and $\hat{\boldsymbol{\sigma}}$ is a symbolic vector with Pauli operator components, such that

$$\boldsymbol{n} \cdot \hat{\boldsymbol{\sigma}} = n_x \hat{\sigma}_x + n_y \hat{\sigma}_y + n_z \hat{\sigma}_z. \tag{3.77}$$

Thus,

$$\hat{U}_R(\theta) = \exp\Big(- \mathrm{i}\theta \hat{J}_x \Big) = \prod_{i=1}^{N} \Big(\mathbb{1} \cos\frac{\theta}{2} - \mathrm{i}\hat{\sigma}_x^{(i)} \sin\frac{\theta}{2} \Big), \tag{3.78}$$

which in principle can be written as an order N polynomial in $\hat{J}_x$, but it is computationally tedious to use in practice.

It was shown in [11] how to expand and simplify a general element of $SU(2)$ in terms of the generating element, $\boldsymbol{n} \cdot \hat{\boldsymbol{J}}$, for a given total angular momentum representation labelled by j. Given a 3 dimensional real unit vector $\boldsymbol{n}$, and $\theta \in \mathbb{R}$, for a spin-j representation of $\hat{\boldsymbol{J}}$,

$$\hat{U}_R(\theta) = \exp\big(\mathrm{i}\theta \boldsymbol{n} \cdot \hat{\boldsymbol{J}}\big) = \sum_{p=0}^{2j} \frac{c_p^j(\theta)}{p!} \big(2\mathrm{i}\sin(\theta/2)\boldsymbol{n} \cdot \hat{\boldsymbol{J}}\big)^p. \tag{3.79}$$

The coefficients, $c_p^j(\theta)$, are defined such that for $x = \sin^2(\theta/2)$, $\epsilon = 0.5(1 - (-1)^{2j-p})$,

$$c_p^j(\theta) = \Big(\cos\frac{\theta}{2} \Big)^{\epsilon} \operatorname*{Trunc}_{\lfloor j - p/2 \rfloor} \Big(\frac{\arcsin^p \sqrt{x}}{(\sqrt{x})^p (\sqrt{1-x})^{\epsilon}} \Big). \tag{3.80}$$

The operator Trunc truncates an ordered series, which should be understood in this context as operating on the Taylor series expansion of the argument. To illustrate the behavior of the operator, consider the truncation of a general power series which converges on some interval about $z = 0$:

$$\operatorname*{Trunc}_{n} \Big(\sum_{k=0}^{\infty} a_k z^k \Big) := \sum_{k=0}^{n} a_k z^k. \tag{3.81}$$

If desired, the formulae for fully expanding out the coefficients of equation (3.79) can be utilized to fully define the action of a $\hat{J}_x$ pulse and subsequent expectation values. A full treatment in this manner is far too computationally complex for ensembles with large N. The full time evolution treatment is given for $N = 3$ below.

One can numerically compute the expected value for $\hat{J}_x$ as a function of time for a small N Tavis-Cummings model by solving the Schrodinger equation. For larger N samples, this approach is extremely inefficient. The experimental observable of interest is the spectrum formed by taking the Fourier transform of the resultant time series for $\Big\langle \hat{J}_x(t) \Big\rangle$. Before

diving into the numerics, it is instructive to first simply consider the qualitative actions of the desired operators. For now, take $N = 3$, with an initial state in the ground state of the Hamiltonian.

Firstly, assuming that all population starts in the ground state translates to an initial state entirely within the $j = 3/2$ angular momentum subspace. Since the collective symmetry isn't broken in this scenario, all populations must remain in this subspace. The θ rotation about x can be written as a polynomial in $\hat{J}_x$, and will thus be able to excite coherences in the $k = 0, 1, 2, 3$ excitation subspaces. Because the resultant state is a coherent superposition, each term in the superposition picks up a time dependent complex phase with frequency equal to the state's energy. A detection through $\hat{J}_x$, which couples neighbouring angular excitation spaces, will yield a signal at the difference of energies of any two populated states which are separated by a single excitation. For example, transitions between the $k = 0$ and $k = 1$ subspaces mediated by $\hat{J}_x$ should produce a non-zero signal of frequencies $\omega \pm g_0\sqrt{N}$. If θ is small, one might expect that rotation unitary will only induce coherences of an appreciable magnitude on excitation space over. That is, for small θ, the polynomial for $\hat{U}_R$ is well approximated by the first order terms. This assumption will be rigorously derived later in the section for general N. Denote the ground state as

$$|g\rangle = |3/2, -3/2\rangle\,|0\rangle\,, \tag{3.82}$$

and the $k = 1$ states as

$$|\omega_0 \pm g_0\sqrt{N}\rangle = \frac{1}{\sqrt{2}}\,|3/2, -3/2\rangle\,|1\rangle \pm \frac{1}{\sqrt{2}}\,|3/2, -1/2\rangle\,|0\rangle\,. \tag{3.83}$$

Under the small θ assumption, the action of the rotation unitary is then

$$\hat{U}_R(\theta)\,|g\rangle = \alpha_0\,|g\rangle + \alpha_-\,|\omega_0 - g_0\sqrt{N}\rangle + \alpha_+\,|\omega_0 + g_0\sqrt{N}\rangle\,. \tag{3.84}$$

The coefficients are a function of θ and can be determined through the matrix elements,

$$\begin{aligned}
\alpha_0 &= \left\langle g \right| \hat{U}_R(\theta) \left| g \right\rangle \\
\alpha_- &= \left\langle \omega_0 - g_0\sqrt{N} \right| \hat{U}_R(\theta) \left| g \right\rangle \\
\alpha_+ &= \left\langle \omega_0 + g_0\sqrt{N} \right| \hat{U}_R(\theta) \left| g \right\rangle .
\end{aligned}$$

Further effort into computing these coefficients will be done later in this section in a more general setting. Now, determining the time evolution of this state is trivial since the

superposition is already expressed within the energy eigenbasis:

$$|\psi(t)\rangle = \exp\big(-\mathrm{i}t\hat{\mathcal{H}}/\hbar\big)\hat{U}_R(\theta)\,|g\rangle = \alpha_0\,|g\rangle + \alpha_- e^{-\mathrm{i}(\omega_0 - g_0\sqrt{N})t}\,|\omega_0 - g_0\sqrt{N}\rangle + \alpha_+ e^{-\mathrm{i}(\omega_0 + g_0\sqrt{N})t}\,|\omega_0 + g_0\sqrt{N}\rangle\,.$$

It only remains to compute the expected value of $\hat{J}_x$ as a function of time, which is given as

$$\begin{aligned}
\langle J_x(t)\rangle &= \left\langle \psi(t)\right|\hat{J}_x\left|\psi(t)\right\rangle \\
&= \alpha_0^*\alpha_+ e^{-\mathrm{i}(\omega_0+g_0\sqrt{N})t}\left\langle g\right|\hat{J}_x\left|\omega_0+g_0\sqrt{N}\right\rangle \\
&\quad + \alpha_0^*\alpha_- e^{-\mathrm{i}(\omega_0-g_0\sqrt{N})t}\left\langle g\right|\hat{J}_x\left|\omega_0-g_0\sqrt{N}\right\rangle + h.c. \\
&= 2\Re\Bigg(\left\langle g\right|\hat{U}_R(-\theta)\left|g\right\rangle\Bigg(e^{-\mathrm{i}(\omega_0+g_0\sqrt{N})t}\left|\left\langle g\right|\hat{J}_x\left|\omega_0+g_0\sqrt{N}\right\rangle\right|^2 \\
&\quad + e^{-\mathrm{i}(\omega_0-g_0\sqrt{N})t}\left|\left\langle g\right|\hat{J}_x\left|\omega_0-g_0\sqrt{N}\right\rangle\right|^2\Bigg)\Bigg).
\end{aligned} \tag{3.85}$$

The exact magnitudes given as matrix elements could be computed here, but the precise expressions are not very enlightening. The main result of this derivation is to illustrate that there are two sinusoidal components of $\left\langle \hat{J}_x(t)\right\rangle$, with frequencies $\omega = \omega_0 \pm g_0\sqrt{N}$. In the Fourier transform of the FID signal, one should see peaks about these frequencies and nowhere else. It is expected that they will be of similar magnitude.

Now, by convention the ground state has been taken to be a state of 0 energy, and so it takes a trivial complex phase as its time evolution. If the initial state was an eigenstate with energy splitting eigenvalue λ_i and k excitations, then any excited coherence with a state of $k+1$ excitations and energy splitting eigenvalue of λ_f would induce a sinusoidal signal of frequency $\omega = \omega_0 + (\lambda_f - \lambda_i)$. In case of the ground state, $k = 0$, $\lambda_i = 0$, and $\lambda_f = \pm g_0\sqrt{N}$.

To confirm and visualize this prediction, consider a full numerical simulation of this phenomenon. Consider the particular parameter set of $\omega_0 = 10$, $g_0 = 0.2/\sqrt{3}$, and $\hbar = 1$. These experimentally unrealistic parameters ensure that full numerical simulation of a measured signal does contain incommensurate time scales, and lends to easier visualization of the resulting spectrum. Finally, take $\theta = 0.1$. Computing the time evolution of the initial state with these parameters and taking the Fourier transform of the measured signal results in figure 3.26

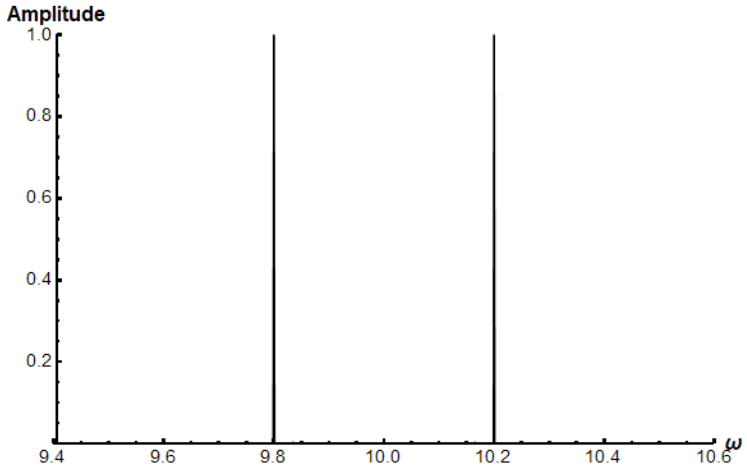

Figure 3.26: Fourier transform of the Free Induction Decay signal measured through $\left\langle \hat{J}_x(t) \right\rangle$ for the TC model initially in the ground state, with $N = 3$ spins, under a J_x pulse of $\theta = 0.1$. The signal is scaled so that the maximum is equal to 1. Notice the peaks are precisely located at $\omega_0 \pm g_0\sqrt{N} = 10 \pm 0.2$, as predicted.

Figure 3.26 is not all that surprising, it is the usual prediction made for the spectra of the Tavis-Cummings system, often made without consideration of the temperature of the sample or the angle of rotation. It is the goal of this section to show that two peaks shifted from ω_0 by $\pm g_0\sqrt{N}$, as shown in figure 3.26 almost never the correct description.

Small spin examples have lower computation difficulty, and so consider relaxing the small angle assumption. The expectation is that with a larger flip angle, additional coherences will be excited within the $k = 2$ and $k = 3$ subspaces, leading to more peaks than just the $\pm g_0\sqrt{N}$ peaks. In principle, these coherences exist in the small angle case, but are negligible in magnitude. Importantly, the additional coherences will introduce new peaks in the Fourier transform of the measured signal, located at the energy differences between the $k = 1$ and 2 subspaces, as well as the between the $k = 2$ and 3 subspaces. Given that the $N = 3$ Tavis-Cummings model has been solved earlier in this section, one can refer to the sets of eigenvalues given in equations (3.72) and (3.73) to predict the locations of the newly induced peaks. The spectrum for the case of $\theta = \pi/4$ is shown in figure 3.27. Additionally, the spectrum for $\theta = \pi/2$ is shown in figure 3.28.

While the spectrum is still dominated by the $g_0\sqrt{N}$ splittings, one should note that for $N = 3$, there are 4 spin states within the Dicke subspace, and 4 outside of it. As N increases, the proportion of states contained in the Dicke subspace falls drastically. For

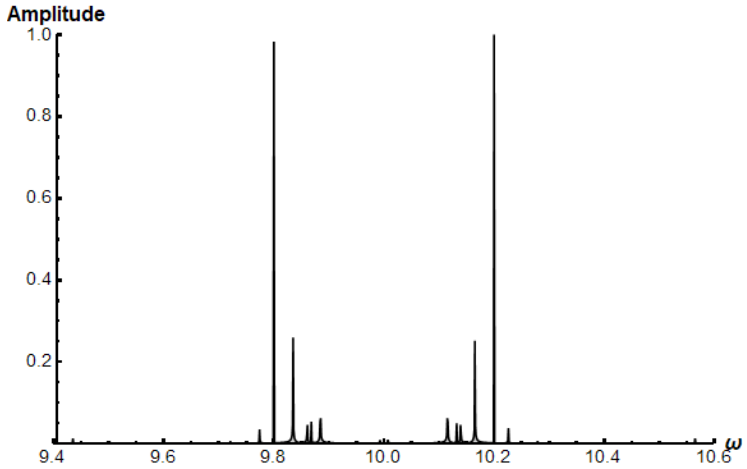

Figure 3.27: Fourier transform of the Free Induction Decay signal measured through $\left\langle \hat{J}_x(t) \right\rangle$ for the TC model initially in the ground state, with $N = 3$ spins, under a J_x pulse of $\theta = \pi/4$. Notice that peaks are located at $\omega_0 \pm g_0\sqrt{N}$, but that these two peaks are no longer the sole structure of the spectrum.

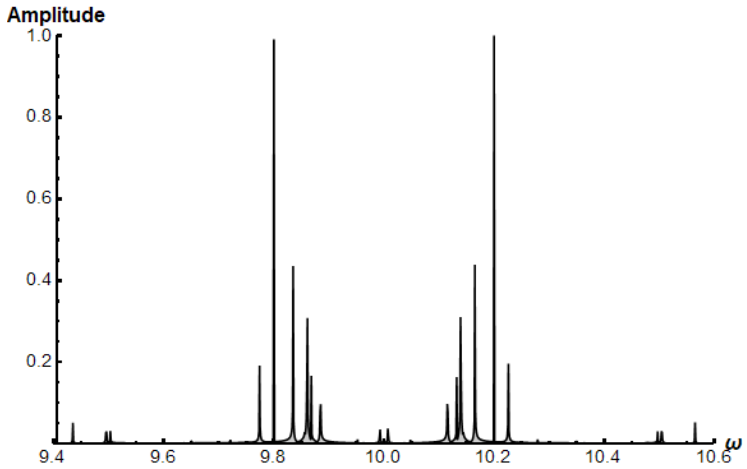

Figure 3.28: Fourier transform of the Free Induction Decay signal measured through $\left\langle \hat{J}_x(t) \right\rangle$, under a J_x pulse of $\theta = \pi/2$. Notice that peaks are located at $\omega_0 \pm g_0\sqrt{N}$, but that these two peaks are no longer the sole structure of the spectrum.

$N = 5$, there are 6 spin states within the Dicke subspace, and thus there are 26 states outside of it. In order for these considerations to be appreciable within the structure of

the spectrum, the initial states will now taken to be thermal states.

For the sake of simulation efficiency and visualization, take the following parameter set of $N = 5$, $\omega_0 = 10$, $g_0 = .2/\sqrt{5}$, and $\hbar = k_B = 1$. Thermal states of this ensemble are then written as

$$\hat{\rho}_T = \frac{1}{Z(\beta)} e^{-\beta \hat{\mathcal{H}}}, \tag{3.86}$$

where $Z(\beta)$ is the partition function given as $Z(\beta) = \mathrm{tr}\exp(-\beta\hat{\mathcal{H}})$, and $\beta = 1/T$. Due to the experimentally unusual parameter set, the values of T in the current temperature scale are not all that enlightening, and so the temperature of these states will be indexed by their purity,

$$\mathcal{P}(\hat{\rho}) = \mathrm{tr}(\hat{\rho}^2). \tag{3.87}$$

By no means is the purity one-to-one with temperature, but the utility here is that the purity gives a sense of how clustered the population is. A purity near 1 indicates that most of the population is contained within a single pure state. Based on previous investigations into the thermal trends of the TC model, a high purity sample is one where most of the population is contained in the ground state of the system. As the temperature increases, the state leaves the temperature dominated regime and enters the degeneracy dominated regime, with a correspondingly increasing spread of population about higher energy states. These states will have low values of purity.

Consider a small flip angle, $\theta = 0.1$. Then, a low temperature, high purity state should reproduce the spectral shape of figure 3.26, where the initial state was the ground state of the Hamiltonian. Figure 3.29 shows the spectrum for a thermal state with a purity of 0.999, that is, almost all of the initial population is contained in the ground state of the $N = 5$ TC Hamiltonian. The image confirms that a very low temperature thermal state behaves as expected, producing the two peak shifted above and below ω_0 by $g_0\sqrt{N}$. As usual, the magnitude is normalized so that the maximum signal is equal to 1.

Now, increasing the flip angle to larger values for θ reproduces similar trends as compared to figures 3.27 and 3.28, and will be thus omitted. Focusing instead on varying the temperature of the intitial state (and thus its purity), consider the same procedure of inducing a small angle rotation and measuring the FID signal, but now with increasingly larger values for temperature. As noted, the increase in temperature yields a corresponding decrease in purity. For reference, the spectra of figures 3.29 to 3.32 are all normalized to the amplitude of the signal for the 0.999 purity case given in figure 3.29. Notice both the decrease in signal amplitude relative to the coldest sample with increasing temperature, as well as the change in shape and narrowing of the peak modes.

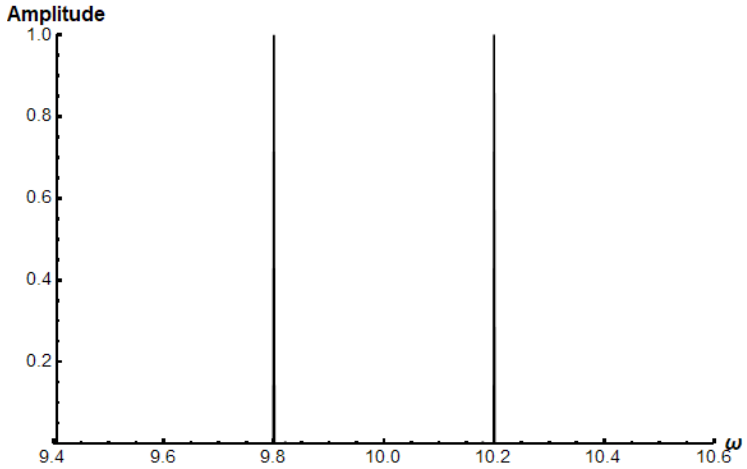

Figure 3.29: Fourier transform of the Free Induction Decay signal measured through $\left\langle \hat{J}_x(t) \right\rangle$ of an initially thermal state of the TC Hamiltonian with $N = 5$ spins. The purity of the thermal state is 0.999. The state is initially perturbed by a J_x pulse with $\theta = 0.1$.

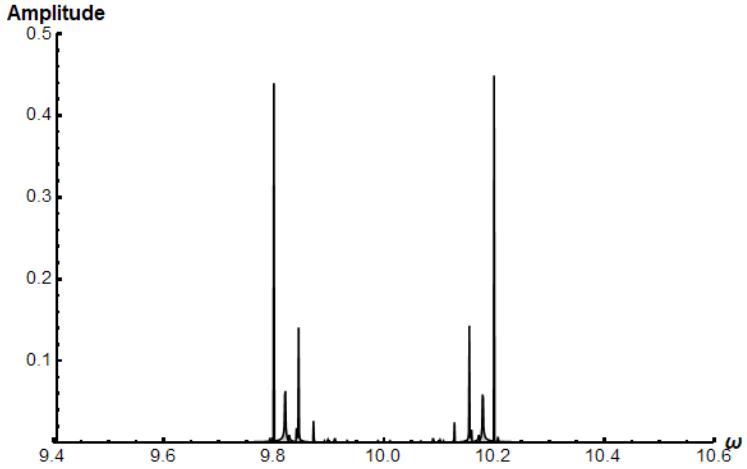

Figure 3.30: Fourier transform of the Free Induction Decay signal measured through $\left\langle \hat{J}_x(t) \right\rangle$ of an initially thermal state of the TC Hamiltonian with $N = 5$ spins. The purity of the thermal state is 0.234. The state is initially perturbed by a J_x pulse with $\theta = 0.1$.

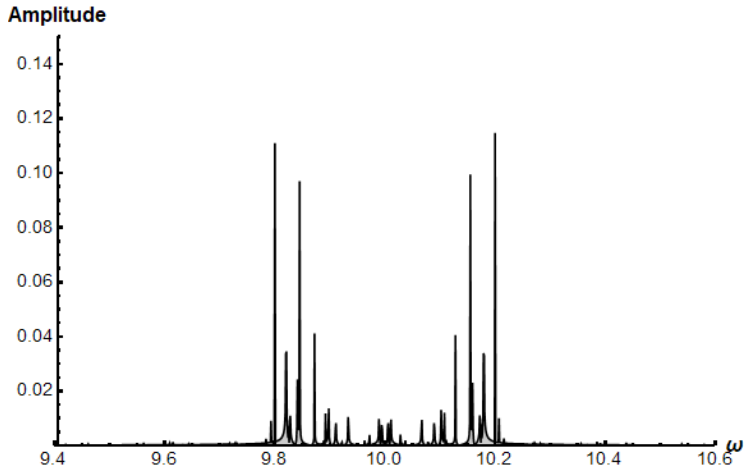

Figure 3.31: Fourier transform of the Free Induction Decay signal measured through $\left\langle \hat{J}_x(t) \right\rangle$ of an initially thermal state of the TC Hamiltonian with $N = 5$ spins. The purity of the thermal state is 0.039. The state is initially perturbed by a J_x pulse with $\theta = 0.1$.

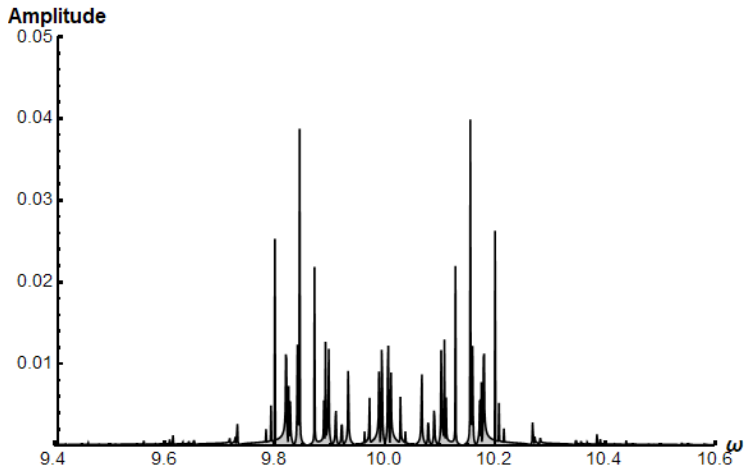

Figure 3.32: Fourier transform of the Free Induction Decay signal measured through $\left\langle \hat{J}_x(t) \right\rangle$ of an initially thermal state of the TC Hamiltonian with $N = 5$ spins. The purity of the thermal state is 0.013. The state is initially perturbed by a J_x pulse with $\theta = 0.1$.

In principle, one can calculate the locations of more peaks expected in these simulations without much difficulty since the spectrum for $N = 3$ is fully solved above, and $N = 5$ can be solved exactly as well. In order to compute the magnitudes of the peaks at a given predicted location in frequency space, one has to compute the state after the Ramsey pulse, and all of the relevant matrix elements. This process is significantly more computationally challenging when it comes to scaling N, as the eigenvector problem does not receive the speed up to $O(n \log n)$ floating point operations, which was present in the algorithm for the eigenvalue problem. Further, the structure here is non-negligible since there is a possibility that a matrix element could be 0; there is no *a priori* reason why a matrix element shouldn't be 0. In practice though, this seems to be a very rare occurrence. In point of fact, the only 0 matrix element discovered thus far is in the $j = 1$ angular momentum space, where the two unshifted (coupling matrix eigenvalue 0) states of neighboring excitation subspaces have a 0 matrix element.

Figures 3.27 and 3.28 well illustrate that even if all population is initially contained in the Dicke subspace, a single peak splitting is an insufficient description of the dynamics. It is all too common in literature to see a Dicke approximation, resulting in two peaks split by $g_0\sqrt{N}$ [41, 3, 29]. When factoring in the results of the numerical investigation into thermal states, which showed that a Dicke ground state assumption is only valid when temperatures are less than 10 mK, one should be very careful of the approximations and restrictions made when attempting to predict the spectrum of a spin ensemble coupled to a cavity.

To fully illustrate the deviation a full theoretical computation has with the Dicke approximation in common experimental regimes, consider $N = 100$ spins. While this quantity is still small compared to most spin samples, it is likely large enough to illustrate typical behavior while still being computationally tractable. Returning to the experimental parameter set of $\omega_0 = 10GHz$, $g_0 = 10Hz$, with temperature $T = 0.120$ K. The thermal state of this quantum system is in the rising portion of the degeneracy dominated regime, with an average energy of approximately $40\hbar\omega_0$.

The goal for an ensemble of this size is to predict the spectrum without tracking an exponentially scaling amount of eigenvector data. That being said, representations of $\hat{J}_x$ are dense in the energy eigenbasis, and so eigenvectors will still need to be computed. That being said, under a small flip-angle approximation, the computational cost can be reduced to a point where spectra are efficiently calculable.

Consider a thermal state undergoing purely Unitary evolution. Under this assumption, one needs only to determine the contribution for a general state, and then average the result over all possible state. For ease of visualization, initial state can be generally represented as an density matrix in the following simplistic notation:

$$\hat{\rho} = \frac{1}{Z(\beta)} \sum_E e^{-\beta E} d(E) \left|E\right\rangle\!\left\langle E\right| = \sum_E P(E) \left|E\right\rangle\!\left\langle E\right| . \tag{3.88}$$

In order to control and measure the spin system, a weakly coupled set of induction coils are introduced into the system, which can be modeled as a toggle-able perturbation Hamiltonian of the form $\hat{V} = \Omega \cos \omega t \hat{J}_x$. Under the assumption that pulses happen quickly, and that back-action from measurement is negligible to the energy eigenstructure, this Hamiltonian provides access to control through collective x rotations, and measurement through a magnetic free induction decay (FID) of the spin ensemble. Mathematically, the unitary is written

$$\hat{U}_R(\theta) = \exp\big(- \mathrm{i}\theta \hat{J}_x \big). \tag{3.89}$$

The observable is simply

$$A \left\langle \hat{J}_x \right\rangle , \tag{3.90}$$

where A is a real amplitude depending on the spin-coil coupling and any signal amplifications. For convenience, take $A = 1$.

Making use of the expansion in equation (3.79), one can expand the relevant rotation unitary in terms of angular momentum dependent representations of $\hat{J}_x$ and its powers, so that

$$\begin{aligned} \exp\big(- \mathrm{i}\theta \hat{J}_x \big) &= \bigoplus_j \left(\sum_{p=0}^{2j} \frac{c_p^j(\theta)}{p!} \big(- 2\mathrm{i} \sin(\theta/2) \hat{J}_x \big)^p \right) \\ &= \bigoplus_j \Big(c_0^j(\theta) \mathbb{1} - 2\mathrm{i} c_1^j(\theta) \sin(\theta/2) \hat{J}_x + \cdots \Big). \end{aligned} \tag{3.91}$$

It is instructive to determine how each operator in the sum impacts the good quantum numbers of j and k. Total angular momentum is unchanged, since all operators are collective, so $\Delta j = 0$. On the other hand, $\hat{J}_x = 0.5(\hat{J}_+ + \hat{J}_-)$, and so $\hat{J}_x$ raises and lowers the number of excitations present in an energy eigenstate by 1. That is, $\hat{J}_x$ mediated transitions with $\Delta k = \pm 1$. In a similar vain, $\hat{J}_x^2$ mediates transitions with $\Delta k = 0, \pm 2$, $\hat{J}_x^3$ mediates transitions with $\Delta k = \pm 1, \pm 3$, and so on.

Based on the $N = 3$ spin example, it is expected that the experimentally relevant portion of the $\hat{J}_x$ spectrum will occur about $+\omega$, and these transitions are exactly those with $\Delta k = \pm 1$. Preparing for a future small angle approximation, one can neglect the contribution of powers of $\hat{J}_x^2$ and higher, as the order two term does not mediate the desired transition, and the order 3 term comes with a pre-factor of $c_3^j(\theta)\sin^3(\theta/2)$, which will end up being absorbed in the error term of the small angle approximation. Then, the relevant action of the rotation unitary on a particular energy eigenstate can be written as follows:

$$\hat{U}_R(\theta)\left|E\right\rangle = \alpha_0\left|E\right\rangle + \sum_q \alpha_q^+\left|E_q^+\right\rangle + \sum_r \alpha_r^-\left|E_r^-\right\rangle + \cdots . \tag{3.92}$$

The $+$ and $-$ superscript notation of equation (3.92) indicate a sum over energy eigenstates with the excitation subspace either one excitation above $(+)$ or one excitation below $(-)$ the excitation subspace of the initial state $\left|E\right\rangle$.

By orthonormality of the energy eigenstates, these coefficients can be written as a matrix elements multiplied by trigonometric terms, such that

$$\alpha_0 = c_0^j(\theta) \tag{3.93}$$

$$\alpha_q^\pm = -2\mathrm{i}\sin(\theta/2)c_1^j(\theta)\left\langle E_q^\pm\right|\hat{J}_x\left|E\right\rangle . \tag{3.94}$$

With the coherence amplitudes determined, time evolution of this state must too be determined for predicting the outcome of a FID measurement. In this case, the utility of working in the energy eigenbasis is precisely the ease in which Hamiltonian evolution can be determined:

$$\begin{aligned}\left|\psi_E(t)\right\rangle &= \exp(-\mathrm{i}t\hat{\mathcal{H}}/\hbar)\hat{U}_R(\theta)\left|E\right\rangle \\ &= \alpha_0 e^{-\mathrm{i}Et/\hbar}\left|E\right\rangle + \sum_q \alpha_q^+ e^{-\mathrm{i}E_q^+ t/\hbar}\left|E_q^+\right\rangle + \sum_r \alpha_r^- e^{-\mathrm{i}E_r^- t/\hbar}\left|E_r^-\right\rangle .\end{aligned} \tag{3.95}$$

Thus, the contribution of $\left|E\right\rangle\!\left\langle E\right|$ term of the density matrix to $\left\langle \hat{J}_x\right\rangle$ to up first order

transitions can be written as,

$$\begin{aligned}\left\langle \hat{J}_x(t)\right\rangle_E &= \left\langle \psi_E(t)\right| \hat{J}_x \left|\psi_E(t)\right\rangle \\ &= 2\sum_q \Re\left(\alpha_0^*\alpha_q^+ e^{-\mathrm{i}(E_q^+-E)t/\hbar}\left\langle E\right| \hat{J}_x \left|E_q^+\right\rangle\right) \\ &\qquad + 2\sum_r \Re\left(\alpha_0^*\alpha_r^- e^{-\mathrm{i}(E_r^--E)t/\hbar}\left\langle E\right| \hat{J}_x \left|E_r^-\right\rangle\right) \\ &= (-4c_0^j(\theta)c_1^j(\theta)\sin(\theta/2))\Bigg(\sum_q \left|\left\langle E_q^+\right| \hat{J}_x \left|E\right\rangle\right|^2 \sin((E_q^+-E)t/\hbar) \\ &\qquad + \sum_r \left|\left\langle E_r^-\right| \hat{J}_x \left|E\right\rangle\right|^2 \sin((E_r^--E)t/\hbar)\Bigg). \end{aligned} \tag{3.96}$$

As it currently stands, the flip angle contribution is dependent on the angular momentum subspace containing $|E\rangle$. It shall be shown that under the assumption that $\theta \ll 1$, the j dependency vanishes. Two cases need to be considered in order to compute the expansions of $c_0^j(\theta)$ and $c_1^j(\theta)$, given by (3.80). If $2j$ is even, $\epsilon = 0$, and if $2j$ is odd, $\epsilon = 1$. The odd case can indeed occur since for odd N, all angular momentum subspaces are given by half integer representations. Then, for $\epsilon = 0$,

$$c_0^j(\theta) = 1. \tag{3.97}$$

For $\epsilon = 1$, recalling that x had been previously defined as $\sin^2(\theta/2)$,

$$\begin{aligned} c_0^j(\theta) &= \cos(\theta/2)\operatorname*{Trunc}_{\lfloor j-1/2\rfloor}\frac{1}{\sqrt{1-x}} \\ &= \cos(\theta/2)\operatorname*{Trunc}_{\lfloor j-1/2\rfloor}\left(1+\frac{x}{2}+\frac{3x^2}{8}+\cdots\right) \\ &= \cos(\theta/2)\left(1+\frac{\sin^2(\theta/2)}{2}+\cdots\right) \\ &= \left(1-\frac{\theta^2}{8}+O(\theta^4)\right)\left(1+\frac{\theta^2}{8}+O(\theta^4)\right) \\ &= 1+O(\theta^4). \end{aligned}$$

Notice that in the above derivation, were it not for the truncation operator,

$$\frac{\cos(\theta/2)}{\sqrt{1-\sin^2(\theta/2)}} = \frac{\cos(\theta/2)}{|\cos(\theta/2)|} = \pm 1, \tag{3.98}$$

and so for small angles and large values of j, this approximation is very close to the true value. Following a similar approach for $c_1^j(\theta)$, when $\epsilon = 0$,

$$\begin{aligned} c_1^j(\theta) &= 1 + \frac{\sin^2(\theta/2)}{6} + \frac{3\sin^4(\theta/2)}{40} + \cdots \\ &= 1 + \frac{\theta^2}{24} + O(\theta^4). \end{aligned}$$

For $\epsilon = 1$,

$$\begin{aligned} c_1^j(\theta) &= \cos(\theta/2)\left(1 + \frac{2\sin^2(\theta/2)}{3} + \frac{8\sin^4(\theta/2)}{15} + \cdots\right) \\ &= \left(1 - \frac{\theta^2}{8} + O(\theta^4)\right)\left(1 + \frac{\theta^2}{6} + O(\theta^4)\right) \\ &= 1 + \frac{\theta^2}{24} + O(\theta^4). \end{aligned}$$

Thus, under the small angle approximation, the j dependency on the effect of the flip-angle drops out completely, yielding

$$c_0(\theta) = 1 + O(\theta^4) \tag{3.99}$$

$$c_1(\theta) = 1 + \frac{\theta^2}{24} + O(\theta^4), \tag{3.100}$$

which holds for all values of j.

Then, for every initial state $|E\rangle$, the flip-angle contribution to $\left\langle \hat{J}_x \right\rangle_E$ is constant for every considered transition. Denoting this flip angle contribution as $F(\theta)$,

$$\begin{aligned} F(\theta) &= -4\big(1 + O(\theta^4)\big)\big(1 + \theta^2/24 + O(\theta^4)\big)\big(\theta/2 + \theta^3/48 + O(\theta^5)\big) \\ &= -2\theta\big(1 + O(\theta^4)\big)\big(1 + \theta^2/24 + O(\theta^4)\big)\big(1 - \theta^2/24 + O(\theta^4)\big) \\ &= -2\theta + O(\theta^5). \end{aligned} \tag{3.101}$$

Thus, for small flip-angles θ, one can very well approximate the flip angle contribution as a global amplitude on the FID of the spin ensemble, depending linearly on θ. Note that the global flip-angle dependence for $\theta \ll 1$ generally applies to any collective spin system with conserved excitations and angular momentum. The particular frequencies of the sine functions, multiplied by the relevant matrix elements of the energy eigenvectors and thermal population, determine the fine structure particular to the Tavis-Cummings Hamiltonian.

Putting everything together, the FID signal due to a full thermal density matrix can be effectively determined. Take the evolving density matrix to be

$$\hat{\rho}(t) = \exp\big(-\mathrm{i}t\hat{\mathcal{H}}/\hbar\big)\hat{U}_R(\theta)\hat{\rho}\hat{U}_R(\theta)^\dagger \exp\big(\mathrm{i}t\hat{\mathcal{H}}/\hbar\big). \tag{3.102}$$

Then,

$$\begin{aligned}
\Big\langle \hat{J}_x(t)\Big\rangle &= \mathrm{tr}\left(\hat{J}_x\hat{\rho}(t)\right) \\
&= \sum_E P(E)\,\mathrm{tr}\left(\hat{J}_x\left|\psi_E(t)\right\rangle\!\left\langle\psi_E(t)\right|\right) \\
&= \sum_E P(E)\left\langle \hat{J}_x(t)\right\rangle_E \\
&= F(\theta)\sum_E P(E)\Bigg(\sum_q \left|\left\langle E_q^+\right|\hat{J}_x\left|E\right\rangle\right|^2 \sin((E_q^+ - E)t/\hbar) \\
&\qquad\qquad + \sum_r \left|\left\langle E_r^-\right|\hat{J}_x\left|E\right\rangle\right|^2 \sin((E_r^- - E)t/\hbar)\Bigg) \qquad (3.103) \\
&= \frac{1}{2}F(\theta)\sum_E P(E)\Bigg(\sum_q \left|\left\langle E_q^+\right|\hat{J}_+\left|E\right\rangle\right|^2 \sin((E_q^+ - E)t/\hbar) \\
&\qquad\qquad + \sum_r \left|\left\langle E_r^-\right|\hat{J}_-\left|E\right\rangle\right|^2 \sin((E_r^- - E)t/\hbar)\Bigg). \qquad (3.104)
\end{aligned}$$

The FID signal, being a large complicated sum of sine functions, is not very useful in its current form, as the more relevant observable is the Fourier transform of the signal. Luckily, the Fourier transform of a sinusoidal function is easy to determine,

$$\mathcal{F}[\sin(\omega_0 t)](\omega) = -\mathrm{i}\pi\big(\delta(\omega-\omega_0) - \delta(\omega+\omega_0)\big), \tag{3.105}$$

where $\delta(\omega)$ is the Dirac δ-function. Thus, under unitary evolution and a small flip-angle, the spectrum is a weighted sum of Dirac δ-functions, whose locations and amplitudes can be predicted with relative ease. Each eigenstate, $|E\rangle$, induces a set of peaks through transitions to states differing by a single excitations, $|E_f\rangle$, located at

$$\omega_{peak} = \pm\frac{1}{\hbar}\big(E_f - E\big), \tag{3.106}$$

with the modulus of the complex amplitude given by

$$A_{peak} = 2\pi\,|\theta|\,P(E)\left|\left\langle E_f\right|\hat{J}_x\left|E\right\rangle\right|^2 + O(\theta^5). \tag{3.107}$$

Further particularizing to the case of the Tavis-Cummings system, if E is a k excitation state with an energy level splitting eigenvalue of λ_i, then E_f must be a $k \pm 1$ excitation state. Define the energy level splitting eigenvalue of E_f as λ_f. Then,

$$\begin{aligned} \pm\frac{1}{\hbar}\big(E_f - E\big) &= \pm\big((k \pm 1)\omega_0 + \lambda_f g_0 - k\omega - \lambda_i g_0\big) \\ &= \pm\big(\pm\omega_0 + (\lambda_f - \lambda_i)g_0\big), \end{aligned} \tag{3.108}$$

where it should be understood that all four possible combinations of signs are valid frequencies. That is, coupling to a $k+1$ and $k-1$ excitation state both induce a peak about $+\omega_0$ and $-\omega_0$, with equal magnitude. This implies the spectrum is symmetric about $\omega = 0$, as one might expect.

With the small angle dependence determined, it remains to compute the necessary matrix elements, as well as thermal populations, in order to compute the shape of the spectrum. To do so, one can particularize a set of parameters appeal to numerics. Given $N = 100$, $T = 0.12\text{K}$, $\omega_0 = 10\text{GHz}$, and $g_0 = 10\text{Hz}$, the figure 3.33 shows the spectrum due to $\hat{J}_+$ transitions, and figure 3.34 shows the spectrum due to $\hat{J}_-$ transitions. The spectrum due to $\hat{J}_x$ is then the average of the two spectra.

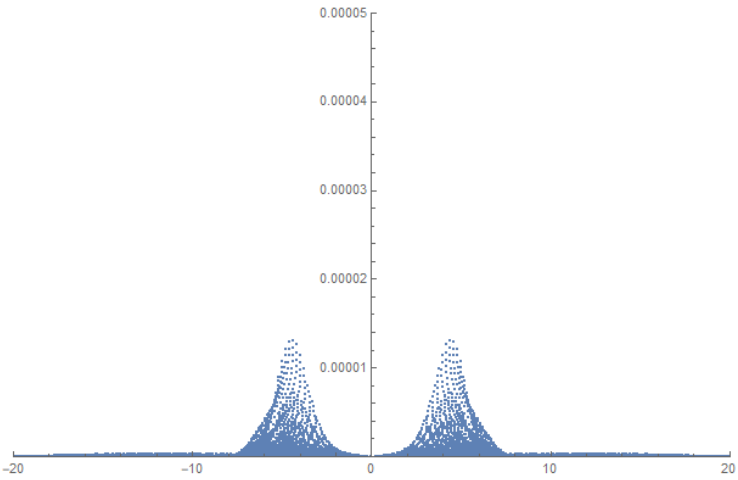

Figure 3.33: Fourier spectrum of the observable $\left\langle \hat{J}_+(t) \right\rangle$. The horizontal axis is in units of g_0, shifted so that $\omega_0 = 10\text{GHz}$ is located at the origin. The vertical axis is the peak amplitude given in equation (3.107), divided by $2\pi\theta$. For reference, $\omega_0 + g_0\sqrt{N}$ is located at 10 on the horizontal axis. Notice that the two peaks are split approximately .6 of $g_0\sqrt{N}$, markedly narrower than the Dicke prediction.

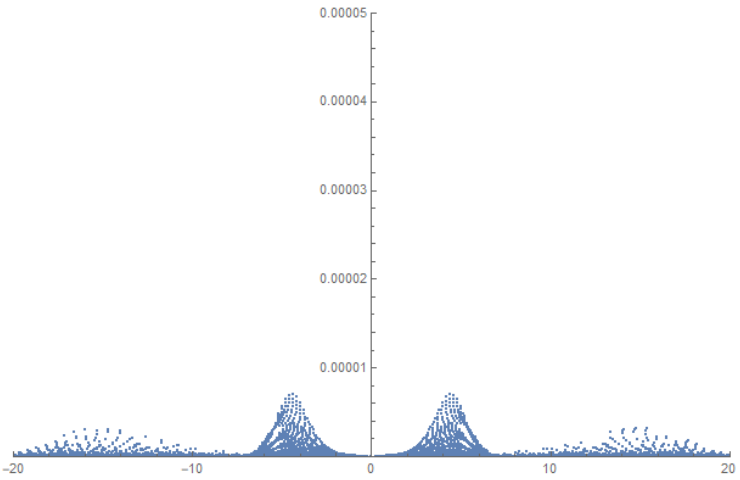

Figure 3.34: Spectrum of the observable $\left\langle \hat{J}_-(t) \right\rangle$. The horizontal axis is in units of g_0, shifted so that $\omega_0 = 10\text{GHz}$ is located at the origin. The vertical axis is the peak amplitude given in equation (3.107), divided by $2\pi\theta$. For reference, $\omega_0 + g_0\sqrt{N}$ is located at 10 on the horizontal axis.

Using insights from signal analysis, given an exponential decay process on the measurement signal each point corresponding to a delta function peak would then transform into the peak of a Lorentzian, of width dependent on the decay time scale. Thus for an experiment in the laboratory, where the sample is in contact with some environment, as described by a Lindblad master equation, the spectrum would be broadened as compared to the calculated peaks in figures 3.33 and 3.34. That being said, it is unlikely that a noise process of this form would cause a shift in the center frequency of these peaks, and thus the qualitative structure should remain. This is further reinforced if the experiment is done in a cavity with a large quality factor, meaning the quantum system has very long coherence times.

In order to extend this result to the case when the flip-angle θ is not small, retracing the previous derivation before the approximations shows that one needs to modify the values α_0 and $\alpha_q^{\pm}$. This is done by considering the entire polynomial expansion for $\hat{U}_R(\theta)$. Then,

α_0 is sensitive to all even powers of $\hat{J}_x$ and $\alpha_q^{\pm}$ is sensitive to all odd powers of $\hat{J}_x$. Thus,

$$\begin{aligned}\alpha_0 &= c_0^j(\theta) - \frac{4c_2^j(\theta)\sin^2(\theta/2)}{4!}\left\langle E\right|\hat{J}_x^2\left|E\right\rangle + \cdots \\ &= \sum_{i=0}^{j}\frac{(-1)^i 4^i}{(2i)!}c_{2i}^j(\theta)\big(\sin^2(\theta/2)\big)^i\left\langle E\right|\hat{J}_x^{2i}\left|E\right\rangle . \end{aligned} \tag{3.109}$$

Similarly,

$$\alpha_q^{\pm} = -2\mathrm{i}\sum_{i=0}^{j-1}\frac{(-1)^i 4^i}{(2i+1)!}c_{2i+1}^j(\theta)\big(\sin(\theta/2)\big)^{2i+1}\left\langle E_q^{\pm}\right|\hat{J}_x^{2i+1}\left|E\right\rangle . \tag{3.110}$$

The difficulty of computing these equations for general θ almost entirely the cost of the higher order matrix elements. Since $\hat{J}_x$ couples an excitation space to neighboring excitation blocks, the relevant portion of its action must be represented with at least 3 blocks worth of dimensionality. Applying the same argument to $\hat{J}_x^2$, one must now consider the action of the operator across 5 neighboring excitation spaces in order to determine the values of the relevant central 3 blocks. In this approach, the dimension of the necessary matrix grows wildly. If one attempts instead to consider the action of powers of $\hat{J}_x$ as a sum of products of $\hat{J}_+$ and $\hat{J}_-$, then this matrix element can be thought of as a walk through excitation subspaces. Though, this yields the issue that for the $2i$-th power of $\hat{J}_x$ there are $\binom{2i}{i} \sim 4^i/\sqrt{i}$ possible paths, as $i \longrightarrow \infty$ [44]. The number of relevant terms for the $2i+1$-st powers of $\hat{J}_x$ are computed similarly, with identical asymptotic behavior. For example, at third order in $\hat{J}_x$, the relevant portion of the action of $\hat{J}_x^3$ is given by

$$\left\langle E_q^{\pm}\right|\hat{J}_x^{2i+1}\left|E\right\rangle = \frac{1}{2^3}\left\langle E_q^{+}\right|\left(\hat{J}_+\hat{J}_+\hat{J}_- + \hat{J}_+\hat{J}_-\hat{J}_+ + \hat{J}_-\hat{J}_+\hat{J}_+\right)|E\rangle . \tag{3.111}$$

Since the range over which i runs takes a maximum at $N/2$, this means that the number of products to be considered is almost exponential in N. The resulting matrix element must then be written as sum over $\binom{2i}{i}$ (or $\binom{2i+1}{i+1}$) terms, each of which is a product of $2i$ (or $2i+1$) floating points. For now, it seems, exact computations with general flip-angles are out of reach.

Even if one is unable to compute the shape of this spectrum, there is a still a little that can be said about its qualitative behaviour. Since the eigenstructure is unchanged, and the focus is still on the spectral region about ω_0, the locations of each δ-function are unchanged. What is changed is then the magnitude of each peak. For small θ, this work has determined that the shape of the spectrum is dependent on temperature, with a magnitude scaling linearly in θ. For larger values of θ, it is as of yet unclear how varying θ

and T will impact the overall shape and magnitude of the resultant spectrum. In any case, from the overwhelming evidence of this section, it appears that the Dicke approximation fails in all but the coldest experimental situations.

3.4 Cavity Mediated Spin-Spin Coherence

The notion of multi-body spin coherence in NMR stems from the language in which the states are written. In high temperature NMR, the assumed state for a single spin species is a thermal density matrix with a minute polarization, $0 < \epsilon \ll 1$,

$$\hat{\rho}_1 = \frac{1}{2}(\mathbb{1} + \epsilon\hat{\sigma}_z). \tag{3.112}$$

In reality there can be on the order of 10^{23} spins present in a single sample, but for all experimental purposes, the measurement signals are identical to having averaged many experiments on a single spin of the same species as the bulk. Consider even a composite density matrix of two spins:

$$\hat{\rho}_2 = \frac{1}{4}\big(\mathbb{1} + 2\epsilon\hat{J}_z + \epsilon^2\hat{\sigma}_z^{(1)}\hat{\sigma}_z^{(2)}\big). \tag{3.113}$$

In many cases, the *second order spin coherence* term, where two Pauli operators are tensored together, is completely neglected. This is entirely reasonable when one considers that if the polarization, ϵ, is on the order of 10^{-6}, then ϵ^2 is on the order of 10^{-12} and significantly more difficult to observe. Further, if the observable being measured is a collective spin operator, such as $\hat{J}_z$, then without a specially designed pulse sequence the higher order terms won't even come into the signal. That being said, it is entirely possible to experimentally measure these quantities, and non-zero values of higher order spin coherence terms are attributed to the build up of correlations and entanglement [41, 3, 23, 28]. Generally these terms most interesting in the presence of spin-spin interaction Hamiltonian, which can produce non-trivial quantum correlations and be used to investigate the scrambling of quantum information through an environment of spins, among other phenomenon [28].

As it currently stands, the Tavis-Cummings Hamiltonian has no spin-spin interaction term. Though, spins can interact by exchanging quantum information through the cavity. The super conducting qubit community often utilizes a cavity to engineer entangling gates between otherwise non-interacting qubits, with good success [3].

Given the tools of the previous sections, one can investigate the effect the cavity has on spin-spin coherence for thermal spin ensembles. In particular, one should be able to answer the question, does thermalizing in the presence of a cavity enhance or inhibit spin-spin correlations as compared to a isolated spin ensemble? For a baseline, consider the thermal state of an isolated spin ensemble of N spins with inverse temperature $\beta = 1/(k_B T)$ and Hamiltonian

$$\hat{\mathcal{H}}_s = \hbar\omega_0\hat{J}_z. \tag{3.114}$$

Then,

$$\hat{\rho}_{th} = \frac{1}{Z(\beta)} e^{-\beta \hat{\mathcal{H}}_s} = \prod_{i=1}^{N} \frac{1}{2} \left(\mathbb{1} - \tanh\left(\frac{\hbar\omega_0}{2k_B T}\right) \hat{\sigma}_z^{(i)} \right). \tag{3.115}$$

Now, expanding out the product into sums,

$$\hat{\rho}_{th} = \frac{1}{2^N} \left(\mathbb{1} - \tanh\left(\frac{\hbar\omega_0}{2k_B T}\right) \sum_{i=1}^{N} \hat{\sigma}_z^{(i)} + \tanh^2\left(\frac{\hbar\omega_0}{2k_B T}\right) \sum_{i \neq j}^{N} \hat{\sigma}_z^{(i)} \hat{\sigma}_z^{(j)} - \cdots \right). \tag{3.116}$$

It is then clear that the m-th order spin coherence term of the thermal density matrix is weighted by $\tanh^m(0.5\beta\hbar\omega_0)$.

In order to connect these weights with the Tavis-Cummings Hamiltonian, it is convenient to rewrite the sums over Pauli operators in terms of collective operators. In this language it will be possible to write the m-th weight as an expectation value of a collective operator. For $m = 1$, the procedure is simple,

$$\sum_{i=1}^{N} \hat{\sigma}_z^{(i)} = 2\hat{J}_z. \tag{3.117}$$

To illustrate the behavior for higher order terms, consider the $m = 2$ case carefully:

$$\begin{aligned}
\sum_{i \neq j}^{N} \hat{\sigma}_z^{(i)} \hat{\sigma}_z^{(j)} &= \sum_{i,j=1}^{N} \left(\hat{\sigma}_z^{(i)} \hat{\sigma}_z^{(j)} - \delta_{ij} \hat{\sigma}_z^{(i)} \hat{\sigma}_z^{(j)} \right) \\
&= \sum_{i,j=1}^{N} \hat{\sigma}_z^{(i)} \hat{\sigma}_z^{(j)} - \sum_{i=1}^{N} (\hat{\sigma}_z^{(i)})^2 \\
&= \left(\sum_{i=1}^{N} \hat{\sigma}_z^{(i)} \right) \left(\sum_{j=1}^{N} \hat{\sigma}_z^{(j)} \right) - \sum_{i=1}^{N} \mathbb{1} \\
&= 4\hat{J}_z^2 - N\mathbb{1}.
\end{aligned} \tag{3.118}$$

As the order increases, the algebra becomes increasingly more challenging. To summarize the procedure, one first rewrites the sum so that leading order can be written as

$$2^m \hat{J}_z^m, \tag{3.119}$$

and then subtracts off all the terms introduced in order to ensure equality. While difficult to parse, there is a generating function that sets up the algebraic problem. Denote the

spin-spin coherence operator as $\hat{C}_m$, which is given by the unscaled sum of products of Pauli operators, as per the expanded multi-body thermal state. Then,

$$\hat{C}_m = \sum_{i_1,\cdots,i_m=1}^{N} \Bigg(\Big(\prod_{l=1}^{m} \hat{\sigma}_z^{(i_l)}\Big)\Big(\prod_{(p,q)\in S_2(m)} (1-\delta_{i_p i_q})\Big)\Bigg). \tag{3.120}$$

Above, the set $S_2(m)$ denotes the set of all unique combinations of integers from 1 to m of length two. For example,

$$S_2(2) = \{(1,2)\} \tag{3.121}$$
$$S_2(3) = \{(1,2),(1,3),(2,3)\}. \tag{3.122}$$

Utilizing this formula it is possible, albeit tedious, to simplify the entire expression down to a polynomial in $\hat{J}_z$. The first few are listed below:

$$\hat{C}_0 = \mathbb{1} \tag{3.123}$$
$$\hat{C}_1 = 2\hat{J}_z \tag{3.124}$$
$$\hat{C}_2 = 4\hat{J}_z^2 - N\mathbb{1} \tag{3.125}$$
$$\hat{C}_3 = 8\hat{J}_z^3 - (6N-4)\hat{J}_z \tag{3.126}$$
$$\hat{C}_4 = 16\hat{J}_z^4 - (24N-32)\hat{J}_z^2 + (3N^2-6N)\mathbb{1} \tag{3.127}$$
$$\hat{C}_5 = 32\hat{J}_z^5 - (80N-160)\hat{J}_z^3 + (30N^2-100N+48)\hat{J}_z. \tag{3.128}$$

Now, it must be the case that $\hat{C}_m$ are trace 0 for all $m \geq 1$. Thus, there are a few relations worth noting:

$$\operatorname{tr} \hat{J}_z^2 = N2^{N-2}$$
$$\operatorname{tr} \hat{J}_z^3 = 0$$
$$\operatorname{tr} \hat{J}_z^4 = (24N-32)N2^{N-6} - N(3N-6)2^{N-4}$$
$$\operatorname{tr} \hat{J}_z^5 = 0$$

These formulae can be utilized to related weights of the spin coherence operators to expectation values of observables. Given a more general density operator, still only polarized along the z direction, define coefficients α_m such that

$$\hat{\rho} = \frac{1}{2^N}\Big(\mathbb{1} + \alpha_1\hat{C}_1 + \alpha_2\hat{C}_2 + \cdots\Big). \tag{3.129}$$

Then,

$$\left\langle \hat{J}_z \right\rangle = \frac{\alpha_1 N}{2}, \tag{3.130}$$

and the fact that

$$\operatorname{tr} \hat{J}_z \hat{C}_m = 0, \ m \geq 2 \tag{3.131}$$

can be checked in either representation, though it is more obvious using the Pauli sums. For example, for $m = 2$,

$$\hat{J}_z \hat{C}_2 = \frac{1}{2}\left(\sum_{k=1}^{N} \hat{\sigma}_z^{(k)} \right)\left(\sum_{i \neq j}^{N} \hat{\sigma}_z^{(i)} \hat{\sigma}_z^{(j)} \right), \tag{3.132}$$

it clear that the full sum over Pauli operators from the $\hat{J}_z$ can cancel at most one Pauli within the sum expansion of $\hat{C}_2$. Thus in every term of the resulting sum, there is at least one Pauli operator present, which necessitates a 0 trace. This exact argument for counting the number of Pauli operators present in each term of a sum can be used to show the following trace relation:

$$\operatorname{tr} \hat{J}_z^k \hat{C}_m = 0, \ N \geq m > k. \tag{3.133}$$

Solving for the weight, one finds

$$\alpha_1 = 2 \left\langle \hat{J}_z \right\rangle / N. \tag{3.134}$$

This can be similarly done for the next weight, by first computing $\left\langle \hat{J}_z^2 \right\rangle$. After solving and simplifying,

$$\alpha_2 = \frac{2}{N(N-1)}\left(\left\langle \hat{J}_z^2 \right\rangle - \frac{N}{4} \right). \tag{3.135}$$

Thus, under the promise that a state $\hat{\rho}$ can be written as per equation (3.129), one is able to measure the weights of the coherence operators directly through expectation values of collective observables.

The desire to experimentally determine the weights of the coherence operators in a spin sample which thermalized in the presence of a cavity motivates an expression for computing expectation values of $\hat{J}_z^m$. Assuming that a partial trace over the cavity Hilbert space results in a spin state which can be written of the form given in equation (3.129), the expectation values of $\hat{J}_z^m$ will allow direct comparison to a thermal spin ensemble which thermalized without a cavity present.

In a somewhat surprising manner, expectation values of $\hat{J}_z^m$ can be computed directly on thermal states of the Tavis-Cummings Hamiltonian, under a few scaling assumptions. The trick is to write out all matrix representations in the excitation basis, that is, to not rediagonalize under the interaction Hamiltonian. In this basis, powers of $\hat{J}_z^m$ have diagonal representations, and are thus trivial to compute.

Consider first for a moment an (un-normalized) thermal density operator with respect to the Tavis-Cummings Hamiltonian:

$$e^{-\beta\hat{\mathcal{H}}} = \exp\left(-\beta\hbar\omega_0\hat{K}\right)\sum_{j,k} d_j \exp\left(-\beta\hbar g_0\hat{L}(j,k)\right). \tag{3.136}$$

In the above equation, recall that $\hat{K}$ is the excitation operator, and $\hat{L}(j,k)$ is the representation of the interaction part of the Hamiltonian in a particular angular momentum and excitation subspace. Since these operators commute, and the excitation operator is diagonal within a subspace, they can be rewritten using their representations within each subspace:

$$e^{-\beta\hat{\mathcal{H}}} = \sum_{j,k} d_j e^{-\beta\hbar\omega_0 k}\exp\left(-\beta\hbar g_0\hat{L}(j,k)\right) = \sum_{j,k} d_j e^{-\beta\hbar\omega_0 k}\sum_{i=0}^{\infty}\frac{(-\beta\hbar g_0)^i\hat{L}(j,k)^i}{i!}. \tag{3.137}$$

Now, under the assumption that $\beta\hbar g_0$ is small enough to truncate the Taylor expansion for the fine structure of the thermal state, the infinite sum can be truncated. Since the goal is to find $\left\langle \hat{J}_z^m\right\rangle$, which is diagonal in the excitation basis, it is most efficient to use the same representation for the interaction portion of the Hamiltonian. Thus, take the coupling matrix representation of the interaction Hamiltonian, $L(j,k)$, which is a hollow tri-diagonal matrix.

By linearity of the trace, expectation values of $\hat{J}_z^m$ reduce to computing the following traces, such that $i, m \in \mathbb{Z}_+$,

$$\operatorname{tr} L(j,k)^i\hat{J}_z^m. \tag{3.138}$$

Now, odd powers of $L(j,k)$ have a 0 diagonal, and thus the product with powers of $\hat{J}_z$ will have a 0 trace. That is, one can neglect the first and third order terms, leaving the zeroth and second order terms dominating. Under this truncation of the Taylor series for the fine structure of the thermal state, there is but a fourth order error, scaling as $O((\beta\hbar g_0\left|L(j,k)\right|_\infty)^4)$. It remains to compute the zeroth and second order traces. Recall that the dimension of the subspace with angular momentum j and k excitations above the

ground state has dimension $D_{j,k} = n(j,k) + 1$, and the square of the coupling matrix is written as

$$L(j,k)^2 = \begin{bmatrix} l_1^2 & 0 & l_1 l_2 & & & & \\ 0 & l_1^2 + l_2^2 & 0 & l_2 l_3 & & & \\ l_1 l_2 & 0 & \ddots & \ddots & \ddots & & \\ & l_2 l_3 & \ddots & \ddots & \ddots & l_{n-1} l_n & \\ & & \ddots & \ddots & l_{n-1}^2 + l_n^2 & 0 & \\ & & & l_{n-1} l_n & 0 & l_n^2 & \end{bmatrix}. \tag{3.139}$$

Then similarly, the representation of $\hat{J}_z^m$ can be written explicitly in each j, k basis, which is given as

$$J_z(j,k)^m = \begin{bmatrix} (-j)^m & & & \\ & (-j+1)^m & & \\ & & \ddots & \\ & & & (-j+n)^m \end{bmatrix}. \tag{3.140}$$

Thus, the zeroth order trace is given by the sum,

$$\operatorname{tr} L(j,k)^0 J_z(j,k)^m = \sum_{p=0}^{n(j,k)} (-j+p)^m. \tag{3.141}$$

Taking the convention that $l_0(j,k) = l_{n+1}(j,k) = 0$, the second order trace is further given by,

$$\operatorname{tr} L(j,k)^2 J_z(j,k)^m = \sum_{p=0}^{n(j,k)} \big(l_p^2 + l_{p+1}^2\big)\big(-j+p\big)^m. \tag{3.142}$$

All the pieces are present to write down a truncated expression for the expectation values of powers of $\hat{J}_z$.

Defining the partition function as usual, such that $Z(\beta) = \operatorname{tr} \exp(-\beta \hat{\mathcal{H}})$, the thermal expectation values of relevance are given as

$$\left\langle \hat{J}_z^m \right\rangle = \frac{1}{Z(\beta)} \operatorname{tr} e^{-\beta \hat{\mathcal{H}}} \hat{J}_z^m. \tag{3.143}$$

Expanding out the expression into computationally friendly sums,

$$\left\langle \hat{J}_z^m \right\rangle = \frac{1}{Z(\beta)} \sum_{j,k} d_j e^{-\beta\hbar\omega_0 k} \Bigg(\sum_{p=0}^{n(j,k)} \Big((-j+p)^m + \frac{(\beta\hbar g_0)^2}{2} \big(l_p^2 + l_{p+1}^2\big) \big(-j+p\big)^m \Big) + O\big((\beta\hbar g_0 \left|L(j,k)\right|_\infty)^4\big) \Bigg). \tag{3.144}$$

Now, the error term is still within the sum over all non-interacting subspaces, and in principle has some dependence on j and k. The belief is that since $g_0 \approx 10^{-9}\omega_0$ in most experimental situations, the magnitude of the error due to the omission of these fine structure terms will be highly suppressed, leaving this expression as a good approximation of the true expectation value.

Consider once more $N = 100$ spins at $\omega_0 = 10$ GHz coupled to a quantized field with $g_0 = 10$ Hz. For a spin ensemble with no cavity present, the thermal expectation values of $\hat{J}_z$ and $\hat{J}_z^2$ can be easily computed using the trace relations and the expanded thermal state. These functions of temperature shall be used as a baseline reference for values extracted from equation (3.144).

$$\left\langle \hat{J}_z \right\rangle = \frac{\alpha_1 N}{2} = -\frac{N}{2} \tanh\big(\frac{\hbar\omega_0}{2k_B T}\big). \tag{3.145}$$

Similarly,

$$\left\langle \hat{J}_z^2 \right\rangle = \frac{N(N-1)}{2}\alpha_2 + \frac{N}{4} = \frac{N(N-1)}{2} \tanh^2\big(\frac{\hbar\omega_0}{2k_B T}\big) + \frac{N}{4} \tag{3.146}$$

The following plots compare the temperature dependencies of $\left\langle \hat{J}_z \right\rangle$ and $\left\langle \hat{J}_z^2 \right\rangle$ at temperatures below 1 K, for the spin ensemble and the Tavis-Cummings ensemble.

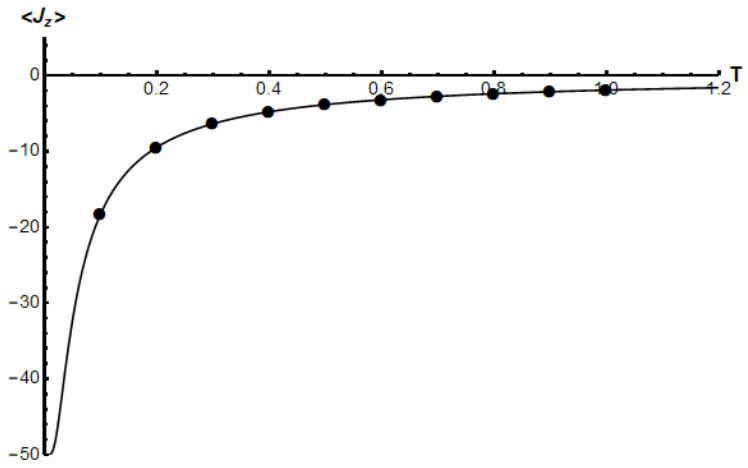

Figure 3.35: Plots of $\left\langle \hat{J}_z \right\rangle$ as a function of temperature for an $N = 100$ spin ensemble. The solid line is plot of equation (3.145), the lone spin ensemble prediction. The points give computed values of equation (3.144) particularized to $m = 1$, the TC model estimation for $\left\langle \hat{J}_z \right\rangle$. Notice the close agreement between these values.

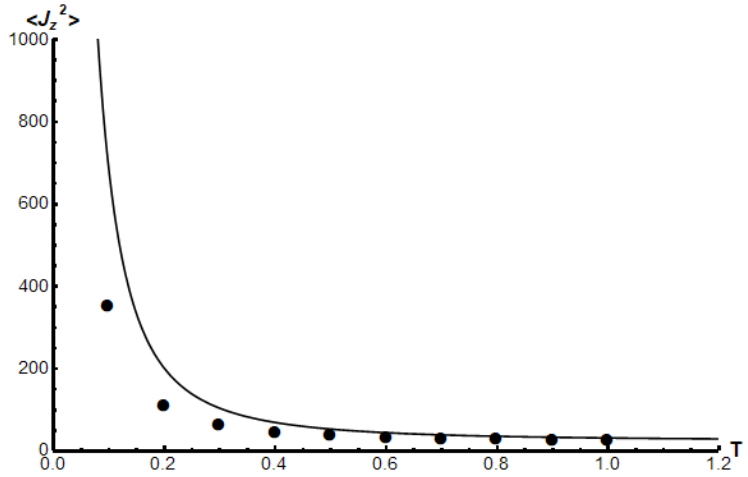

Figure 3.36: Plots of $\left\langle \hat{J}_z^2 \right\rangle$ as a function of temperature for an $N = 100$ spin ensemble. The solid line is plot of equation (3.146), the lone spin ensemble prediction. The points give computed values of equation (3.144) particularized to $m = 2$, the TC model estimation for $\left\langle \hat{J}_z^2 \right\rangle$. Notice the poor agreement between these values at low temperatures.

The plot of $\left\langle \hat{J}_z^2 \right\rangle$ within figure 3.36 shows that the spin ensemble and the Tavis-Cummings system have a clear deviation in these expectation values. Somewhat surprisingly, $\left\langle \hat{J}_z \right\rangle$ seems to be very similar for the two systems. Closer inspection into the points will show that this is not truly the case. Consider a plot of the absolute value of the difference between those two curves.

Figure 3.37 shows that while the two curves are indeed close, they differ by about 10^{-6}, and the magnitude of this difference appears to be an increasing function of temperature. This is contrasted with the plots of $\left\langle \hat{J}_z^2 \right\rangle$, which has a the deviation decreasing as a function of temperature. It should be noted that this deviation must be bounded, as the infinite temperature limit of the two expectation values must both be 0, and thus their differences also eventually converge to 0.

It is unlikely that these deviations are caused by the error terms. Focusing once more on equation (3.144), the difference between this expectation value and the spin only case is deeper than just the correction term proportional to g_0^2. While $\hat{J}_z$ is only sensitive to spin excitations, the thermal populations of the eigenstates is based on the total excitations present in that state. To clarify, consider a simple pure state of the form $|j, -j+1\rangle |1\rangle$. In the Tavis-Cummings setting, this state would be thermally weighted as a state with

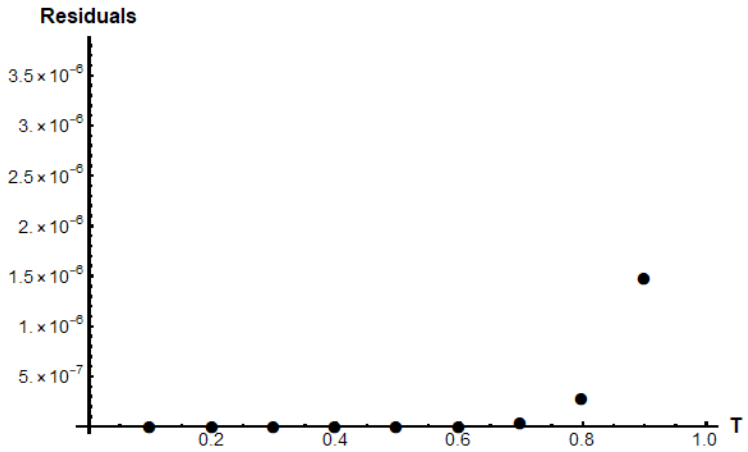

Figure 3.37: Plots of the absolute value of the difference $\left\langle \hat{J}_z \right\rangle$ for a lone spin ensemble and a Tavis-Cummings system, with $N = 100$ spins present in the ensemble. Notice the apparent divergence in predictions with increasing temperature.

two excitations, picking up a factor of $\exp(-2\beta\hbar\omega_0)$, divided by the partition function. For comparison, a spin ensemble (no cavity present) would energetically see that this state has but a single excitation, and so its thermal factor would instead be $\exp(-\beta\hbar\omega_0)$, divided by the partition function. In effect, any given eigenvalue of $\hat{J}_z$ will contribute to the expectation value multiple times with different thermal pre-factors, due to the fact that the spins thermalized with the cavity present. This effect is amplified for computing expectation values of higher powers of $\hat{J}_z$, due to the increase in magnitude of overall scale.

The computed expectation values have thus far been static thermal values. Recall that $\hat{J}_z$ does not commute with the entire Tavis-Cummings Hamiltonian, and thus will have a non-trivial time evolution for many states. If one were able to perform a radio-frequency pulse along the z direction within the lab frame, then the excited coherences would be confined to a single excitation subspace. The resulting time evolution of these coherences should then be observable through a FID measurement of $\left\langle \hat{J}_z^m(t) \right\rangle$. Assuming that the initial state of the system is thermal before the coherences are excited, the same procedure of calculating a Fermi spectrum for $\hat{J}_x$ should apply to $\hat{J}_z$ as well. As expected, the first attempt shall consider a small flip angle, $\theta \ll 1$, which in this case corresponds to a pulse unitary of the form

$$\hat{U}_R(\theta) = \exp\big(-\mathrm{i}\theta\hat{J}_z\big). \tag{3.147}$$

Under a z pulse, only a single excitation subspace will have excited coherences for a

given initial state $|E\rangle$. Then,

$$\hat{U}_R(\theta)\,|E\rangle = \sum_i \alpha_i\,|E_i\rangle\,. \tag{3.148}$$

By orthonormality of the energy eigenbasis,

$$\begin{aligned}\alpha_i &= \left\langle E_i \right| \hat{U}_R(\theta) \left| E \right\rangle \\ &= c_0^j(\theta) - 2\mathrm{i}c_1^j(\theta)\sin(\theta/2)\left\langle E_i \right| \hat{J}_z \left| E \right\rangle \\ &\qquad - 2c_2^j(\theta)\sin^2(\theta/2)\left\langle E_i \right| \hat{J}_z^2 \left| E \right\rangle + \cdots\,.\end{aligned} \tag{3.149}$$

Pressing forward without computing or simplifying the expansion of equation (3.149), the expectation value for $\hat{J}_z$ can be computed as a time dependent quantity,

$$\left\langle \hat{J}_z(t) \right\rangle_E = \sum_{p,q} \left(\alpha_p^* e^{\mathrm{i}E_p t/\hbar}\right)\left(\alpha_q e^{-\mathrm{i}E_q t/\hbar}\right)\left\langle E_p \right| \hat{J}_z \left| E_q \right\rangle. \tag{3.150}$$

Notice that unlike the expectation value for $\hat{J}_x$, which was computed by two single sums, the expectation value for $\hat{J}_z$ requires the computation of a double sum. Further note that the matrix element of equation (3.150) is not the corresponding complex conjugate of equation (3.149). This would appear to indicate that for a given pair of eigenstates of energy E_p and E_q, the magnitude of the frequency mode at $\omega = (E_p \pm E_q)/\hbar$ is more complicated than an absolute value of a matrix element. Given that a measurement of $\hat{J}_z$ is only sensitive to coherences within a given excitation subspace, the induced frequency modes in an FID measurement will be centered about $\omega = 0$, making a measurement of these signals highly sensitive to factors such as $1/f$ noise. Thus, a measurement of this type is more sensitive to noise sources and more difficult to compute. As such, further progress into this derivation is experimentally unmotivated.

Chapter 4

Conclusion and Future Work

4.1 Spin Diffusion

By considering highly polarized ensemble quantum spin systems, one can treat the quantum density matrix as an ensemble of pure states undergoing random walk transport. It should be noted that quantum models with flip-flop coupling often lead to ballistic transport of energy. That is, the standard deviation of motion scales linearly with time, as opposed to diffusion where it scales as the square root. These results are well known and confirmed in many one dimensional models [55, 47], but the complexity of 3 spatial dimensions, especially those with all-to-all connections no translational invariance, has inhibited a complete investigation into coherent transport behavior in large systems[47].

Under the assumption that diffusion is a good model for transport of magnetization in large highly polarized crystals, this method should be able to be confirmed in the near future by low temperature experiments utilizing state of the art dynamic polarization techniques. There is a surprising yet reassuring coincidence that the computed magnitudes of the diffusion coefficient at low polarization is on the same order as the diffusion coefficient at high temperature. The fact that similar values are obtained for the same physical phenomenon utilizing vastly different formulations lends hope to the validity of this argument.

Confirmation of the diffusive transport assumption by future experiments will hopefully motivate a re-examination of how quantum transport is treated in non-integrable quantum systems. Further theoretical investigation into the origin of the approximate cube root dependence of the diffusion coefficient on polarization could end up being very fruitful. It is expected that the true dependence of diffusivity on polarization is much more complicated,

though it is certainly known that the diffusion rate should be 0 when the crystal is fully polarized, which this model does not reproduce.

4.2 Cavity QED

The research on the Tavis-Cummings Hamiltonian began as an investigation into determining the structure of higher order energy level splittings present within the Tavis-Cummings model, that is, splittings other than $\pm g_0\sqrt{N}$. During the many discussions and presentations of this work within Cory group, these shifts were referred to as Lamb shifts, in part due to the historical similarity of a quantized field splitting otherwise degenerate energy levels of angular momentum states. Within this work, hybridization of otherwise degenerate energy levels have simply been referred to as energy level splittings to avoid confusion.

There had been previously been a great deal of research into the behavior of a Tavis-Cummings system within the Dicke subspace, and the first goal of this work was to extend the procedure to other angular momentum subspaces. By thinking in this manner, it was discovered that by simply utilizing representations of the actions of $\hat{J}_z$, that it was possible to reduce the task of solving the Hamiltonian to finding eigenvalues of tridiagonal matrices, with dimension bounded by $N + 1$. Pushing forward and trying a multitude of theoretical tools to extract as much information as possible, it was found that the eigenvalue problem on these types of matrices had a huge computational speedup. It was assuredly the computational speed of computing the partition function for visualizing various behavior that allowed many of these new insights to come to light.

The study of the Tavis-Cummings Hamiltonian is far from complete. This particular new method into inspecting the intricacies present merely scratches the surface of what can be discovered. The connection of the coupling matrices to Jacobi operators, and thus orthogonal polynomials, is an exciting direction for continued theoretic research into the structure of this Hamiltonian.

Further, a great portion of this work was restricted to Gibbs thermal states. This restriction seems reasonable in a great many laboratory situations, but can most definitely be relaxed for future studies. For instance, considering a spin ensemble which with a state initialized separately from the cavity and then introduced to the quantized field may yield various insights into the nature of coherence growth, information transport, and entanglement. In addition, initially coherent states on the cavity (and possibly even the spin ensemble) can be excited experimentally, and may prove to offer a wealth of new structure to explore.

Regardless of the initial state, knowledge of the full energy level structure of the Tavis-Cummings Hamiltonian is invaluable in any investigation. It is the belief of the author that this work provides a recipe for mapping that full structure efficiently, and in a manner that can be readily utilized in any scenario.

While not covered in this work, the hope is that knowledge of the energy level structure of the Hamiltonian can be used to develop new control methods for processing and storing quantum information.

Revisiting the formulation of the Hamiltonian itself, more precise experimental setups may wish to account for the effect of minute field inhomogeneities in the classical magnetic field. Including this effect will distinguish the spins, which will cause a major reshuffling of the eigenstates and inhibit the use of the method presented in this work. Assuming deviations in the field are small compared to the mean,

$$\bar{\omega} = \frac{1}{N}\sum_{i=1}^{N}\omega_i, \tag{4.1}$$

the inhomogenous field term can be written as a perturbation,

$$\frac{1}{2}\sum_{i=1}^{N}\omega_i\hat{\sigma}_z = \frac{\bar{\omega}}{2}\hat{J}_z + \sum_{i=1}^{N}\epsilon_i\hat{\sigma}_z. \tag{4.2}$$

Here, $\epsilon_i = 0.5(\omega_i - \bar{\omega})$. Assuming each ϵ_i is small, tools of perturbation theory would be a good place to start and investigation into the impact these terms have on time evolution of states assumed to be in a perfect Tavis-Cummings model. Treating the distribution of field deviations, ϵ_i, as an unknown gradient, it may even be the case that these deviations can be measured directly, providing a new method of mapping magnetic fields on atomic scales.

With the mapped energy level structure, there is hope that new techniques in cavity cooling of a spin ensemble may yet emerge. Cavity cooling aims to utilize a leaky cavity to enhance the cooling rates of a spin ensemble, which is currently limited by the fact that collective cooling models do not coupling neighboring angular momentum subspaces. With better knowledge of the induced energy level structure of the Tavis-Cummings, it is possible that non-collective control schema, such as gradient pulses or enhancement of existing field inhomogeneities, can be better utilized to drive population towards the true ground state of $|N/2, -N/2\rangle\,|0\rangle$ with an enhanced rate.

The possible avenues for future exploration are seemingly endless, and the information and methods presented in this work are hopefully a large step forward into the discovery or refinement of new experimental technique.

References

[1] Leandro Aolita, Fernando De Melo, and Luiz Davidovich. Open-system dynamics of entanglement: a key issues review. *Reports on Progress in Physics*, 78(4):042001, 2015.

[2] OWB Benningshof, HR Mohebbi, IAJ Taminiau, GX Miao, and DG Cory. Superconducting microstrip resonator for pulsed esr of thin films. *Journal of Magnetic Resonance*, 230:84–87, 2013.

[3] OWB Benningshof, HR Mohebbi, IAJ Taminiau, GX Miao, and DG Cory. Superconducting microstrip resonator for pulsed esr of thin films. *Journal of Magnetic Resonance*, 230:84–87, 2013.

[4] Nicolaas Bloembergen. On the interaction of nuclear spins in a crystalline lattice. *Physica*, 15(3-4):386–426, 1949.

[5] Nicolaas Bloembergen, Edward Mills Purcell, and Robert V Pound. Relaxation effects in nuclear magnetic resonance absorption. *Physical review*, 73(7):679, 1948.

[6] NM Bogoliubov, RK Bullough, and J Timonen. Exact solution of generalized tavis-cummings models in quantum optics. *Journal of Physics A: Mathematical and General*, 29(19):6305, 1996.

[7] GS Boutis, D Greenbaum, Hyungjoon Cho, DG Cory, and C Ramanathan. Spin diffusion of correlated two-spin states in a dielectric crystal. *Physical review letters*, 92(13):137201, 2004.

[8] Bradley A Chase and JM Geremia. Collective processes of an ensemble of spin-1/ 2 particles. *Physical Review A*, 78(5):052101, 2008.

[9] Ed S Coakley and Vladimir Rokhlin. A fast divide-and-conquer algorithm for computing the spectra of real symmetric tridiagonal matrices. *Applied and Computational Harmonic Analysis*, 34(3):379–414, 2013.

[10] David L. Cooper, Fabio E. Penotti, and Robert Ponec. Reassessing spin-coupled (full generalized valence bond) descriptions of ozone using three-center bond indices. 2017.

[11] Thomas L Curtright, David B Fairlie, Cosmas K Zachos, et al. A compact formula for rotations as spin matrix polynomials. *SIGMA. Symmetry, Integrability and Geometry: Methods and Applications*, 10:084, 2014.

[12] Gabriele De Chiara and Anna Sanpera. Genuine quantum correlations in quantum many-body systems: a review of recent progress. *Reports on Progress in Physics*, 81(7):074002, 2018.

[13] Christian L Degen, F Reinhard, and Paola Cappellaro. Quantum sensing. *Reviews of modern physics*, 89(3):035002, 2017.

[14] Dean G Duffy. *Green's functions with applications*. CRC Press, 2015.

[15] Marcin Dukalski and Yaroslav M Blanter. High jaynes-cummings pseudospins eigenstates in the homogeneous tavis-cummings model. *arXiv preprint arXiv:1301.4857*, 2013.

[16] Luigi Frunzio, Andreas Wallraff, David Schuster, Johannes Majer, and Robert Schoelkopf. Fabrication and characterization of superconducting circuit qed devices for quantum computation. *IEEE transactions on applied superconductivity*, 15(2):860–863, 2005.

[17] JMG Gómez, K Kar, VKB Kota, Rafael A Molina, Armando Relaño, and Joaquín Retamosa. Many-body quantum chaos: Recent developments and applications to nuclei. *Physics Reports*, 499(4-5):103–226, 2011.

[18] D Greenbaum, M Kindermann, C Ramanathan, and DG Cory. Hydrodynamic approach to coherent nuclear-spin transport. *Physical Review B*, 71(5):054403, 2005.

[19] David J Griffiths. Introduction to electrodynamics, 2005.

[20] Serge Haroche and Jean-Michel Raimond. *Exploring the Quantum*. Oxford University Press, 2006.

[21] Hiroshi Hayashi, Tatsumasa Itahashi, Kohei M Itoh, Leonid S Vlasenko, and Marina P Vlasenko. Dynamic nuclear polarization of s 29 i nuclei in isotopically controlled phosphorus doped silicon. *Physical Review B*, 80(4):045201, 2009.

[22] M Himbert, J Dupont-Roc, and C Lhuillier. Spin-diffusion coefficient in gaseous helium between 1 and 0.5 k. *Physical Review A*, 39(12):6170, 1989.

[23] Atac Imamoğlu. Cavity qed based on collective magnetic dipole coupling: spin ensembles as hybrid two-level systems. *Physical review letters*, 102(8):083602, 2009.

[24] J Järvinen, J Ahokas, S Sheludyakov, O Vainio, L Lehtonen, S Vasiliev, D Zvezdov, Y Fujii, S Mitsudo, T Mizusaki, et al. Efficient dynamic nuclear polarization of phosphorus in silicon in strong magnetic fields and at low temperatures. *Physical Review B*, 90(21):214401, 2014.

[25] Leo P Kadanoff and Paul C Martin. Hydrodynamic equations and correlation functions. *Annals of Physics*, 24:419–469, 1963.

[26] Gurneet Kaur and Paola Cappellaro. Initialization and readout of spin chains for quantum information transport. *New Journal of Physics*, 14(8):083005, 2012.

[27] Ryogo Kubo. Brownian motion and nonequilibrium statistical mechanics. *Science*, 233(4761):330–334, 1986.

[28] Y Kubo, FR Ong, Patrice Bertet, Denis Vion, V Jacques, D Zheng, A Dréau, J-F Roch, Alexia Auffèves, Fedor Jelezko, et al. Strong coupling of a spin ensemble to a superconducting resonator. *Physical review letters*, 105(14):140502, 2010.

[29] Yuimaru Kubo, Cecile Grezes, Andreas Dewes, T Umeda, Junichi Isoya, H Sumiya, N Morishita, H Abe, S Onoda, T Ohshima, et al. Hybrid quantum circuit with a superconducting qubit coupled to a spin ensemble. *Physical review letters*, 107(22):220501, 2011.

[30] Willis E Lamb Jr and Robert C Retherford. Fine structure of the hydrogen atom by a microwave method. *Physical Review*, 72(3):241, 1947.

[31] Jongmin Lee, Michael J Martin, Yuan-Yu Jau, Tyler Keating, Ivan H Deutsch, and Grant W Biedermann. Demonstration of the jaynes-cummings ladder with rydberg-dressed atoms. *Physical Review A*, 95(4):041801, 2017.

[32] Robert Mann. *An introduction to particle physics and the standard model*. CRC press, 2011.

[33] John Preskill. Quantum computing in the nisq era and beyond. *Quantum*, 2:79, 2018.

[34] AG Redfield. Spatial diffusion of spin energy. *Physical Review*, 116(2):315, 1959.

[35] MD Reed, L DiCarlo, BR Johnson, L Sun, DI Schuster, L Frunzio, and RJ Schoelkopf. High-fidelity readout in circuit quantum electrodynamics using the jaynes-cummings nonlinearity. *Physical review letters*, 105(17):173601, 2010.

[36] Heinz Rutishauser. The jacobi method for real symmetric matrices. *Numerische Mathematik*, 9(1):1–10, 1966.

[37] Jun John Sakurai and Eugene D Commins. Modern quantum mechanics, revised edition, 1995.

[38] William I Salmon. Genealogical electronic spin eigenfunctions and antisymmetric many-electron wavefunctions generated directly from young diagrams. In *Advances in Quantum Chemistry*, volume 8, pages 37–94. Elsevier, 1974.

[39] Giuseppe E Santoro and Erio Tosatti. Optimization using quantum mechanics: quantum annealing through adiabatic evolution. *Journal of Physics A: Mathematical and General*, 39(36):R393, 2006.

[40] Jochen Scheuer, Ilai Schwartz, Samuel Müller, Qiong Chen, Ish Dhand, Martin B Plenio, Boris Naydenov, and Fedor Jelezko. Robust techniques for polarization and detection of nuclear spin ensembles. *Physical Review B*, 96(17):174436, 2017.

[41] DI Schuster, AP Sears, E Ginossar, L DiCarlo, L Frunzio, JJL Morton, H Wu, GAD Briggs, BB Buckley, DD Awschalom, et al. High-cooperativity coupling of electron-spin ensembles to superconducting cavities. *Physical review letters*, 105(14):140501, 2010.

[42] Bruce W Shore and Peter L Knight. The jaynes-cummings model. *Journal of Modern Optics*, 40(7):1195–1238, 1993.

[43] Charles P Slichter. *Principles of magnetic resonance*, volume 1. Springer Science & Business Media, 2013.

[44] Joel Spencer and Laura Florescu. Asymptopia, volume 71 of student mathematical library. *American Mathematical Society, Providence, RI*, page 66, 2014.

[45] Frank Spitzer. *Principles of random walk*, volume 34. Springer Science & Business Media, 2013.

[46] Andrew Stasiuk, Lane G Gunderman, Mohamed El Mandouh, Troy W Borneman, and David G Cory. Generalized collective lamb shift. *arXiv preprint arXiv:2101.09550*, 2021.

[47] Bill Sutherland. *Beautiful models: 70 years of exactly solved quantum many-body problems*. World Scientific Publishing Company, 2004.

[48] Michael Tavis and Frederick W Cummings. Exact solution for an n-molecule—radiation-field hamiltonian. *Physical Review*, 170(2):379, 1968.

[49] Gerald Teschl. *Jacobi operators and completely integrable nonlinear lattices*. Number 72. American Mathematical Soc., 2000.

[50] H Co Torrey. Nuclear spin relaxation by translational diffusion. *Physical Review*, 92(4):962, 1953.

[51] David S Watkins. Product eigenvalue problems. *SIAM review*, 47(1):3–40, 2005.

[52] Steven Weinberg. *The quantum theory of fields*, volume 2. Cambridge university press, 1995.

[53] Hermann Weyl. *The classical groups: their invariants and representations*, volume 45. Princeton university press, 1946.

[54] Bary W Wilson, Kris Caputa, Maria A Stuchly, Jeffrey D Saffer, Karl C Davis, Calvin E Washam, Lloyd G Washam, Glenn R Washam, and Mark A Wilson. Design and fabrication of well confined uniform magnetic field exposure systems. *Bioelectromagnetics: Journal of the Bioelectromagnetics Society, The Society for Physical Regulation in Biology and Medicine, The European Bioelectromagnetics Association*, 15(6):563–577, 1994.

[55] Antoni Wójcik, Tomasz Łuczak, Paweł Kurzyński, Andrzej Grudka, Tomasz Gdala, and Małgorzata Bednarska. Unmodulated spin chains as universal quantum wires. *Physical Review A*, 72(3):034303, 2005.

[56] Wurong Zhang and DG Cory. First direct measurement of the spin diffusion rate in a homogenous solid. *Physical review letters*, 80(6):1324, 1998.